

**MORPHOLOGY DYNAMICS OF PRECIOUS METAL CATALYSTS
FOR THE STEAM REFORMING OF OXYGENATED FUELS**

by

Stephen Crowley

A dissertation submitted to the Graduate Faculty in Engineering

In partial fulfillment of the requirements for the degree of

Doctor of Philosophy

The City College of the City University of New York

2016

© 2016
Stephen Crowley
All Rights Reserved

This manuscript has been read and accepted for the
Graduate Faculty in Engineering in satisfaction of the
dissertation requirement for the degree of Doctor of Philosophy.

Marco J. Castaldi, Chair of Examining Committee

Date

Ardie D. Walser, Associate Dean for Academic Affairs

Date

EXAMINING COMMITTEE

Elizabeth Biddinger, Professor of Chemical Engineering, The City College of
New York

Alexander Couzis, Professor of Chemical Engineering, The City College of
New York

Ilona Kretschmar, Professor of Chemical Engineering, The City College of
New York

Anatoly Frenkel, Professor of Materials Science and Chemical Engineering,
Stony Brook University

THE CITY COLLEGE OF THE CITY UNIVERSITY OF NEW YORK

Abstract

MORPHOLOGY DYNAMICS OF PRECIOUS METAL CATALYSTS FOR OXYGENATED HYDROCARBON STEAM REFORMING

by

Stephen Crowley

Advisor: Professor Marco J. Castaldi

Precious metal nanoparticles dispersed on high surface area carriers have been demonstrated to exhibit superior capabilities in catalyzing chemical reactions. Currently there is an emphasis on employing these precious metal catalysts in the reforming of fuels, a process in which an organic molecule is exposed to high temperatures in order to produce gaseous hydrogen for use in various applications. Traditionally natural gas has been used for the production of this hydrogen, limiting the overall sustainability of the process. Therefore, a shift to more sustainable sources in the form of biomass derived fuels is necessary.

Ethanol steam reforming (ESR) has been widely explored as a test case in order to identify appropriate catalyst materials for oxygenate reforming as well as to elucidate the reaction scheme governing the process. However, in a recent review on catalytic ESR by Hou *et al.*, the authors highlight that there is no agreed upon reaction pathway for the overall ethanol steam reforming process. Here we seek to provide new insights on the reaction pathways involved in steam reforming over a Rh-based catalyst demonstrated to have superior performance through the use of isotope-labeled reactants. *Operando* characterization of the catalyst showed

oxidation state and structural changes to the catalyst surface with partially-oxidized Rh providing optimal performance.

The low-temperature ESR reaction mechanism over a supported Rh/Pt catalyst was investigated using strategic isotope labeling of the reactants. This allowed for an unprecedented level of understanding with respect to the dominant reaction pathways, the contribution of each metal to the product distribution, and the role of the support. Both the recombination of C-species on the surface of the catalyst as well as preservation of the C-C bond within ethanol are responsible for C₂ product formation. The onset of ethylene, a common byproduct observed after catalyst deactivation, does not occur until incomplete ethanol conversion is observed. In addition, we quantitatively show that 57% of observed ethylene is formed directly through ethanol dehydration. Finally we provide clear evidence that oxygen in the silica-zirconia support likely constitutes 10% of the CO formed during reaction.

Acknowledgments

First and foremost, I would like to express my deepest gratitude to my advisor Prof. Marco J. Castaldi for the almost recklessly enthusiastic support of my Ph. D. research, regardless of how far-fetched (or expensive) my ideas were. His encouragement helped me to expand my way of thinking and his experience in the field of catalysis provided the scaffolding required to elevate the project work to a world-class level.

I am also extremely grateful for the insight and perspectives provided to me by the remaining members of my thesis committee; Prof. Elizabeth Biddinger, Prof. Ilona Kretzschmar, Prof. Alexander Couzis, and Prof. Anatoly Frenkel. A special thanks goes to Prof. Frenkel and the Synchrotron Catalysis Consortium at Yeshiva University for allowing me access to the National Synchrotron Light Source at Brookhaven National Laboratory. Due to the breadth of this committee's backgrounds, the feedback I received enabled me to appreciate the global impact of the work and allowed for well-rounded development during my studies. Furthermore, I would like to thank Prof. Kimberley Frederick for her mentorship during my undergraduate career at the College of the Holy Cross and exposing me to laboratory research for the first time.

My sincere thanks goes to Prof. Amanda Simson, a former member of the Combustion & Catalysis Laboratory, for providing me with an incredibly strong

theoretical and experimental foundation for my thesis work. Without her support initially and throughout my Ph. D. this research would not have been possible.

A gargantuan amount of appreciation is felt for my fellow researchers in the Combustion & Catalysis Laboratory, specifically Dr. Timothy Sharobem, Dr. Naomi Klinghoffer, Jeffrey LeBlanc, Robyn Smith, and Michaela Wagar, for their unequivocal support both in and out of lab. The last several years would not have been nearly as enjoyable or productive without you all by my side.

Lastly, and arguably most importantly, I would like to thank my family: my parents, my sister, and my fiancé. Their guidance and support have made my personal and professional achievements all the more meaningful, and I hope to continue to make them proud.

Table of Contents

Chapter 1: Introduction	1
1.1. Motivation	1
1.2. Hydrodeoxygenation (HDO) of biomass	4
1.3. Renewable reformat selection	6
1.4. Catalyst selection and development	7
1.5. Thesis aim and organization	8
Chapter 2: Literature review	10
2.1. Dynamics of reforming catalysts	10
2.1.1. Deactivation mechanisms	10
2.1.2. Conformation and oxidation state changes	12
2.2. Ethanol steam reforming mechanism development	14
Chapter 3: Experimental methodology	16
3.1. Catalyst synthesis	16
3.1.1. Powder	16
3.1.2. Pellet	17
3.2. Catalyst characterization	17
3.2.1. CO chemisorption	17
3.2.2. Scanning electron microscopy (SEM)	18

3.2.3. Transmission electron microscopy (TEM)	18
3.2.4. X-ray diffraction (XRD)	19
3.2.5. X-ray absorption fine structure (XAFS).....	19
3.3. Reactor tests.....	19
3.3.1. Packed bed reactor	20
3.3.2. Nashner-Adler reactor.....	20
Chapter 4: Catalyst formulation and characterization	21
4.1. CO chemisorption	21
4.1.1. Dispersion dependence on formulation	22
4.1.2. Inert vs. oxidative environment calcination.....	24
4.2. SEM and TEM	25
4.3. X-ray diffraction.....	28
4.4. Conclusions	29
Chapter 5: Catalyst performance during ethanol steam reforming	30
5.1. Hydrogen activity of various catalyst formulations	30
5.2. Stability of highest performing formulation.....	33
5.3. Reforming temperature and pretreatment.....	35
5.4. Conclusions	38
Chapter 6: Conformational changes through <i>operando</i> X-ray analysis	39

6.1. Product Distribution.....	40
6.2. XANES	41
6.3. EXAFS.....	42
6.4. XAFS fitting	45
6.5 Conclusions	50
Chapter 7: Mechanistic insights through using isotope-labeled reactants	50
7.1. Reactant selection and operating conditions	51
7.2. Kinetic isotope effect.....	52
7.3. Product distribution vs time on stream	52
7.4. Isotopic composition of products	55
7.5. Conclusions	69
Chapter 8: Regeneration behavior	71
8.1. Oxidative regeneration	71
8.2. Reductive regeneration.....	73
Chapter 9: Modeling and simulations	75
9.1. Temperature profile along the reactor bed	75
9.2. Conversion profile along the reactor bed	77
Chapter 10: Conclusions and future work	80
10.1. Conclusions	80

10.2. Future work	82
10.2.1. Nanoparticle lattice structure.....	82
10.2.2. Reaction network at elevated temperatures	83
10.2.3. Carbon deposition.....	84
Appendices.....	85
Appendix A: Gaseous product analysis.....	85
A.1. Micro gas chromatography (μ GC)	85
A.2. Gas chromatography – mass spectroscopy (GC-MS)	86
Appendix B: XAFS	86
B.1. Nashner-Adler cell	86
B.2. XAFS fitting	87
Appendix C: Isotopic enrichment confirmation	89
Appendix D: Additional calculations and simulation – plug flow reactor...	92
D.1. Rate expression	92
D.2. Mass balance.....	94
D.3. Energy balance	96
D.4. Matlab code	100
Bibliography	100

List of Tables

Table 1: Energy densities of liquid fuels. [Trivalent 2010]	4
Table 2: Catalyst composition on SiO ₂ -ZrO ₂ support.	17
Table 3: Dispersion of precious metals on silica-zirconia support as a function of calcination temperature (under inert conditions) determined through CO chemisorption.	22
Table 4: Turnover frequencies (TOFs) for all catalyst formulations. Reaction conditions: S/C = 1.5, GHSV = 44,000 hr ⁻¹ , calcination temperature: 650°C, reforming temperature: 650°C, and 1 atm.....	33
Table 5: Summary of XAFS fitting results for the 3 wt% Rh/1 wt% Pt catalyst during several stages of ethanol reforming.	46
Table 6: Calculated coordination number ratios for 3 wt% Rh/1 wt% Pt under reforming conditions.	49
Table 7: Isotope product distribution for CH ₄ during ethanol reforming across three catalyst formulations.	60
Table 8: Isotope product distribution for C ₂ H ₆ during ethanol reforming across three catalyst formulations.	62
Table 9: Isotope product distribution for C ₂ H ₄ during ethanol reforming across three catalyst formulations.	64
Table 10: Isotope product distribution for CO during ethanol reforming across all catalyst formulations.	65

Table 11: Isotope product distribution for H ₂ O during ethanol reforming across all catalyst formulations.	66
Table 12: Isotope product distribution for CO ₂ during ethanol reforming across all catalyst formulations.	68
Table A.1: Inficon 3000 Micro GC channel specifications and applications.....	85
Table A.2: Method parameters for gaseous product analysis by GC-MS.	86
Table A.3: Species balance during ethanol steam reforming based on stoichiometry in Equation (A.3).	93
Table A.4: Parameters for calculation of overall heat transfer coefficient in the packed bed catalytic reactor. [The Engineering ToolBox 2016].....	98
Table A.5: Sixth-order polynomial fit coefficients describing the change in heat capacity as a function of temperature for each reaction component as described in Equation (A.46).	99

List of Figures

Figure 1: Overall hydrodeoxygenation (HDO) process of fuels from biomass involving (1) processing of raw biomass into its constituent components, (2) acid digestion of biopolymers, and (3) removal of oxygen from the chemical makeup of the fuel through hydrogen treatment. Figure adapted from Choudhary <i>et al.</i> 2011. Dashed box: steam reforming of oxygenated hydrocarbons.	6
Figure 2: Schematic of possible reaction pathways during ethanol steam reforming. Circled numbers correlate to numbered Equations (1-12). Arrows represent forward reactions for simplicity. [Crowley <i>et al.</i> 2016]	15
Figure 3: Graphical representation of data shown in Table 3; Dispersion of precious metals on silica-zirconia support as a function of calcination temperature determined through CO chemisorption.	23
Figure 4: Dispersion of precious metals on silica-zirconia support as a function of calcination temperature in an inert (solid symbols) and oxidative (open symbols) environment for A) 3 wt% Rh/1 wt% Pt and B) 0 wt% Rh/4 wt% Pt. Inert environment calcination profiles reproduced from data presented in Table 3 and Figure 3.	24
Figure 5: SEM images of 3 wt% Rh/1 wt% Pt on silica-zirconia calcined at (A) 550°C, (B) 650°C, (C) 750°C, and (D) 850°C) with sub-micron crystallites highlighted in red circles.	26

Figure 6: TEM images of 3 wt% Rh/1 wt% Pt on silica-zirconia calcined at 850°C. Dark black spots indicate the presence of precious metal nanoparticles as confirmed with EDS.....	27
Figure 7: XRD profiles for 3 wt% Rh/1 wt% Pt on silica-zirconia support calcined at various temperatures.....	28
Figure 8: Hydrogen production of various single metal and bimetallic Rh-Pt catalyst formulations. All catalysts were calcined at 650°C under He and pre-reduced in 5% H ₂ in N ₂ . Reaction conditions: S/C = 1.5, volumetric GHSV = 44,000 hr ⁻¹ , calcination temperature: 650°C, reforming temperature: 650°C, and 1 atm.	31
Figure 9: Product distribution for the steam reforming of ethanol at 650°C over pre-reduced 3 wt% Rh/1 wt% Pt on silica-zirconia as a function of time on stream. Reaction conditions: S/C = 1.5, GHSV = 44,000 hr ⁻¹ , calcination temperature: 650°C, reforming temperature: 650°C, and 1 atm.....	34
Figure 10: Product distribution for the low-temperature steam reforming of ethanol over (A) pre-reduced 3 wt% Rh/1 wt% Pt on silica-zirconia and (B) non-pre-reduced 3 wt% Rh/1 wt% Pt on silica-zirconia as a function of time on stream. Reaction conditions: S/C = 1.5, GHSV = 44,000 hr ⁻¹ , calcination temperature: 550°C, reforming temperature: 350°C, and 1 atm.....	36
Figure 11: Product distribution for the steam reforming of ethanol at 350°C over 3 wt% Rh/1 wt% Pt on silica-zirconia as a function of time on stream in a Nashner-Adler reaction cell with <i>operando</i> X-ray analysis.	40

Figure 12: Rh K-edge XANES spectra under <i>operando</i> ethanol reforming conditions. Arrows within the legend indicate direction of edge shift for each stage of ethanol reforming. Idealized graphics of the catalyst surface are shown for clarity.....	41
Figure 13: Rh K-edge EXAFS spectra under <i>operando</i> ethanol reforming conditions in A) k-space and B) R-space for the 3 wt% Rh/1 wt% Pt catalyst.	44
Figure 14: Pt L ₃ -edge EXAFS spectra under <i>operando</i> ethanol reforming conditions in A) k-space and B) R-space for the 3 wt% Rh/1 wt% Pt catalyst.	45
Figure 15: Idealized representation of a A) core-shell, B) metal segregated, C) alloy or mixed metal, and D) three-shell nanoparticle atomic configuration. [Ferrando <i>et al.</i> 2008]	48
Figure 16: Isotope-labeled reactants, ethanol-1- ¹³ C and water- ¹⁸ O.[Crowley <i>et al.</i> 2016]	51
Figure 17: Product distribution profile for the reforming of ethanol-1- ¹³ C with water- ¹⁸ O over (A) 3 wt% Rh/1 wt% Pt, (B) 4 wt% Rh, and (C) 4 wt% Pt on SiO ₂ -ZrO ₂ support. Reaction conditions: S/C = 1.5, GHSV = 44,000 hr ⁻¹ , calcination temperature: 550°C, reforming temperature: 350°C, and 1 atm. [Crowley <i>et al.</i> 2016]	54
Figure 18: Atomic partitioning of ¹² C, ¹³ C, ¹⁶ O, and ¹⁸ O shown as part of the total amount detected (left) and as percent composition (right) into (A) methane, (B) ethane, (C) ethylene, (D) carbon monoxide, and (E) carbon dioxide over 3 wt% Rh/1 wt% Pt on SiO ₂ -ZrO ₂ . Bold colored text indicates isotope labeling. [Crowley <i>et al.</i> 2016]	56

Figure 19: Atomic partitioning of ^{12}C , ^{13}C , ^{16}O , and ^{18}O shown as part of the total amount detected (left) and as percent composition (right) into (A) methane, (B) ethane, (C) ethylene, (D) carbon monoxide, and (E) carbon dioxide over 4 wt% Rh on $\text{SiO}_2\text{-ZrO}_2$. Bold colored text indicates isotope labeling. [Crowley *et al.* 2016]..... 58

Figure 20: Atomic partitioning of ^{12}C , ^{13}C , ^{16}O , and ^{18}O shown as part of the total amount detected (left) and as percent composition (right) into (A) methane, (B) ethane, (C) ethylene, (D) carbon monoxide, and (E) carbon dioxide over 4 wt% Pt on $\text{SiO}_2\text{-ZrO}_2$. Bold colored text indicates isotope labeling. [Crowley *et al.* 2016]..... 59

Figure 21: Schematic of possible dominant reaction pathways during ethanol steam reforming at (A) $t = 0$, (B) $t = 1.25$ h, (C) $t = 2.25$ h, and (D) $t = 4$ h. Black shading highlights dominant reaction pathways at each time. Red X indicates that the reaction most likely does not occur. Circled numbers correlate to numbered Equations (1-12). Arrows represent forward reaction for simplicity. [Crowley *et al.* 2016]..... 69

Figure 22: Product distribution profile for the reforming of ethanol- $1\text{-}^{13}\text{C}$ with water- ^{18}O with 1 hour regeneration in 5% O_2 in N_2 over (A) 3 wt% Rh/1 wt% Pt, (B) 4 wt% Rh, and (C) 4 wt% Pt on $\text{SiO}_2\text{-ZrO}_2$ support. Reaction conditions: $S/C = 1.5$, $\text{GHSV} = 44,000 \text{ hr}^{-1}$, calcination temperature: 550°C , reforming temperature: 350°C , and 1 atm. [Crowley *et al.* 2016]..... 72

Figure 23: Product distribution profile for the steam reforming of ethanol with 1 hour regeneration in 5% H_2 in He over (A) 3 wt% Rh/1 wt% Pt, (B) 4 wt% Rh, and (C) 4 wt% Pt on $\text{SiO}_2\text{-ZrO}_2$ support. Reaction conditions: Nashner-Adler reactor, $S/C = 1.5$, flow rate = 44 mL/min, calcination temperature: 550°C , reforming temperature: 350°C , and 1 atm..... 74

Figure 24: Nondimensionalized temperature profile along the reactor bed for catalytic ethanol steam reforming performed at (A) 350°C and (B) 650°C.	76
Figure 25: Nondimensionalized conversion profile along the reactor bed for catalytic ethanol steam reforming performed at (A) 350°C and (B) 650°C.	78
Figure 26: Fractional conversion as a function of position along the packed bed reactor for ethanol steam reforming performed at various temperatures.	79
Figure A.1: Nashner-Adler cell used for X-ray characterization of the catalyst during ethanol steam reforming.....	87
Figure A.2: XAFS fitting of the Rh-edge and Pt-edge spectra for the 3 wt% Rh/1 wt% Pt catalyst during several stages of ethanol reforming.....	88
Figure A.3: Total ion chromatograms for (A) water and water- ¹⁸ O and (B) ethanol and ethanol-1- ¹³ C.....	90
Figure A.4: Mass spectral fragmentation pattern of (A) water and (B) water- ¹⁸ O...	91
Figure A.5: Mass spectral fragmentation pattern of (A) ethanol and (B) ethanol-1- ¹³ C.	91

Chapter 1: Introduction

1.1. Motivation

Catalytic steam reforming of hydrocarbon fuels has proven to be an effective means of meeting the demand for hydrogen with many benefits including high theoretical efficiencies.¹ There continues to be a push to expand our knowledge of established catalytic systems and determine their limitations with regard to specific applications. Catalytic materials have already been shown to deliver higher selectivity, improved conversion, and faster reaction time,² but the extent of these advantages can depend on a multitude of factors that are not fully determined for many systems. In the pursuit of these limits, it has been observed that precious metals, specifically platinum group metals (PGMs), such as rhodium, palladium, and platinum exhibit improved performance over their lower-cost counterparts including iron, cobalt, and nickel.³ Intrinsic reaction rates were examined for methane steam reforming by Obradović *et al.* with platinum exhibiting 8 times the activity of nickel-based catalysts,⁴ showing that while it can be argued that the initial cost of PGMs is prohibitively expensive, their overall performance more than makes up for the staggering upfront investment over the life of the catalyst.

In optimizing catalytic behavior, extensive work has been performed investigating how particular catalyst materials behave in the presence of various reactants, including but not limited to alkanes, ketones, esters, and alcohols. Initial studies focused on the use of a single metal dispersed over a high surface area

metal-oxide support. This was done in an attempt to understand the activities of individual metals as well as the influence of the support on catalytic activity.

Recent work by Tang *et al.* reexamined the “volcano curve” generated by plotting the turnover frequency (TOF) as a function of the change in enthalpy of formation for activated species across a wide range of base and precious metal catalysts.⁵ Not surprisingly, platinum group metals (PGMs) exhibited the highest TOFs at moderate binding energies.

Along these lines, several modes of activation have been identified throughout the literature on catalysis. Activation through the on-stream formation of active sites by reactant molecules has been shown for supported silver catalysts used in the hydrocarbon selective catalytic reduction (SCR) of NO_x.⁶ This type of activation is largely attributed to the carbon species present in the reactants, able to form numerous complexes that enhance activity.⁷ Activation by restructuring in which a chemical stimulus induces reconfiguration of the metal atom lattice structure to an activated state has been shown for transition metals.⁸ Support material has been shown to play a role in catalyst metal particle reconfiguration,⁹ however this restructuring is more consequential when induced by catalyst poisons such as sulfur or the adsorption of alkali metals from the reactants. The modes by which restructuring occurs and the well-established structure-activity relationships for heterogeneous catalysts provide motivation for the investigation of highly engineered bimetallic catalysts due to the presence of a promoter material.

The role of individual metals as they combine synergistically in bimetallic catalysts and the resulting impact on overall performance behavior is not yet well understood for many catalytic systems. Structure-activity relationships have been under investigation for over four decades¹⁰ with recent advances highlighting the importance of various structures through the destabilization modes of reactants on unique surface lattices.^{11,12} Bimetallic catalysts have been identified to have excellent activity in processes ranging from selective or preferential oxidation^{13–15} to hydrogenation^{16–18} and reforming reactions.^{19–21} While catalysts designed for methane reforming have been well characterized, the presence of carbon-carbon bonds as well as reactive functional groups expose the shortcomings of these catalysts. Ergo, the dynamics of reforming catalysts depend greatly on the reformat itself.

Fuels used as the reformat have largely originated from nonrenewable sources such as petroleum²² and natural gas,²³ therefore it is desirable to find a more renewable feedstock to derive this hydrogen. Ethanol has been identified as a potential starting material for reasons of current cost and availability.^{24,25} Furthermore, we are using ethanol as a model compound for typical oxygenated hydrocarbons formed from the processing of renewables.

The presence of oxygen within the chemical makeup of more renewable fuels is detrimental to the fuel's energy density.²⁶ Table 1 lists common liquid fuels of varying oxygen content and their energy densities for a direct comparison.²⁷

Table 1: Energy densities of liquid fuels. [Trivalent 2010]

Fuel	Chemical Formula	Energy Density (MJ/kg)
Liquefied Natural Gas	CH ₄ (majority)	48.63
Conventional Gasoline	C ₈ H ₁₈ to C ₁₂ H ₂₆	43.45
US Conventional Diesel ²⁸	C ₁₀ H ₂₀ to C ₁₅ H ₂₈	42.79
Biodiesel (Methyl Ester) ²⁹	C ₁₇ H ₃₄ O ₂ to C ₁₉ H ₃₂ O ₂	37.53
n-Butanol	C ₄ H ₁₀ O	34.37
Ethanol	C ₂ H ₆ O	26.95
Methanol	CH ₄ O	20.10

Comparing methanol with liquefied natural gas, the addition of an oxygen atom into the chemical structure results in a 59% decrease in energy density. As a way to combat this, a process known as the hydrodeoxygenation (HDO) of biofuels has been identified to upgrade biologically derived oxygenated hydrocarbons into oxygen-free fuels with higher energy densities.

1.2. Hydrodeoxygenation (HDO) of biomass

In the HDO process, biomass is first broken down into its constituent carbohydrates, primarily cellulose and hemicellulose. These carbohydrates undergo acid digestion into simple sugars which are then treated with hydrogen to remove oxygen functional groups, thereby converting sugars and alcohols into linear alkanes with higher energy densities.³⁰ Within this process, an external source of hydrogen is needed to carry out the final steps of the synthesis to give rise to the final product.

In the ideal process, the removal of every oxygen atom from the feedstock should require one H₂ molecule for the formation of water. Therefore, for the many sugars and polyols containing more than one oxygen atom, the amount of H₂ consumed increases dramatically to ensure full conversion. It was determined that for every mole of triglyceride, a common oxygenate produced during biomass processing, fifteen moles of hydrogen are required to fully convert the feedstock into oxygen-free hydrocarbons and water.³¹ As previously mentioned, the primary supply of hydrogen comes from petroleum feedstocks, so in effect the desired products (n-alkanes) are still being derived from petroleum. In fact, it was found that 100 to 400 Nm³ of hydrogen per ton of feedstock was needed to achieve desired levels of hydrodeoxygenation.³² Consequently, it is desirable to obtain the hydrogen used from renewable sources, thereby making the entire process renewables-driven.

The work of Chattanathan *et al.* explored the benefit and feasibility of using biologically derived fuels as the reformat.³³ Our research seeks to expand on this idea by using the sugars and alcohols produced in the HDO intermediate steps themselves as the reformat for hydrogen production as depicted in Figure 1 (adapted from Choudhary *et al.* 2011). This would make the overall process more self-contained and inherently more sustainable.

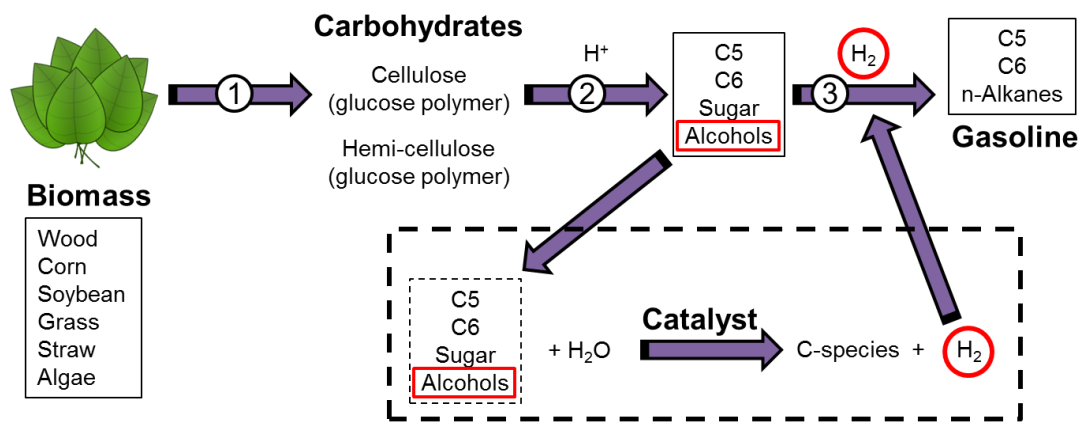


Figure 1: Overall hydrodeoxygenation (HDO) process of fuels from biomass involving (1) processing of raw biomass into its constituent components, (2) acid digestion of biopolymers, and (3) removal of oxygen from the chemical makeup of the fuel through hydrogen treatment. Figure adapted from Choudhary *et al.* 2011. Dashed box: steam reforming of oxygenated hydrocarbons.

The steam reforming of natural gas is the primary production method for hydrogen, so in effect the desired products are still ultimately being derived from non-renewable sources. Consequently, it is desirable to generate the hydrogen used in this process from more sustainable sources, thereby making the entire process renewables-driven.

1.3. Renewable reformate selection

In the initial stages of HDO, the compounds isolated from the biomass feedstock to be used as the reformate could fall into several categories of chemical composition, each with distinct behavior in the reforming process. Carbohydrates such as sugars have markedly different performance in hydrogen yield from polyols such as methanol, ethylene glycol, and sorbitol with glucose providing only 50% of the hydrogen selectivity provided by methanol.³⁴ While methanol inherently provides higher selectivity toward hydrogen, higher order oxygenated hydrocarbons

are much more abundant in the first stages of the HDO process. Ethanol, glucose, glycerol, and 3-hydroxybutyrolactone have been identified as representative derivatives of lignocellulosic biomass polymers.³⁵ Due to their increasingly complex chemical structures, they become more difficult to use as platform chemicals in the reforming process. Ethanol, with the presence of a single C-C bond and an oxygenated functional group, could provide a basis for understanding how the functional groups and carbon backbones are affected in the reforming process.

1.4. Catalyst selection and development

There are, however, no efficient catalysts for steam reforming of bio-derived feedstocks such as ethanol. Current catalysts rely on formulations developed for reforming of natural gas (methane) and petroleum-derived fractions with minimum concentrations of oxygen-containing hydrocarbons (oxygenates). These catalysts do not offer sufficient activity and stability for bio-derived feedstocks with large concentrations of oxygenates.³⁶ For example, bio-oils produced by pyrolysis typically contain about 40-45 wt% oxygen from oxygenates and those obtained by liquefaction – about 15 wt%.³⁷⁻⁴⁰

Historically base-metal catalysts such as Ni, Fe, and Cu have been used in fuel reforming.^{3,41,42} These catalytic materials have demonstrated activities for the water-gas shift reaction (Equation 4) as well as capabilities in the reforming of natural gas, however they have not been effective for oxygenated fuels. Specifically, Cu was shown to be ineffective at breaking the C-C bond in ethanol while Ni catalysts deactivated readily due to coke formation. These findings have led to the

investigation of precious metals as catalysts for steam reforming oxygenated fuels. Pt has previously been demonstrated to promote the water-gas shift reaction while Rh can efficiently break the C-C bond in ethanol and is resistant to coke formation⁴³. It is anticipated that the higher activity and more stable long-term performance may provide justification for the increased up-front cost of using precious metals compared to base metal catalysts.

1.5. Thesis aim and organization

One of the most pressing challenges in reforming oxygenated hydrocarbons is their tendency to cause rapid deactivation of highly engineered catalysts used in conventional processes such as methane steam reforming. The varying functional groups as well as the combination of sugars, ethers, ketones, and alcohols found in biomass convolute the inner workings of the catalyst system, making it extremely difficult to attribute particular deactivation behavior to the chemical structure of a molecule. The goal of this work is to understand the catalytic underpinnings dictating overall performance in the steam reforming of oxygenated hydrocarbons, specifically to increase selectivity toward desired products and reduce the severity of observed deactivation.

Chapter 2 consists of a literature review on the current understanding of catalyst deactivation mechanisms and their possible causes. Well understood mechanisms such as precious metal and carrier sintering, coking, and pore structure collapse are discussed. Changes to the structure of heterogeneous catalysts used in reforming applications are also reviewed.

The third chapter recaps the experimental methodology that was used throughout the studies in the chapters to follow. Catalyst synthesis, characterization, and reactor test parameters are detailed.

Chapter 4 details the formulation and initial characterization work of the catalysts used in the steam reforming of ethanol. The dispersion of precious metals on the support, crystal structure, and micrographs are presented within. Increasing calcination temperature was found to decrease the accessibility of catalytically active sites and increase the crystallinity of the sample across all catalyst formulations.

In the fifth chapter, each synthesized catalyst is compared to determine the optimal ratio of the precious metals by examining their performance in the ethanol steam reforming process. A Rh:Pt ratio of 3:1 was found to provide the greatest selectivity toward hydrogen with the least amount of deactivation over the course of 90 hours. Energy input to the system and catalyst pretreatment were investigated to observe differences in the stability, selectivity, and regenerability of the highest performing catalyst formulation.

Chapter 6 details *in situ* and *operando* X-ray absorption spectroscopy techniques used to monitor the oxidation state of the precious metal nanoparticles on the surface of the catalyst as a function of time on stream. A partially oxidized Rh species was found to be the most active whereas the oxidation state of Pt showed little to no change. The current hypothesis is that the presence of Pt stabilizes the

precious metal nanoparticle structure, allowing for an extension of the time period in which catalytic sites remain active.

The seventh chapter presents catalytic ethanol steam reforming mechanistic insights expounded through the use of isotope-labeled reactants. It was shown that species recombination on the surface of the catalyst is the primary pathway for C-containing products. Chapter 8 describes regeneration behavior in reducing and oxygenating environments as well as determining if there is a preference for coke formation by the oxygen-bound carbon or methyl group in ethanol. Only a slight preference for the carbon bound to oxygen was observed with a roughly 50/50 distribution.

Chapter 9 shows the results of modeling and simulation work at various test parameters for our system describing the conversion and temperature profiles along the length of the reactor. A full development of the governing equations is presented in Appendix D. Lastly, in chapter 10, conclusions and possible future work are discussed.

Chapter 2: Literature review

2.1. Dynamics of reforming catalysts

2.1.1. Deactivation mechanisms

Catalyst deactivation is one of the major challenges faced in fuel reforming and there exists a need to determine the underlying causes, enabling model refinement and preventative measures to be developed. Well-known deactivation

mechanisms include coke formation, carrier deactivation in the form of sintering and pore structure collapse, poisoning, and metal sintering. Coke, or carbon deposited on the catalyst surface, renders active sites inaccessible to reactants and is ultimately detrimental to the performance of the catalyst. Ethylene, acetaldehyde, and other C₂-species are widely known coke precursors.⁴⁴ Thus, reforming oxygenated hydrocarbons with more than one atom of carbon per molecule presents a challenge to preventing C₂ formation. In their work comparing the reforming of methane, methanol, and ethanol, Laosiripojana *et al.* found that no C₂ species were detected during methane and methanol reforming. However, ethanol reforming resulted in 13.5% combined ethylene and ethane detection.⁴⁵ Therefore, in the development of suitable catalysts, C₂ formation will likely pose a challenge.

The availability of catalytically active metal sites can also be reduced through precious metal sintering, a widely reported feature of dispersed metal catalysts used at elevated temperatures.^{41,46–48} An agglomeration of metal nanoparticles decreases the surface area to volume ratio, enveloping catalytically active sites on the inside of the nanoparticle and reducing apparent catalytic activity. A similar phenomenon can be observed with the support, wherein exposure to elevated temperatures can cause pore-structure collapse, effectively trapping metal nanoparticles within the support matrix.⁴⁹ Exposure of the catalyst material to high temperatures inherently causes structural instability,⁵⁰ and in the case of

oxygenated fuel reforming, the presence of oxygen is likely to cause oxidation of the material as well.

Recently, initial results showed for the first time that the oxidation state of catalytic Rh nanoparticles changes dynamically under reaction conditions with ethanol and that the extent of Rh oxidation appears to control catalyst activity and the rate of deactivation.⁵¹ The oxidation state of metal catalysts has received an enormous amount of attention as a way to more fully understand their associated activities.^{52–60} Initial work in this area was performed on catalytic material before or after it was used in a chemical process.^{52–57} This integral approach has provided information regarding oxidation state changes, but provides no real information on how those changes occur. To determine the dynamics associated with a global oxidation state change, a notable shift toward *operando* catalyst characterization has taken place in the last several years.^{61–63}

2.1.2. Conformation and oxidation state changes

The extent to which catalyst oxidation state controls overall performance has been under discussion and investigation for decades.^{64–67} Lucrédio *et al.* employed *operando* methodology to fully understand the effect on active metal oxidation state and the structural ramifications of adding La to Ni and Rh-Ni catalysts for the reforming of biogas.⁶¹ X-ray absorption near edge structure (XANES) spectra at the Ni K-edge were collected throughout each stage of the experimental protocol, ranging from catalyst activation with hydrogen to the actual reforming of biogas at temperatures between 25–750°C.⁶¹ They found that the presence of the platinum

group metal (PGM) Rh allowed for the reduction of the Ni^{2+} species to Ni^0 at lower temperatures whereas the addition of La inhibited reduction of the nickel.⁶¹ They have shown that the presence of dopants and the addition of other catalytically active metals can drastically impact the effects of a pretreatment step and ultimately influence catalytic behavior.⁶¹

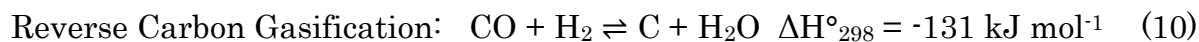
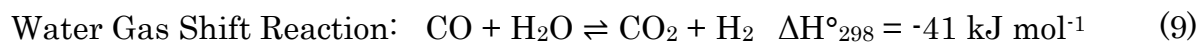
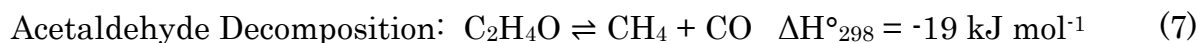
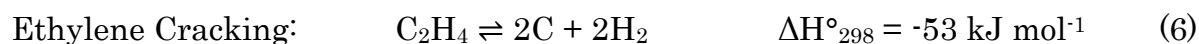
It has been shown that PGMs can fundamentally change the behavior of a base-metal catalyst. Divins and Llorca seek to expand on the functionality of these noble metals in the steam reforming of ethanol by looking at catalytic systems composed solely of PGMs and the impact of the support.^{63,68} Bimetallic Rh-Pd nanoparticles on a CeO_2 support were analyzed under *in situ* conditions, involving the transfer of material from the reactor to the X-ray photoelectron spectrometer,⁶³ as well as *operando* conditions where near-ambient pressure XPS was performed under true reaction conditions.⁶⁸ The *in situ* XPS experiments employed the Rh 3d, Pd 3d, and Ce 3d photoelectrons for characterization. It was found that the presence of the support inhibited the reduction of the metals during the hydrogen activation step common to the studies mentioned above, suggesting a large amount of electron withdrawal from the metals to the support.⁶³ However, the authors note that under *operando* conditions the bimetallic nanoparticles are much more enriched in Pd as well as more oxidized.

The conformation and oxidation state dynamics and the ability to actively measure them allows for informative diagnostics on the behavior of catalytic systems. These changes will ultimately lead to shifts in selectivity, possibly

producing intermediate compounds that either promote or are detrimental to desired product formation. Therefore, investigation is needed on the full impact of these changes on the reaction pathways present during the reforming process, allowing for improved catalyst design parameters in the future to achieve optimal performance.

2.2. Ethanol steam reforming mechanism development

There are a myriad of competing reactions contributing to the overall mechanistic understanding of ethanol steam reforming⁴⁸ as shown in Equations (1-12) and Figure 2.



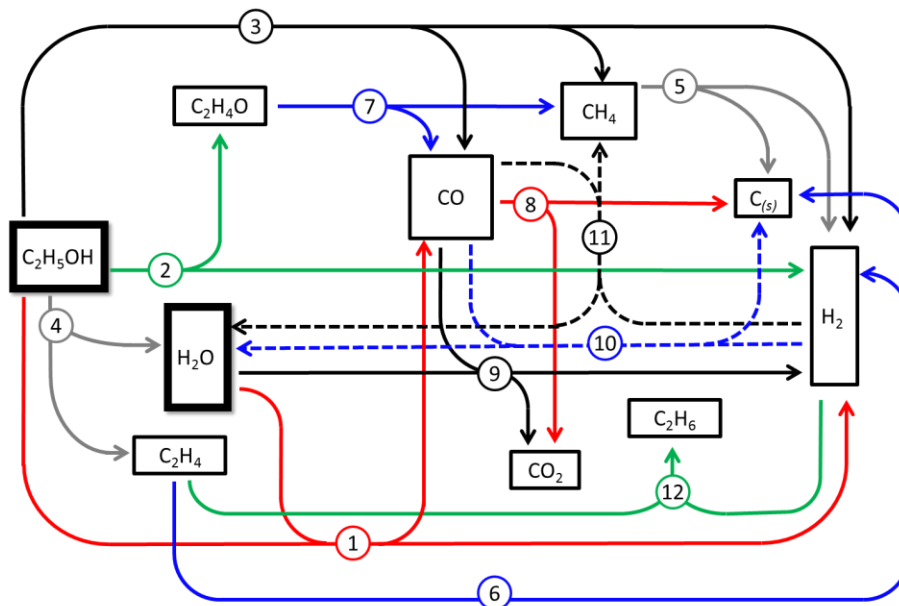


Figure 2: Schematic of possible reaction pathways during ethanol steam reforming. Circled numbers correlate to numbered Equations (1-12). Arrows represent forward reactions for simplicity. [Crowley *et al.* 2016]

Classic reaction model development focuses on measuring products over a range of test conditions combined with a proposed set of equilibrium reactions to match observed experimental data.^{48,69–71} In a recent review on catalytic ESR by Hou *et al.*, the authors highlight that there is no agreed upon reaction pathway for the overall ESR process.⁴⁸ Many researchers have contributed extensive experimental and modeling efforts to elucidate the precise reaction sequence. Vesselli *et al.* utilize X-ray photoelectron spectroscopy (XPS) of adsorbed ethanol on a Rh (111) surface and UHV desorption experiments while Resta *et al.* use density functional theory (DFT) to determine major species formed during ethanol decomposition, showing experimentally and computationally that C-C bond

cleavage is preferential to C-O bond scission.⁷²⁻⁷⁵ In addition, the dehydrogenation reaction [Equation (2)] on Rh/CeO₂ was studied by the Chen group, showing that an oxametallacycle is formed followed by C-C bond cleavage and desorption to yield CH₄, H₂, and CO.⁷⁶ However, there is currently no consensus on the origin of the atoms constituting the final observed products for the steam reforming of higher-order hydrocarbons.

Isotope labeling is a longstanding technique used to gain insight into the likelihood of particular reaction pathways.⁷⁷⁻⁷⁹ Song *et al.* used deuterated ethanol and water to determine the adsorption/desorption behavior of reactants⁸⁰ as well as to investigate the reaction pathway of ethanol and water over CeO₂- and ZrO₂-supported Co.⁸¹ These studies have provided a platform for further investigation in specific behavior of ethanol steam reforming systems.

Chapter 3: Experimental methodology

3.1. Catalyst synthesis

3.1.1. Powder

All catalyst preparation materials were obtained from BASF (RM-75ST) and incorporated into our laboratory synthesis procedures. Rh and Pt were impregnated on a SiO₂-ZrO₂ support (CAS number: 14808-60-7, 1314-23-4), chosen for its improved structural stability⁸² and demonstrated resistance to contaminants typically found in real systems,⁸³ via incipient wetness of aqueous metal salt solutions. Prior to impregnation, the carrier was pre-calcined at 950°C in air for 2

hours. The total metal loading was held constant at 4 weight percent. The ratio of Rh to Pt was varied stepwise by 1 weight percent starting with catalysts composed of pure Rh and finishing with pure Pt as shown in Table 2.

Table 2: Catalyst composition on SiO₂-ZrO₂ support.

Formulation	wt% Rh	wt% Pt
A	4	0
B	3	1
C	2	2
D	1	3
E	0	4

The impregnated support powders were dried and calcined in air for 2 hours at 120°C and 550°C respectively. Calcination at higher temperatures was performed in helium where indicated.

3.1.2. Pellet

Catalyst pellets were prepared for X-ray analysis. 100 mg of the catalyst powder stock as prepared in section 3.1.1 were pressed in a 13 mm die to a pressure of 10,000 psi. Pellets exhibited a thickness of approximately 1 mm, resulting in a density of 0.75 g/cm³.

3.2. Catalyst characterization

3.2.1. CO chemisorption

CO chemisorption was performed on a Quantachrome ChemBET PULSAR™ TPR/TPD Automated Chemisorption Flow Analyzer. All catalytic material was dried at 120°C for 2 hours under N₂, pre-reduced in 5% H₂ in N₂ at 400°C for 2

hours, and purged with N₂ for 1 hour prior to CO chemisorption being performed. Adsorption measurements were performed at room temperature assuming a chemical adsorption stoichiometry of CO to precious metal of 1 in order to calculate total CO uptake.

3.2.2. Scanning electron microscopy (SEM)

Scanning electron micrographs were obtained using a Zeiss Supra 55 field emission SEM. All samples were deposited on carbon conductive adhesive tape on aluminum pin stub SEM mounts and dried at 110°C for at least 2 hours prior to analysis. A potential of 5.0 kV was used with a working distance of 5 mm and an aperture of 30 μm.

3.2.3. Transmission electron microscopy (TEM)

Transmission electron micrographs were obtained using a JEOL JEM-2100 LaB6 transmission electron microscope. Images were collected using a Gatan Orius bottom-mount 11 megapixel camera. An operating potential of 200 kV was used for the collection of all images. Energy-dispersive silicon-drift X-ray (EDX) was used to confirm the presence and relative concentrations of precious metals on the catalyst materials. All samples were ground using an agate mortar and pestle and mounted on carbon TEM grids and introduced into the instrument via a standard JEOL double-tilt specimen holder.

3.2.4. X-ray diffraction (XRD)

XRD measurements were taken using a PANalytical X'Pert Powder Diffraction System. A Philips high intensity ceramic sealed tube with a power rating of 3 kW was used as the X-ray source utilizing Cu K α (1.5405 Å) radiation. The operation voltage was 40 kV over a 2 θ range of 35-45°. All measurements were performed at room temperature under ambient atmospheric conditions.

3.2.5. X-ray absorption fine structure (XAFS)

X-ray scans were taken using Beamline X18B of the National Synchrotron Light Source I at Brookhaven National Laboratory. A Si(111) crystal was used as the monochromator. Spectra were collected using both transmission and passivated implanted planar silicon (PIPS) fluorescence detection. The strongest signal from either detector was then used to perform extended x-ray absorption fine structure (EXAFS) analysis to gain insight on conformation.

3.3. Reactor tests

All catalysts, both powder and pelletized forms, were pre-reduced in 5% H₂ at 400°C for 2 hours with a flow rate of 44 mL/min prior to ethanol reforming experiments unless noted otherwise. Reaction products were monitored using an Agilent 3000 Micro GC equipped with Molecular Sieve (carrier gas: Ar) and Plot U (carrier gas: He) analytical columns and thermal conductivity detectors (TCDs). The ethanol and water reactants were introduced by bubbling ultra-high purity nitrogen (99.999%, T. W. Smith) through a liquid mixture of ethanol and water in

appropriate ratios to obtain a volumetric steam-to-carbon ratio (S/C) of 1.5 (stoichiometric). A large reservoir of the reactant mixture of 500 mL was used to ensure minimal changes to liquid and vapor phase concentrations. Prior to mixing with ethanol, water was purified through a Direct-Q UV Millipore system and had a measured resistance of 18.2 m Ω ·cm. Ethyl alcohol (Pure, 200 proof, cat#4455-4L) was obtained from EMD Omnipur[®]. Isotope-labeled reactants, ethanol-1-¹³C and water-¹⁸O, were introduced by bubbling research grade nitrogen (99.9999%, T. W. Smith) through separate reservoirs of ethanol-1-¹³C and water-¹⁸O, combined on stream to produce an identical reaction mixture to all other tests (S/C = 1.5).

3.3.1. Packed bed reactor

A fixed-bed quartz micro reactor was employed to obtain activity data. For tests involving a single reaction mixture reservoir as detailed in section 3.3, a quartz tube with inner diameter of 4 mm was placed inside the electric furnace of the ChemBET with a thermocouple positioned at the inlet of the catalyst bed to monitor temperature. A separate reactor was constructed for the isotope-labeled reactant experiments where all parameters used during reaction tests on the ChemBET were mimicked. Flow was verified by rotameter. A gas hourly space velocity (GHSV) of 44,000 hr⁻¹ was used during all reforming experiments.

3.3.2. Nashner-Adler reactor

A Nashner-Adler cell was used as a reactor to allow for *operando* X-ray measurements (see Appendix B.1). 100 mg of the catalyst was pressed into a 13 mm

pellet under 10,000 psi of pressure. In this configuration, the catalyst pellet was suspended in a relatively large volume of the reactant mixture under constant flow in and out of the chamber. Each reforming experiment consisted of pre-reducing the catalyst in 5% H₂ in He followed by ethanol reforming. Reductive regeneration was performed in 5% H₂ in He for 1 hour at the operating temperature of 350°C, followed by an Ar purge and a second ethanol reforming regime. The following conditions were used during each fuel reforming experiment: S/C = 1.5, 350°C, and 1 atm. X-ray scans were taken using Beamline X18B of the National Synchrotron Light Source I at Brookhaven National Laboratory.

Chapter 4: Catalyst formulation and characterization

4.1. CO chemisorption

To understand how the Rh:Pt ratio influenced the number of available catalytically active sites, dispersion of the precious metals on the support as a function of calcination temperature in an inert environment was quantified through CO chemisorption via the ChemBET. Equation (13) was used to calculate dispersion (D).

$$D = \frac{\text{Accessible Metal (g)}}{\text{Total Metal (g)}} = \frac{n_{CO}}{S} \cdot \frac{M_{PM}}{\%PM \cdot g_{cat}} \quad (13)$$

Where n_{CO} is the moles of chemisorbed CO, M_{PM} is the weighted average molecular weight of the precious metal, $\%PM$ is the total metal loading (this work: 4 weight percent), g_{cat} is the mass of catalyst (metal and support), and S is the stoichiometric ratio of adsorption. In this work, S was assumed to be a one-to-one stoichiometry for

uptake of CO to precious metal atom in dispersion calculations. While CO is known to dissociate on supported Rh catalysts,⁸⁴ this S value is generally accepted for supported Rh catalyst characterization^{85–87} as stoichiometry greater than one-to-one are observed primarily on isolated Rh sites at much lower metal loadings.⁸⁸

4.1.1. Dispersion dependence on formulation

The obtained dispersion values and a graphical representation of the data are shown in Table 3 and Figure 3 respectively.

Table 3: Dispersion of precious metals on silica-zirconia support as a function of calcination temperature (under inert conditions) determined through CO chemisorption.

Catalyst Formulation	Rh (wt%)	Pt (wt%)	Calcination Temperature				
			550°C	650°C	750°C	850°C	950°C
A	4	0	30.98%	26.63%	18.19%	3.01%	1.21%
B	3	1	26.69%	22.37%	12.14%	2.15%	0.70%
C	2	2	15.66%	16.30%	7.96%	2.13%	0.97%
D	1	3	16.92%	7.73%	1.42%	1.00%	0.02%
E	0	4	16.38%	14.58%	14.15%	9.86%	6.99%

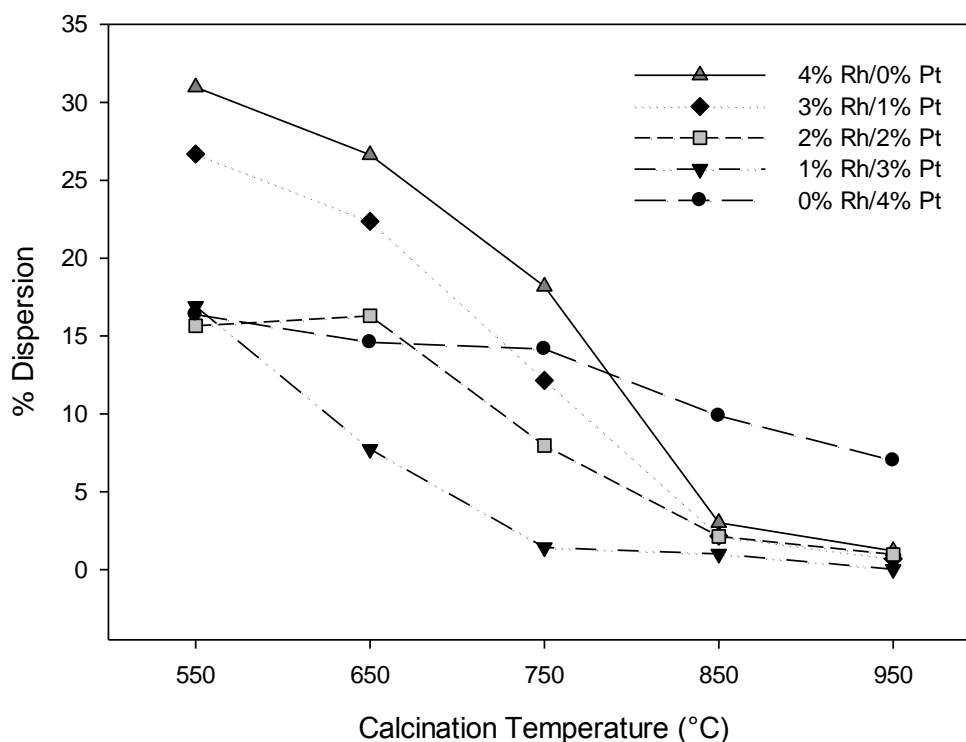


Figure 3: Graphical representation of data shown in Table 3; Dispersion of precious metals on silica-zirconia support as a function of calcination temperature determined through CO chemisorption.

Here it can be observed that for all formulations the measured dispersion decreases as a function of calcination temperature (in He). When solely looking at the lowest calcination temperature of 550°C the formulations fall into two distinct groups demonstrating a pronounced change between two and three wt%; high Rh-content (3 and 4 weight percent) and low Rh-content (2 weight percent and below).

Interestingly the pure Pt formulation maintains a higher dispersion at increasing calcination temperatures while the Rh-containing formulations follow a clear trend of decreasing dispersion as Rh-content decreases. Furthermore dispersion measurements provide insight into the expected activity of the catalyst, indicating

that catalyst formulations with higher Rh-content should exhibit superior reforming capabilities.⁸⁹

4.1.2. Inert vs. oxidative environment calcination

The distinct behavior of the pure Pt system required further investigation since this formulation did not adhere to the expected trend of decreasing dispersion with increasing calcination temperature. Calcination in an oxidative environment (air) was performed for all five catalyst formulations followed by dispersion measurements through CO chemisorption. A comparison of the dispersion profiles for catalysts calcined in an inert and the oxidative environment is shown in

Figure 4.

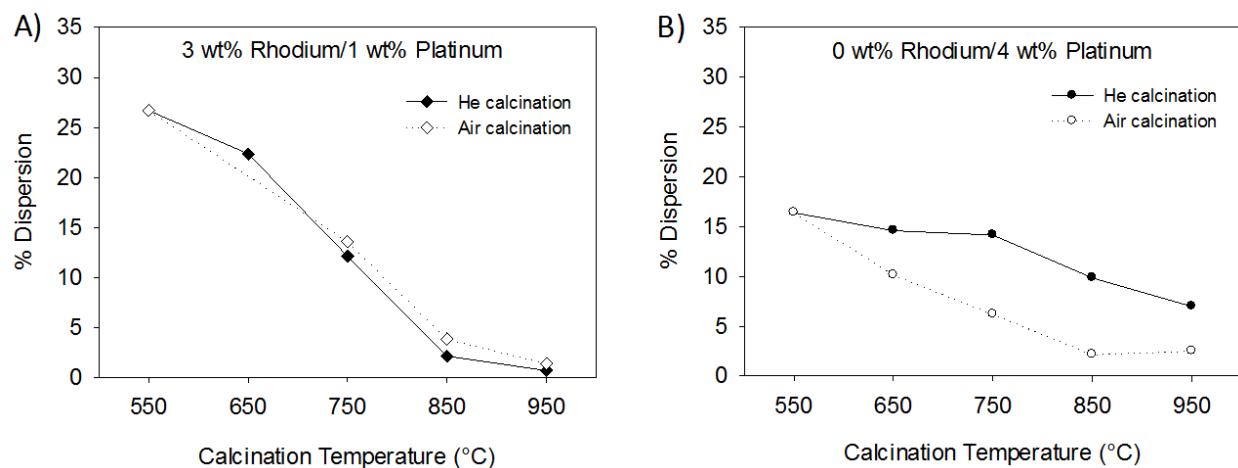


Figure 4: Dispersion of precious metals on silica-zirconia support as a function of calcination temperature in an inert (solid symbols) and oxidative (open symbols) environment for A) 3 wt% Rh/1 wt% Pt and B) 0 wt% Rh/4 wt% Pt. Inert environment calcination profiles reproduced from data presented in Table 3 and Figure 3.

When calcined in an oxidative environment, the measured dispersion values for Rh-containing catalysts are comparable to the values obtained when calcined in an

inert environment. Comparative profiles for 3 wt% Rh/1 wt% Pt catalyst are shown in Figure 4A and are representative for all Rh-containing formulations. However, those for the pure platinum catalyst (Figure 4B) are greatly reduced. This is likely due to the higher volatility and mobility of platinum oxide versus platinum metal species in the reduced state.^{90,91} Therefore, it is expected that the platinum oxide species formed during reforming of oxygenated species will result in decreased catalytic activity for catalyst formulations with higher Pt content.

4.2. SEM and TEM

Scanning electron microscopy (SEM) images were taken of the 3 wt% Rh/1 wt% Pt catalyst (same as in Figure 4) exposed to various calcination temperatures for a visual representation of any macroscopic morphological changes. These images are shown in Figure 5.

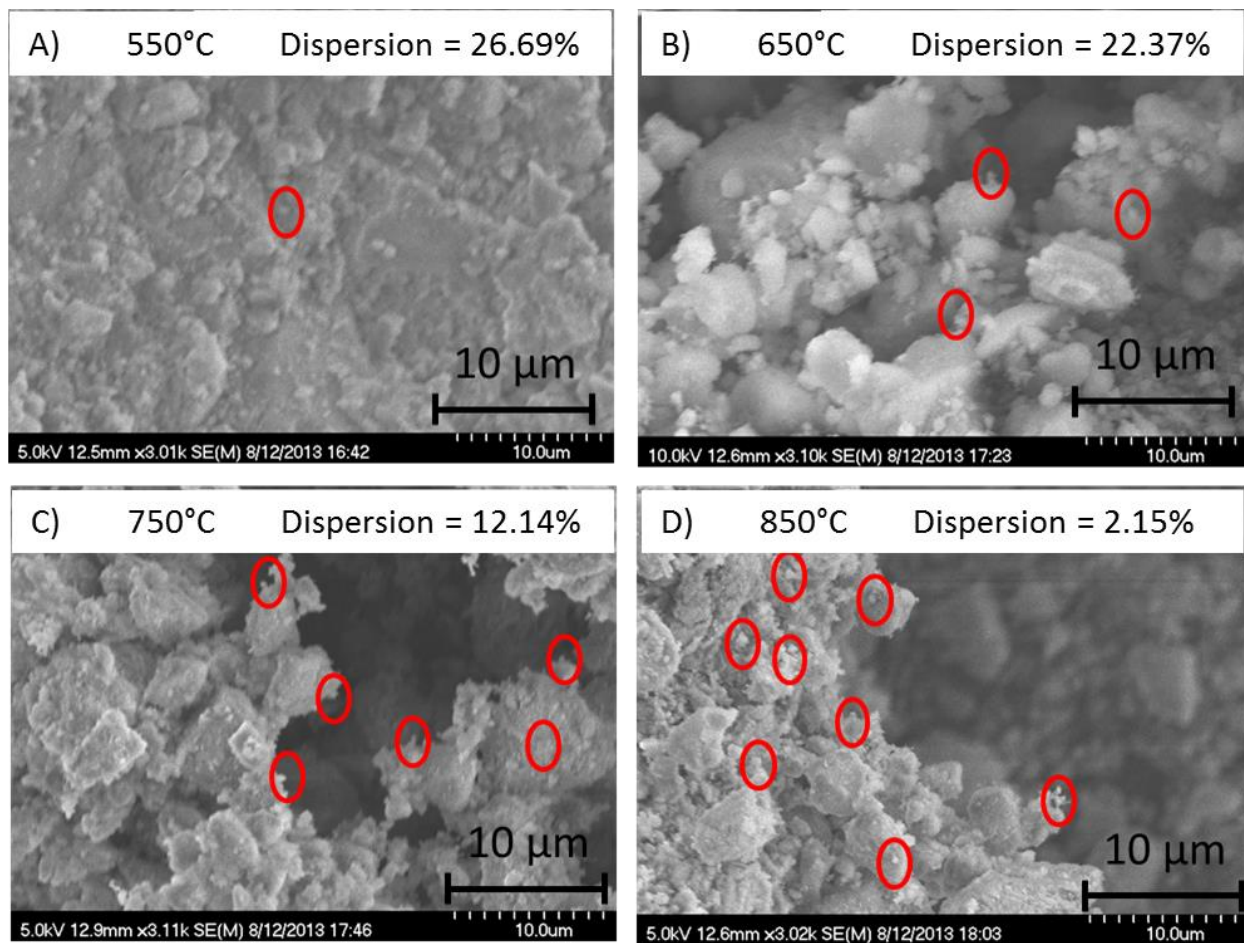


Figure 5: SEM images of 3 wt% Rh/1 wt% Pt on silica-zirconia calcined at (A) 550°C, (B) 650°C, (C) 750°C, and (D) 850°C) with sub-micron crystallites highlighted in red circles.

Calcination temperature and measured dispersion values are reproduced across the top of each image. As calcination temperature is increased we observe the emergence of sub-micron particles on the surface of the material which correlates well to the observed dispersion measurements.

Higher resolution transmission electron microscopy (TEM) images were taken to confirm the agglomeration of the precious metals as shown in Figure 6.

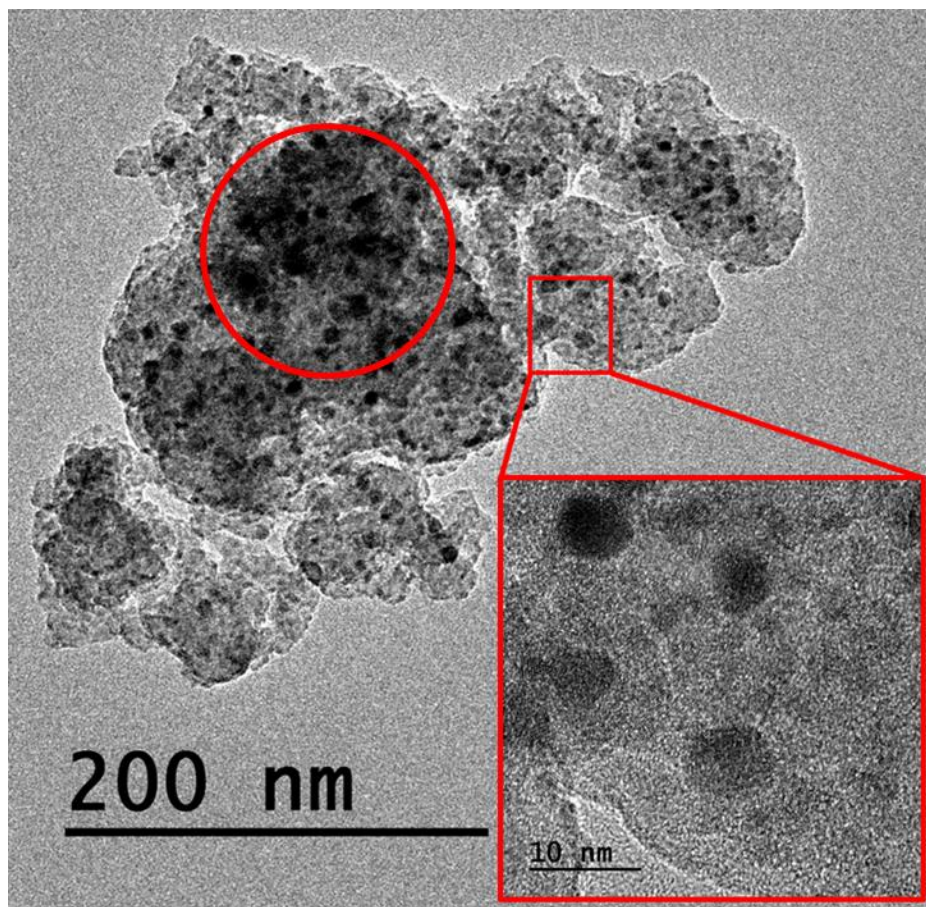


Figure 6: TEM images of 3 wt% Rh/1 wt% Pt on silica-zirconia calcined at 850°C. Dark black spots indicate the presence of precious metal nanoparticles as confirmed with EDS.

The dark spots in the TEM image indicate the precious metal nanoparticles. A large central deposit has been induced by the elevated calcination temperature indicated by the red circle. When we expand the image in the red square, a defined lattice can be observed for the precious metal nanoparticles depicted by the dark spots on the bulk of the material. Therefore, the sub-micron crystallites observed in SEM images (Figure 5) were confirmed to exhibit agglomeration of the precious metal nanoparticles. Furthermore, TEM imaging indicates that the nanoparticles themselves have a size on the order of 10 nm, thereby accounting for the decrease in dispersion measured by CO chemisorption. As a means of more fully understanding

the nature of the precious metal nanoparticles, the inherent lattice structure provides an impetus for a characterization of crystal structure.

4.3. X-ray diffraction

XRD measurements were also done on the 3 wt% Rh/1 wt% Pt formulation calcined at temperatures ranging from 550°C to 950°C to observe any changes in crystal structure. A distinctive peak at $2\theta = 41^\circ$ emerged as the calcination temperature was increased as shown in Figure 7.

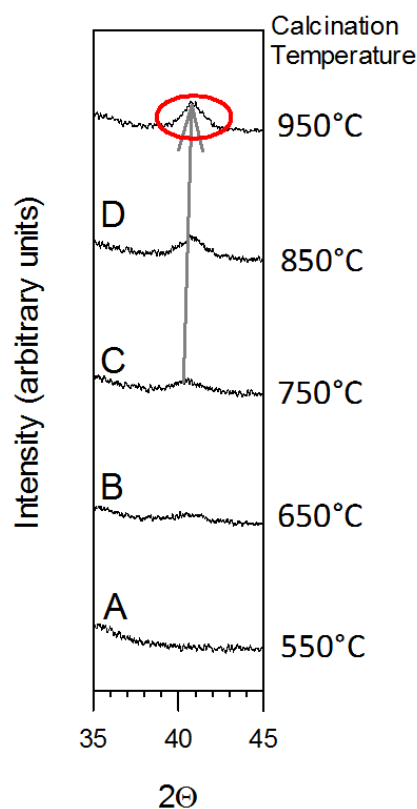


Figure 7: XRD profiles for 3 wt% Rh/1 wt% Pt on silica-zirconia support calcined at various temperatures.

This peak, correlating to the (111) reflection of the Rh-Pt where the d-spacing was calculated to be 2.25 Å according to Bragg's Law, suggests an agglomeration of the

precious metal nanoparticles as a function of increasing calcination temperature⁹² consistent with the dispersion measurements performed by CO chemisorption. The peak at $2\theta = 41^\circ$ is not apparent for the lower calcination temperatures (550°C and 650°C) since the precious metal nanoparticles are smaller, whereby the amorphous nature of the carrier obscures the crystal structure. Furthermore this peak was shown to drift slightly (change in $2\theta = 0.5^\circ$) toward a higher 2θ as a function of increasing calcination temperature. This phenomenon suggests that the oxidation state of the metals is changing during this process^{93,94} with a shift toward a more oxidized metal species.

4.4. Conclusions

The features of the catalytic systems detailed above successfully demonstrate that the surface of the catalysts is not stagnant, but changeable in response to various stimuli. Factors such as dispersion and crystallinity of the precious metals can be measurably altered through synthesis parameters. Higher calcination temperatures resulted in increased size and crystallinity of the precious metal nanoparticles, giving rise to a more ordered system. The accessibility of catalytically active sites as well as the precious metal lattice of the nanoparticles should have profound impacts on catalyst activity. These characterizations allow for a better understanding of the performance observed for each catalyst.

Chapter 5: Catalyst performance during ethanol steam reforming

Ethanol reforming experiments were performed in a packed bed continuous-flow reactor. The following conditions were used during each fuel reforming experiment: S/C = 1.5, GHSV = 44,000 hr⁻¹, calcination temperature: 650°C, reforming temperature: 650°C, and 1 atm. The catalysts were pre-reduced in a 5% H₂ in N₂ mixture at 400°C for 2 hours and purged of residual H₂ with pure N₂ for 1 hour prior to exposure to reaction conditions to ensure the state of the catalyst was consistent. Reaction products were quantified using the micro GC.

5.1. Hydrogen activity of various catalyst formulations

The hydrogen activity of all catalyst formulations was determined by plotting the measured mole percent hydrogen as a function of time on stream as shown in Figure 8.

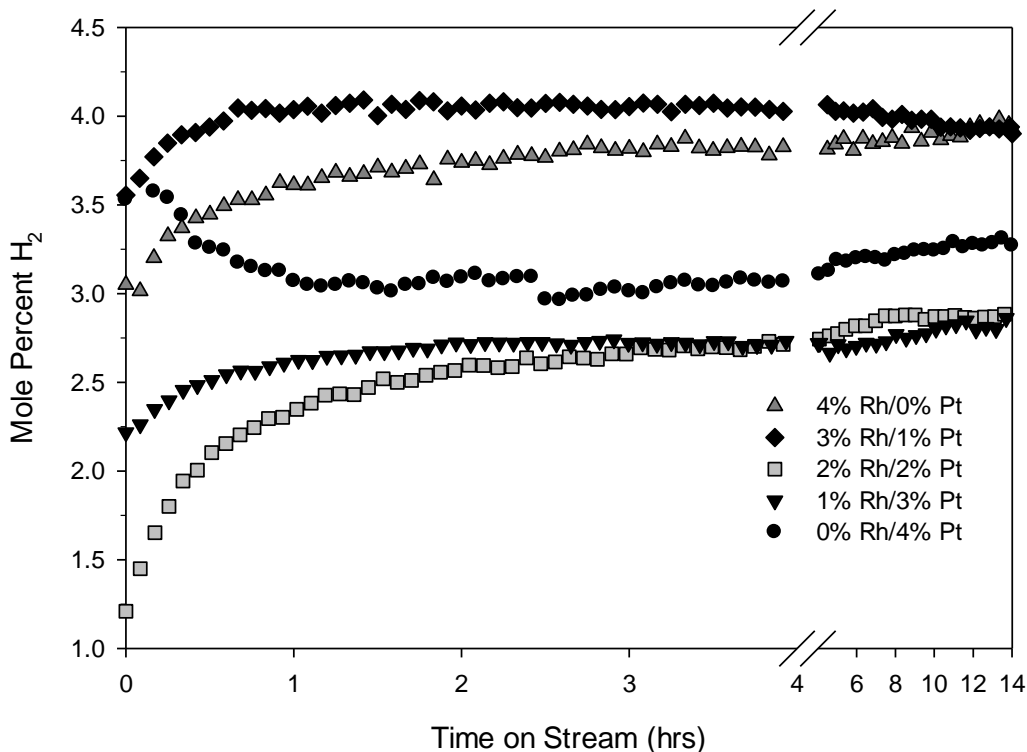


Figure 8: Hydrogen production of various single metal and bimetallic Rh-Pt catalyst formulations. All catalysts were calcined at 650°C under He and pre-reduced in 5% H₂ in N₂. Reaction conditions: S/C = 1.5, volumetric GHSV = 44,000 hr⁻¹, calcination temperature: 650°C, reforming temperature: 650°C, and 1 atm.

The rhodium-containing catalysts exhibited higher activity toward hydrogen than the pure platinum catalyst. Interestingly, the 3 wt% Rh/1 wt% Pt catalyst achieves a higher value for the production of hydrogen at $t = 1$ hour than the pure Rh catalyst yet both exhibit nearly identical behavior after 12 hours. This indicates that the selectivity toward hydrogen changes dynamically as a function of time on stream, suggesting that changes in the conformation or oxidation state of the precious metal nanoparticles occur as the metal participates in the reaction. The initial increase in measured percent hydrogen further suggests that there is an

induction period during which there is a change to the catalyst. Below we will demonstrate that the reduced surface of the precious metals becomes partially oxidized. As the reaction is allowed to continue, the oxidation state and conformation of the bimetallic and the pure rhodium system become more similar as indicated by their similar performance.⁹⁵

As a means to directly compare the performance of the prepared catalyst formulations, their activity normalized to the available metal active sites was calculated in the form of a turnover frequency (TOF). Table 4 shows the calculated turnover frequency (TOF) at 45 minutes on stream for each of the catalyst systems described above under the previously established reforming conditions. These values were calculated using Equation (14) shown below:

$$TOF = \frac{\text{Molar Flow Rate of } H_2 \left(\frac{mol}{s}\right)}{\text{Active Metal Sites (mol)}} = \frac{\dot{N}_T \cdot n_{H_2,prod}}{\frac{g_{cat} \cdot \%PM \cdot D}{M_{PM}}} \quad (14)$$

where \dot{N}_T is the total molar flow rate and $n_{H_2,prod}$ is the mole% of hydrogen produced. All other variables are identical to those described in Equation (13).

Table 4: Turnover frequencies (TOFs) for all catalyst formulations. Reaction conditions: S/C = 1.5, GHSV = 44,000 hr⁻¹, calcination temperature: 650°C, reforming temperature: 650°C, and 1 atm.

Catalyst Formulation	Rh (wt%)	Pt (wt%)	TOF (mol/mol · s)
A	4	0	4.4 x 10 ³
B	3	1	5.3 x 10 ³
C	2	2	5.0 x 10 ³
D	1	3	11.9 x 10 ³
E	0	4	11.6 x 10 ³

While it is apparent that the 1 wt% Rh/3 wt% Pt catalyst formulation has the highest TOF, there are several factors to consider. The high TOF for formulations D and E indicates that they are most active, i. e. Pt increases activity, however the dispersion is much lower. This is shown in Figure 8 with the diminished hydrogen production, thus overall activity is lower. If dispersion could be not only increased, but *maintained*, these formulations should exhibit superior reforming capabilities.

5.2. Stability of highest performing formulation

The dynamic nature of the catalyst has been shown through various characterization techniques and initial performance screening via H₂ production. Pretreatment as well as the reaction environment in which the catalyst experiences have drastic effects on the dispersion, crystal structure, and oxidation state of the precious metals.⁵¹ While these factors provide a basis for understanding how the precious metals interact with their reaction environment, it is difficult to accurately predict how these elements will combine to determine catalytic activity.

Therefore, ethanol reforming experiments were performed under the same reforming conditions previously described. A typical product distribution profile for ethanol reforming performed over the catalyst formulation with the highest hydrogen activity, 3 wt% Rh/1 wt% Pt, is shown in Figure 9.

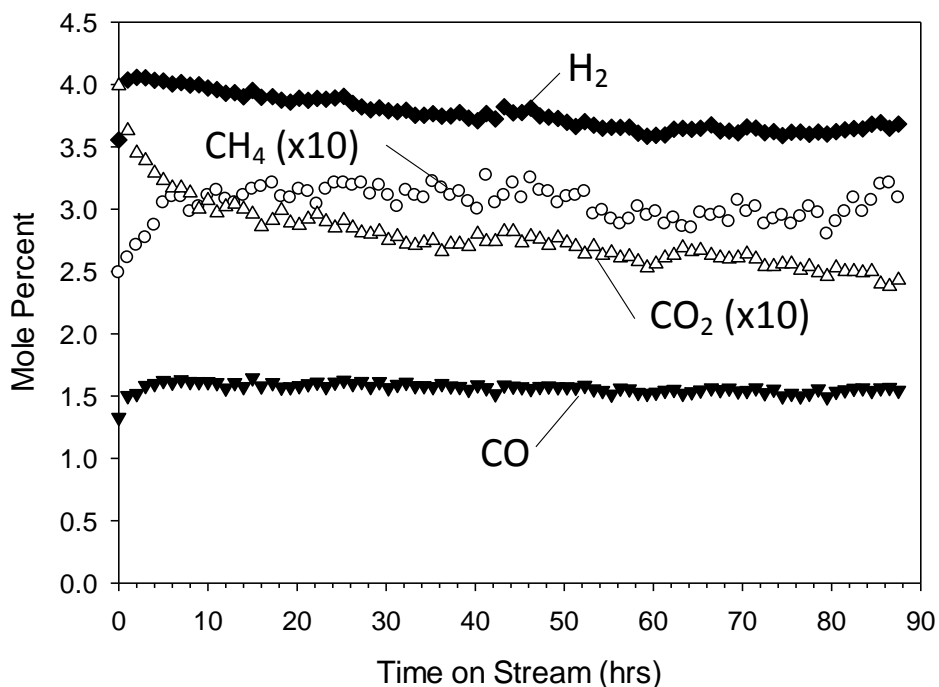


Figure 9: Product distribution for the steam reforming of ethanol at 650°C over pre-reduced 3 wt% Rh/1 wt% Pt on silica-zirconia as a function of time on stream. Reaction conditions: S/C = 1.5, GHSV = 44,000 hr⁻¹, calcination temperature: 650°C, reforming temperature: 650°C, and 1 atm.

After an initial induction period of roughly one hour the system exhibits near-equilibrium hydrogen production of 4.05 mole% with a slow decrease to 3.75 mole% over the course of 60 hours on stream. A trade-off in the production of CO₂ and CH₄ as a function of time on stream can also be observed, yet the measured amount of CO remains constant throughout the entire test. This is likely due to the

predominantly Rh(111) surface present in the catalyst, as shown through XRD, where methyl hydrogen abstraction is thought to occur followed by rapid dehydrogenation to CO and surface carbon.⁹⁶

5.3. Reforming temperature and pretreatment

Keeping all other conditions the same, activity data was generated at a reforming temperature of 350°C. A calcination temperature of 550°C was used for these experiments to ensure the surface was thermally stable during the test. This provides insight into the surface reconfiguration by separating the combined thermal and chemical effects (i.e. tests done at 650°C with a catalyst calcined at 650°C) versus just chemical (i.e. reaction species). To further explore these phenomena, ethanol reforming was performed at the previously mentioned conditions (calcination temperature: 550°C, reforming temperature: 350°C) with the exception of the pretreatment in 5% H₂ in N₂. The product distributions for these tests are shown in Figure 10.

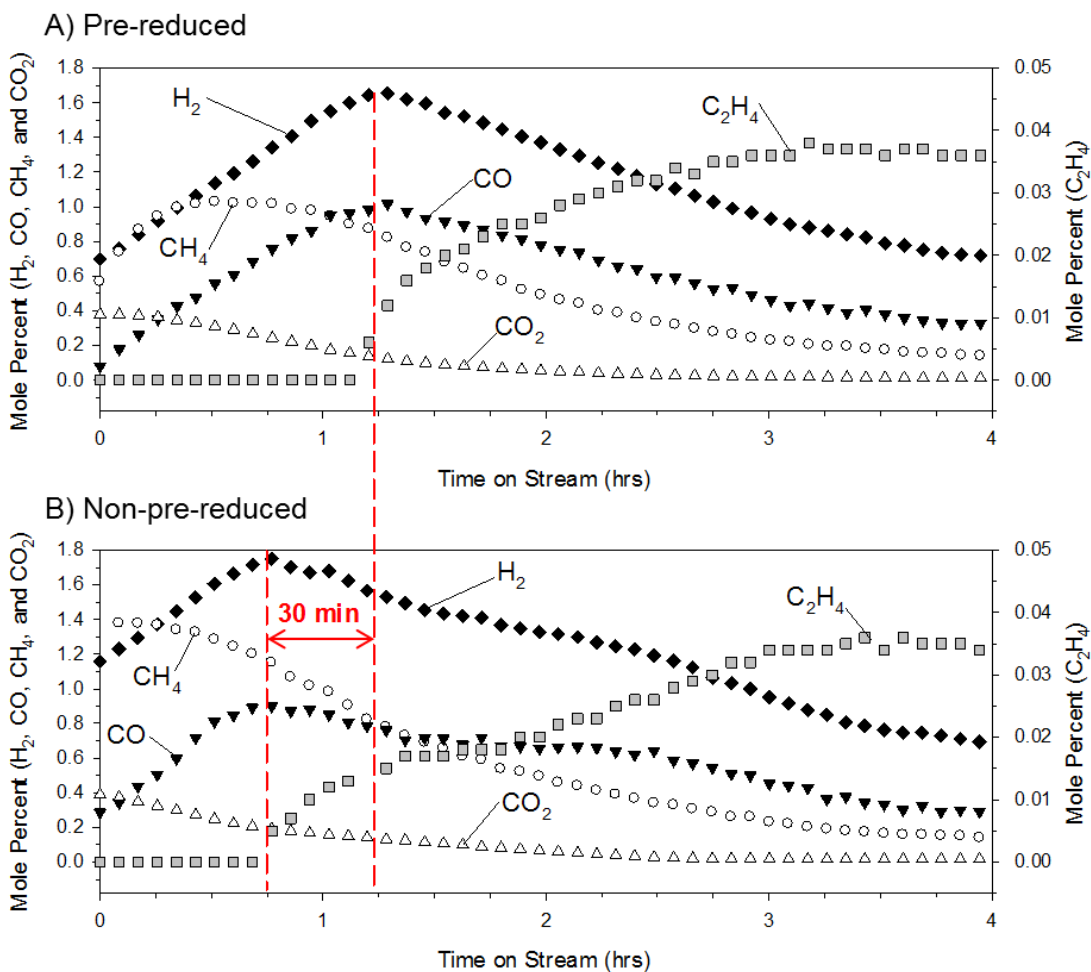


Figure 10: Product distribution for the low-temperature steam reforming of ethanol over (A) pre-reduced 3 wt% Rh/1 wt% Pt on silica-zirconia and (B) non-pre-reduced 3 wt% Rh/1 wt% Pt on silica-zirconia as a function of time on stream. Reaction conditions: S/C = 1.5, GHSV = 44,000 hr⁻¹, calcination temperature: 550°C, reforming temperature: 350°C, and 1 atm.

In Figure 10A, the product distribution changes drastically within the first 4 hours with a new byproduct (ethylene, C₂H₄) detected after t = 1.25 hours. At t = 0 similar trends are observed for the product distribution as those observed when reforming at the higher temperature. These include the highest CO₂ production which immediately decreases, no ethylene (C₂H₄) detected, and a steady increase in the production of H₂, CO, and CH₄. Interestingly the initial amount of CO₂ produced

is identical to that produced at the higher reforming temperature at 0.40 mole%. If one considers the heat produced by the water-gas shift reaction as a product in the equilibrium scheme, it would be expected that a lower reforming temperature would allow for more generation of heat, thereby shifting the reaction equilibrium toward the products. The fact that the reforming temperature has no effect on the initial amount of carbon dioxide produced indicates that something else is limiting the reaction.

Differences in the product distributions due to reforming at different temperatures first become apparent at $t = 0.50$ hr in Figure 10A when the methane production reaches a maximum and starts to decrease. This is followed by the maxima of H_2 and CO and the first detectable production of C_2H_4 all occurring at $t = 1.25$ hr. This data suggests that the catalytically active material changes dynamically during the reaction perhaps due to the exposure of reaction species, resulting in a change in the product distribution and the formation of intermediates and byproducts not previously observed.

To further explore these findings ethanol reforming was performed at the previously mentioned conditions (calcination temperature: $550^\circ C$, reforming temperature: $350^\circ C$) except that the pretreatment in 5% H_2 in N_2 was eliminated. The product distribution for this initially oxidized system is shown in Figure 10B. Ethanol reforming over catalysts both with and without pretreatment in 5% H_2 in N_2 have several distinct features, the most notable is a shift in the time to achieve maximum hydrogen production and the first detectable levels of ethylene.

The delay of 30 minutes between the pre-reduced and non-pre-reduced profiles for hydrogen and ethylene production likely indicates a morphology change, an oxidation state change, or both.

5.4. Conclusions

At the relatively elevated temperature of 650°C, the catalysts with higher Rh content (formulations A and B) achieved turnover frequencies on the order of 10^3 while formulation B exhibited near-equilibrium (4.034 mole%) production of hydrogen. In light of these results, the product distribution and amount of hydrogen produced are improved by the addition of Rh for primarily Pt-containing catalysts and is optimized with a Rh:Pt ratio of 3:1 in primarily Rh-containing catalysts. Subsequent tests confirm that the 3 wt% Rh/1 wt% Pt catalyst is capable of producing hydrogen at near-equilibrium concentrations (4.034 mole%) for 90+ hours.

For low-temperature ethanol steam reforming, the pre-reduced catalyst is in the zero oxidation state at $t = 0$ undergoing subsequent activation in the first 1.25 hours on stream at which point we observe the maximum in hydrogen production. The non-pre-reduced catalyst exhibits similar activation, but initial hydrogen production is the same as that of the pre-reduced catalyst after 30 minutes on stream. This suggests that partially oxidized metal particles on the catalyst exhibit a higher level of activity in this reaction, but after a certain amount of conformation or oxidation state change, activity decreases as evidenced by the decrease in hydrogen production and the emergence of ethylene. Furthermore the system must

achieve a certain amount of hydrogen production before any byproducts are detected. This likely indicates a competition between oxidation of metal surface sites and reduction due to hydrogen that becomes available to the system.

Chapter 6: Conformational changes through *operando* X-ray analysis

To investigate the apparent oxidation state and conformational changes presented in Chapter 5, *operando* X-ray measurements were performed during ethanol steam reforming over the most active catalyst formulation, 3 wt% Rh/1 wt% Pt on SiO₂-ZrO₂, as well as the single-metal Rh and Pt formulations using a Nashner-Adler reactor (see Appendix B.1).

In X-ray absorption fine structure (XAFS), the sample is exposed to a range of X-rays of known energies. For X-rays of a single energy, a portion of these X-rays are absorbed by the sample causing the emission of a core electron. The intensity of the incident X-ray beam can be compared to the intensity of the that transmitted through the sample to quantify the amount of absorption that occurs. By scanning through a range of X-rays a spectrum is created and within this spectrum there exists a sharp rise in absorption energy above a threshold incident energy. This sharp rise is known as the absorption edge and can provide information on the oxidation state of the material being characterized. Furthermore, a series of smaller peaks or oscillations exist at energies above the edge that are indicative of the atomic spacing in the sample.^{97,98}

6.1. Product Distribution

While the product distribution differed slightly from that obtained using a packed bed reactor, overall trends were observed to be the same with dynamic behavior occurring as a function of time on stream as shown in Figure 11.

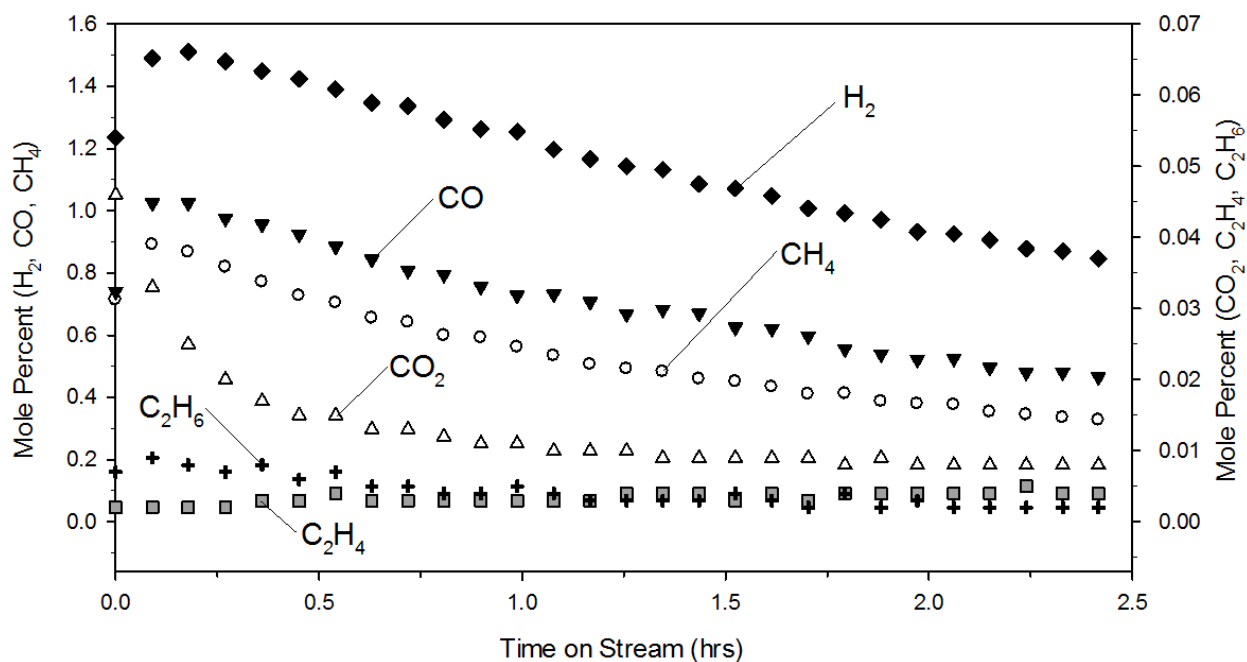


Figure 11: Product distribution for the steam reforming of ethanol at 350°C over 3 wt% Rh/1 wt% Pt on silica-zirconia as a function of time on stream in a Nashner-Adler reaction cell with *operando* X-ray analysis.

Similar features of the product distribution, including the brief activation and subsequent deactivation of the catalyst indicated by the H₂ profile, indicate that the same changes to the catalyst are occurring during reaction as those observed for a packed bed reactor. This setup is therefore appropriate for *operando* XANES and EXAFS analysis of the catalyst during ethanol steam reforming.

6.2. XANES

The relative oxidation state of the precious metal nanoparticles can be observed through XANES analysis. In XANES, the shielding effect of oxygen bound to the metal surface results in a shift of the edge step to higher energies. The more oxidized the sample, the more energy is necessary to observe the edge step.⁹⁸ In our studies, the oxidation state of the precious metal nanoparticles was observed by obtaining fluorescence XANES spectra. The Rh K-edge spectra are shown in Figure 12 for the bimetallic catalyst at each stage of the ethanol reforming experiment.

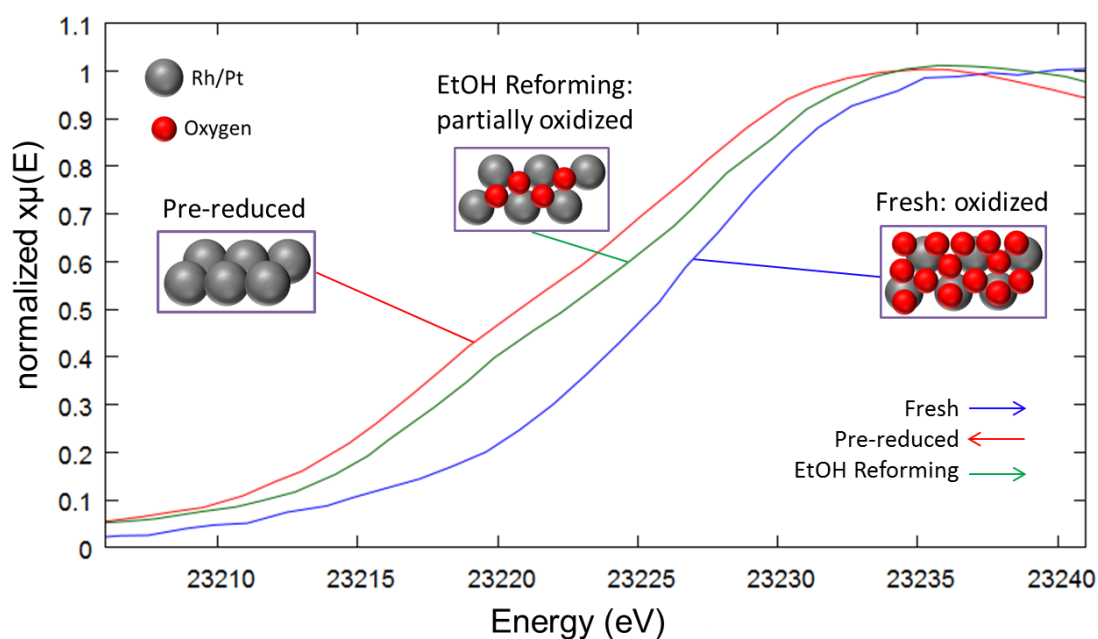


Figure 12: Rh K-edge XANES spectra under *operando* ethanol reforming conditions. Arrows within the legend indicate direction of edge shift for each stage of ethanol reforming. Idealized graphics of the catalyst surface are shown for clarity.

The shift of absorption edge indicates the change of the chemical state of the material. Fresh catalyst, having been calcined in air, is shown to be the most

oxidized with the highest energy edge step observed. A marked shift in edge step energy toward lower levels by roughly 5 eV is observed after the pre-reduction step, consistent with a Rh foil standard indicating that the catalyst surface is completely reduced after pretreatment. During ethanol reforming, the edge shifts towards higher energy indicating a more oxidized state of Rh without reaching the fully oxidized state of the fresh catalyst.

6.3. EXAFS

To investigate the observed deactivation of the catalyst and the contribution of conformational changes within the precious metal nanoparticles, EXAFS spectra were obtained. In EXAFS, the small oscillations discussed previously are isolated by subtracting the smooth background absorption coefficient ($\mu_0(E)$) from the measured absorption coefficient ($\mu(E)$) and normalized to the step in absorption coefficient at the threshold energy ($\Delta\mu_0(E)$) as shown in Equation (15).

$$\chi(E) = \frac{\mu(E) - \mu_0(E)}{\Delta\mu_0(E)} \quad (15)$$

Here $\chi(E)$ represents the EXAFS function. The oscillations are best described by a wave function, k , defined according to Equation (16).

$$k = \sqrt{\frac{2m(E - E_0)}{\hbar^2}} \quad (16)$$

Here m is the mass of an electron and \hbar is Planck's constant. Ultimately, the EXAFS equation can be written as shown in Equation (17).

$$\chi(k) = \sum_j \frac{N_j S_0^2 f_j(k) e^{-2k^2 \sigma_j^2}}{k R_j^2} \sin[2k R_j + \delta_j(k)] \quad (17)$$

Here N is the number atoms neighboring the excited atom, S_0^2 is the passive electron reduction factor, $f(k)$ is the scattering amplitude, $\delta(k)$ is the phase shift, R is the distance to the neighboring atom, and σ^2 is the disorder.⁹⁹ The Fourier transform of $\chi(k)$ gives rise to the R-space spectrum, which is an efficient way to represent the atomic radial distribution function. These parameters ultimately provide information on the distance between atoms, the number of nearest neighboring atoms, structural disorder, and the type of neighboring atoms, making this technique appropriate for the characterization of bimetallic catalysts.¹⁰⁰

EXAFS spectra of the 3 wt% Rh/1 wt% Pt catalyst were collected at both the Rh K-edge and Pt L₃-edge were obtained for several stages of the reforming experiment: after pre-reduction at 350°C, post ethanol reforming at 350°C, and post ethanol reforming at room temperature (RT). In each figure, the reference spectra (denoted “foil”) are shown for comparison. The Rh spectra are shown in Figure 13.

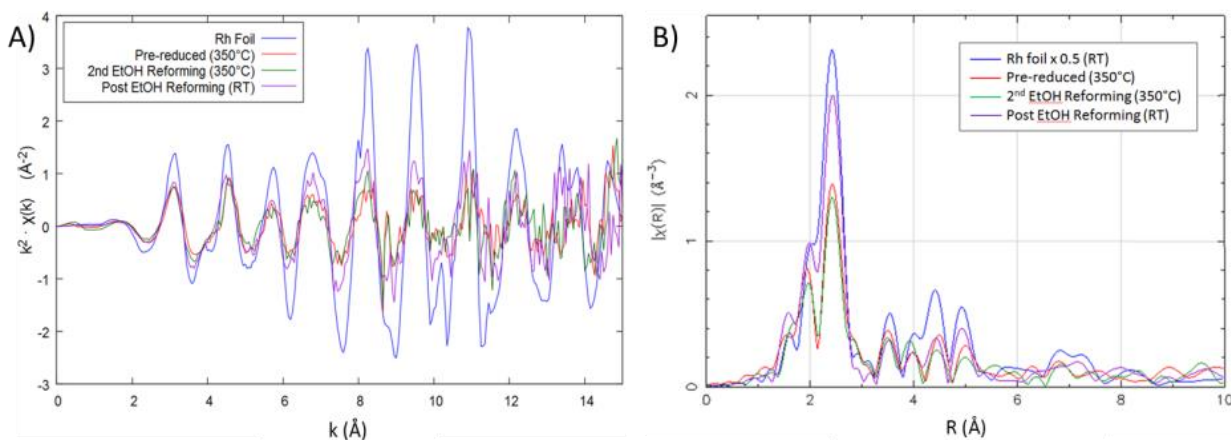


Figure 13: Rh K-edge EXAFS spectra under *operando* ethanol reforming conditions in A) k-space and B) R-space for the 3 wt% Rh/1 wt% Pt catalyst.

The k-space spectral features (Figure 13A) in all conditions are very similar, though less pronounced, to those of Rh foil. This suggests the Rh atoms have a similar local structure to that of Rh foil, consistent with the fact that the precious metal nanoparticles are composed primarily of Rh.

In R-space (Figure 13B), the spectral shape of the sample is quite similar with that of Rh foil (blue). All spectra show a pronounced peak in the range of 1.8 – 3.0 \AA , which can be mainly attributed to the prevalence of Rh-Rh bonds. The peak intensity of the spectra taken at the reaction temperature of 350°C and room temperature could not be directly compared because at high temperature both the disorder factor and coordination number of metal-metal bonds would affect the height of the peak. For the spectra taken at the higher temperature after ethanol reforming (green), the peak intensity decreases slightly compared to the spectrum before reaction (red). Similar spectra of the sample were taken at the Pt L_3 -edge as shown in Figure 14.

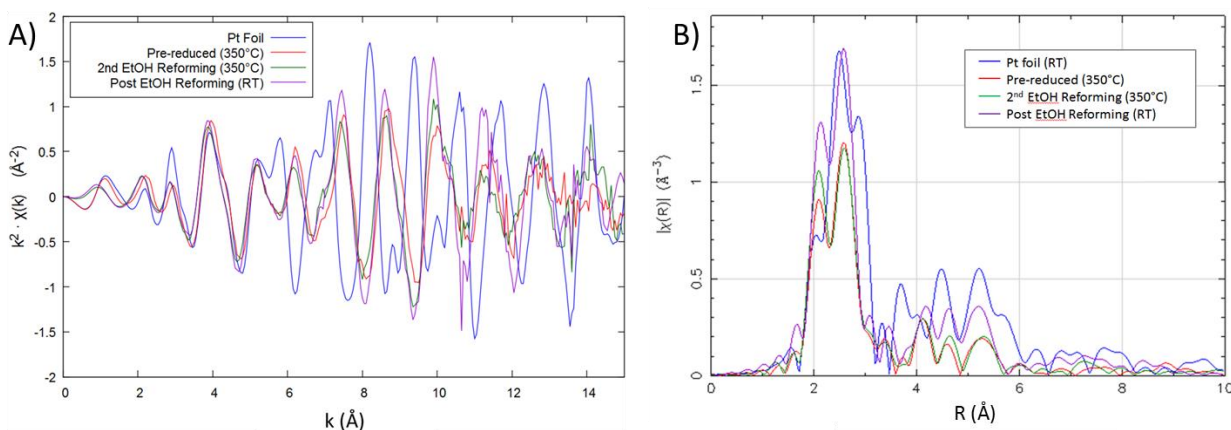


Figure 14: Pt L₃-edge EXAFS spectra under *operando* ethanol reforming conditions in A) k-space and B) R-space for the 3 wt% Rh/1 wt% Pt catalyst.

In both k-space and R-space, the spectral features for the sample under all conditions were different from that of Pt foil. This suggests Pt atoms have different local structure from Pt foil, providing evidence for the prevalence of Pt-Rh bonds.

The spectral difference between the sample and Pt foil can also be seen in the R-space spectra (Figure 14B). Compared to Pt foil, the shoulder peak at roughly 2 Å in the sample spectra is relatively high, which suggests that there are Rh atoms in the local structure of Pt.¹⁰¹ The Rh- and Pt-edge EXAFS data provide support for conformational changes occurring within the catalyst, thereby necessitating XAFS modeling for more detail on the dynamic nature of precious metal nanoparticle structure.

6.4. XAFS fitting

As discussed in section 6.3, structural changes to the catalyst require examination of both the Pt-Rh path and Rh-Pt path for XAFS fitting. For Rh-edge data, the model includes two paths: Rh-Rh and Rh-Pt. Similarly, the model for Pt-

edge data also includes two paths: Pt-Pt and Pt-Rh. To provide proper constraints to the bond distance and disorder factor, multi-data fitting was performed for the Rh-edge data and Pt-edge data under the same conditions. Thus, the bond distance and disorder factor of Rh-Pt were constrained to be the same with Pt-Rh allowing for direct comparison. The fit spectra are in agreement with the experimental spectra and are available in the supplemental information (Figure A.2). Results are shown in Table 5.

Table 5: Summary of XAFS fitting results for the 3 wt% Rh/1 wt% Pt catalyst during several stages of ethanol reforming.

<i>Rh-edge</i>					
Condition	Bond	N	R (Å)	$\sigma^2(\text{Å}^2)$	ΔE (eV)
Pre-reduced (350°C)	Rh-Rh	7.0±0.7	2.66±0.01	0.008±0.003	-1.8±1.2
	Rh-Pt	2.1±1.0	2.679±0.005	0.005±0.001	-1.8±1.2
Post EtOH reforming (350°C)	Rh-Rh	5.5±0.7	2.66±0.01	0.006±0.003	-3.6±1.4
	Rh-Pt	2.4±1.0	2.684±0.009	0.003±0.001	-3.6±1.4
Post EtOH reforming (RT)	Rh-Rh	6.9±0.5	2.69±0.01	0.005±0.001	-2.1±1.0
	Rh-Pt	1.3±0.7	2.696±0.006	0.003±0.001	-2.1±1.0

<i>Pt-edge</i>					
Condition	Bond	N	R (Å)	$\sigma^2(\text{Å}^2)$	ΔE (eV)
Pre-reduced (350°C)	Pt-Pt	1.1±0.4	2.68±0.01	0.000±0.002	8.2±0.6
	Pt-Rh	4.7±0.4	2.679±0.005	0.005±0.001	8.2±0.6
Post EtOH reforming (350°C)	Pt-Pt	1.8±0.8	2.70±0.02	0.000±0.003	7.9±1.0
	Pt-Rh	4.0±0.7	2.684±0.009	0.003±0.001	7.9±1.0
Post EtOH reforming (RT)	Pt-Pt	1.4±0.7	2.69±0.02	0.001±0.002	8.9±0.8
	Pt-Rh	5.2±0.7	2.696±0.006	0.003±0.001	8.9±0.8

Both Rh and Pt naturally exhibit a face-centered cubic crystal lattice, implying a coordination number of 12. The fact that the precious metal nanoparticles in the catalyst are under coordinated with a highest total coordination number of 9.1 ± 1.2

(Rh-edge, pre-reduced at 350°C condition) provide support that a strained conformation is contributing to catalytic activity.

When the scattering atom is Rh, the Rh-Rh coordination number decreases from 7.0 ± 0.7 after pre-reduction to 5.5 ± 0.7 during ethanol reforming and the Pt-Rh coordination number decreases from 4.7 ± 0.4 to 4.0 ± 0.7 . However, when the scattering atom is Pt, the Rh-Pt coordination number increases from 2.1 ± 1.0 after pre-reduction to 2.4 ± 1.0 during ethanol reforming and the Pt-Pt coordination number increases from 1.1 ± 0.4 to 1.8 ± 0.8 . This provides clear evidence that the precious metal nanoparticles restructure as a function of time on stream, suggesting that this conformational change might explain the previously unaccounted for deactivation of the catalyst.

Several possible configurations of the nanoparticles could result from the restructuring observed. The Ferrando group identified four main possibilities for the structure of a bimetallic particle: core shell, metal-segregated, alloy or mixed metal, and three-shell. An idealized depiction of the various structures is reproduced from Ferrando *et al.* in Figure 15.¹⁰²

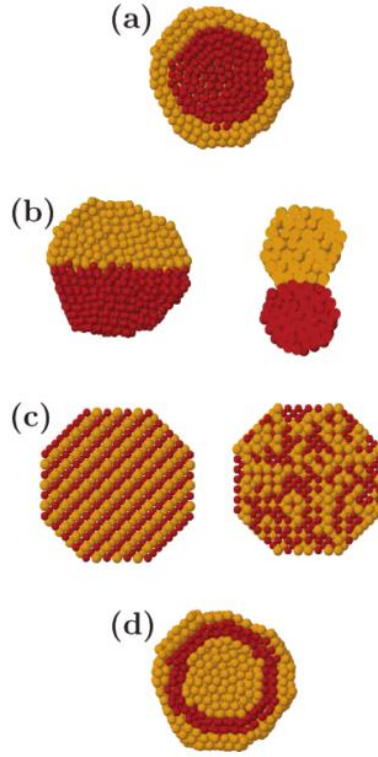


Figure 15: Idealized representation of a A) core-shell, B) metal segregated, C) alloy or mixed metal, and D) three-shell nanoparticle atomic configuration. [Ferrando *et al.* 2008]

The presence of an alloy for a bimetallic species with metals “A” and “B” can be determined by comparing the ratio (R) of their coordination numbers with the ratio of the molar concentrations. A true alloy is formed if the ratio of the coordination numbers of metal A to metal A and metal A to metal B equals the ratio of the molar concentration of metal A to that of metal B as defined in Equation (18).

$$R_{A-B} = \frac{N_{AA}}{N_{AB}} = \frac{x_A}{x_B} \quad (18)$$

Here N_{AA} and N_{AB} are the coordination numbers of metal A to metal A and metal A to metal B respectively and x_A and x_B are the molar concentrations of A-type and B-type atoms in the sample. For the 3:1 ratio of Rh:Pt by weight, the molar ratio can be calculated as follows in Equation (19):

$$\frac{x_{Rh}}{x_{Pt}} = \left(\frac{3 \text{ wt\% Rh}}{1 \text{ wt\% Pt}} \right) \left(\frac{195.1 \frac{g}{mol} Pt}{102.9 \frac{g}{mol} Rh} \right) = 5.7 \quad (19)$$

Indicating that the molar ratio between Rh and Pt is 5.7. If the calculated ratio of the coordination numbers ($N_{Rh-Rh} \cdot N_{Rh-Pt}$ and $N_{Pt-Rh} \cdot N_{Pt-Pt}$) matches the molar ratio ($x_{Rh}/x_{Pt} = 5.7$), this indicates the presence of an alloy of the two metals. A summary of the ratios of coordination numbers is shown in Table 6.

Table 6: Calculated coordination number ratios for 3 wt% Rh/1 wt% Pt under reforming conditions.

	Pre-reduced (350°C)	Post EtOH Reforming (350°C)	Post EtOH Reforming (RT)
N_{Rh-Rh}/N_{Rh-Pt}	3.3 ± 1.6	2.3 ± 1.0	5.3 ± 2.8
N_{Pt-Rh}/N_{Pt-Pt}	4.3 ± 1.6	2.2 ± 1.1	3.7 ± 1.9

For the pre-reduced catalyst, the coordination number ratios are smaller than the molar ratio between Rh and Pt ($x_{Rh}/x_{Pt} = 5.7$), suggesting that the bimetallic nanoparticle is not a random alloy. After reforming ethanol, the coordination number ratios decrease when measured at the operating temperature of 350°C. This observed change can most likely be attributed to the further segregation of Pt and Rh into single-metal clusters. Interestingly, when the sample is cooled to room temperature in an inert environment and analyzed under *in-situ* conditions, the coordination number ratios increase, almost to the original values calculated for the pre-reduced catalyst. This shows that a conformational change is occurring during reaction and is having an effect on catalyst performance. Furthermore, this change

would have been completely overlooked if *in situ* characterization had been performed versus *operando*.

6.5 Conclusions

The findings presented in this chapter suggest that the most active phase of the Rh is a partially oxidized species as indicated in Figure 12. Furthermore, the structure of the precious metal nanoparticles is changing as a function of time on stream, potentially offering an explanation for irreversible catalyst deactivation observed previously.⁵¹

Chapter 7: Mechanistic insights through using isotope-labeled reactants

Isotope labeling is a longstanding technique used to gain insight into the likelihood of a particular reaction pathway.⁷⁷⁻⁷⁹ In this way, information has been gleaned on the various roles of water in the steam reforming process. In the field of fuel reforming, Song *et al.* have performed work using this method to determine the adsorption and desorption behavior of reactants using deuterated (²H or D) ethanol and water.⁸⁰ Their results indicated that dissociated OD groups from D₂O were combining with H atoms present due to the dissociation of ethanol. Furthermore, deuterated water and water-¹⁸O were used to investigate the reaction pathway of ethanol and water over ceria- and zirconia-supported cobalt.⁸¹ They found that the oxidation of ethanol occurs at the catalyst surface due to the presence of C¹⁸O¹⁶O since surface oxygen must participate in the reaction. While this work expounded

the role of water, the contribution of each C atom within ethanol to the overall reforming behavior remained unclear. The authors highlight that it is unclear how the C-containing species are formed during reaction.⁸⁰ Here we seek to provide new insights on the Rh-based catalyst that we have recently shown dynamically changes oxidation states during reforming¹⁰³ by using strategically labeled reactants of both ethanol and water.

7.1. Reactant selection and operating conditions

Through employing both isotope-labeled ethanol *and* isotope-labeled water, it is now possible to track the atomic partitioning of the reactants into the products. This allows for a more complete understanding of ethanol and water as reactants and how they combine to give rise to the products. Chemical formulas of the reactants, ethanol-1-¹³C and water-¹⁸O are shown in Figure 16.

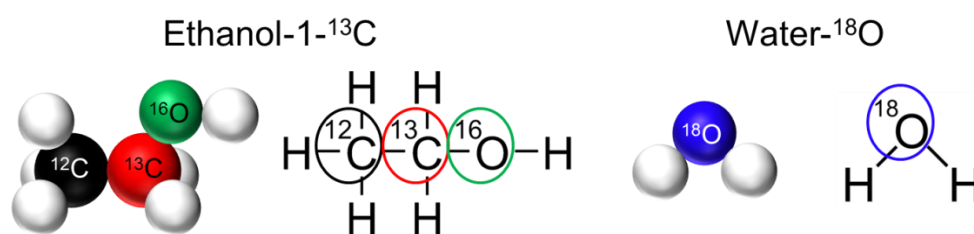


Figure 16: Isotope-labeled reactants, ethanol-1-¹³C and water-¹⁸O.[Crowley *et al.* 2016]

In this study, isotope enrichment was 99 atom% ¹³C for ethanol-1-¹³C and 97.40 atom% ¹⁸O for water-¹⁸O as confirmed by GC-MS. All non-H-atoms can be distinguished from one another, allowing for atom origin differentiation.

7.2. Kinetic isotope effect

By substituting one of the atoms within the reactants for a heavier isotope, a change has been made to the vibrational energies within ethanol and water. Ultimately this suggests that the reaction rate will change. A quantification of the change in rate of the reaction when an atom in a reactant is replaced with one of its isotopes, known as the kinetic isotope effect (KIE), was determined to be minimal for ethanol-1-¹³C and water-¹⁸O. KIEs were determined using the method described by Singleton *et al.*¹⁰⁴ as shown in Equation (19).

$$KIE_i = \frac{k_{m_{i1}}}{k_{m_{i2}}} = \sqrt{\frac{m_{i2}}{m_{i1}}} \quad (19)$$

where i is the species, k is the reaction rate constant, m_{i1} is the molecular weight of the non-isotope-labeled species, and m_{i2} is the molecular weight of the isotope-labeled species. The KIE for ethanol-1-¹³C and water-¹⁸O were calculated to be 1.01 and 1.05 respectively, showing that the behavior of the isotope-labeled system is nearly the same as when using non-labeled reactants.

7.3. Product distribution vs time on stream

Isotope-labeled ethanol steam reforming was performed over 4 wt% Rh, 4 wt% Pt, and 3 wt% Rh/1 wt% Pt on SiO₂-ZrO₂ catalysts to observe the partitioning of each non-hydrogen atom within the makeup of the reactants into the products as well as determine the contribution of each metal to the overall product distribution.

Bare SiO₂-ZrO₂ was found to be inactive in the process. All isotope-labeled ethanol steam reforming experiments were performed in a packed bed reactor at reaction conditions identical to those in section 5.3: S/C = 1.5, GHSV = 44,000 hr⁻¹, calcination temperature: 550°C, reforming temperature: 350°C, and 1 atm.

The overall product distribution profiles for ethanol reforming over each of the three aforementioned catalyst formulations is shown in Figure 17. Conversion of ethanol, X_{EtOH} , was calculated according to Equation (20).

$$X_{EtOH} = \frac{n_{EtOH,in} - n_{EtOH,out}}{n_{EtOH,out}} \quad (20)$$

The product distribution changed dynamically within the first 4 hours on stream across all three catalyst formulations and was consistent with earlier work presented in Section 5.3. Evidenced in Figure 17A, initially there was a steady increase in the amount of H₂ and CO produced for the bimetallic catalyst formulation. CH₄ also increased initially, but reached a maximum after roughly 10 minutes then steadily decreased. The highest CO₂ production was observed at t = 0, which immediately decreased. Ethane (C₂H₆) was produced at a near-constant rate during the first 1.25 h on stream while no ethylene (C₂H₄) was detected. The most notable feature occurred at roughly 1.25 h; maxima were observed in H₂ and CO production followed by a steady decrease, indicating catalyst deactivation. This is supported by the conversion of ethanol falling below 100% at the same time. Furthermore a selectivity change from ethane to ethylene was simultaneously

observed, stabilizing in production after 2.25 h on stream with ethylene concentrations of 0.007 mole% with no ethane detected.

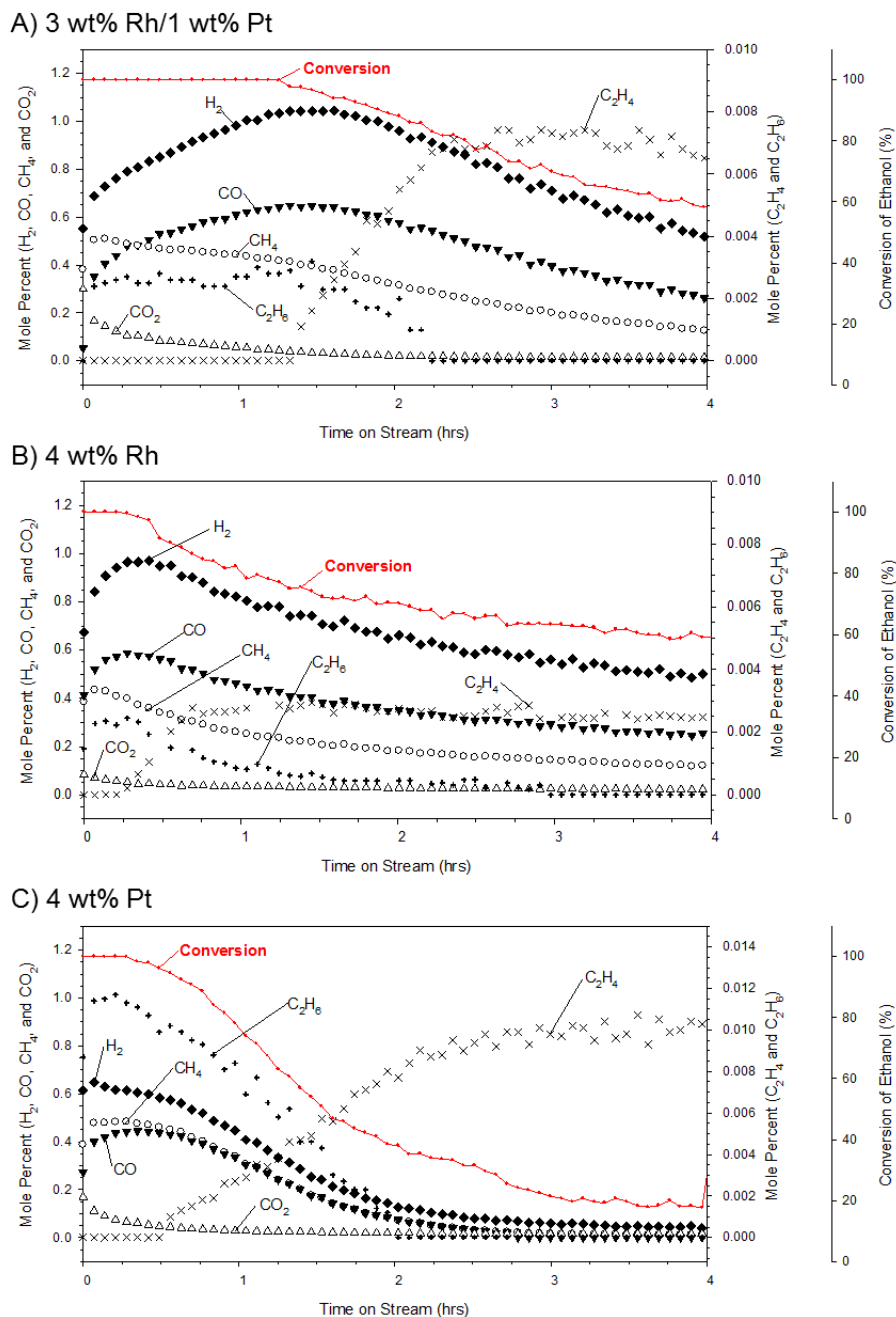


Figure 17: Product distribution profile for the reforming of ethanol-1-¹³C with water-¹⁸O over (A) 3 wt% Rh/1 wt% Pt, (B) 4 wt% Rh, and (C) 4 wt% Pt on SiO₂-ZrO₂ support. Reaction conditions: S/C = 1.5, GHSV = 44,000 hr⁻¹, calcination temperature: 550°C, reforming temperature: 350°C, and 1 atm. [Crowley *et al.* 2016]

Interestingly, the single metal catalyst formulations (Figure 17B and C) showed signs of deactivation after 0.5 h on stream as opposed to 1.25 h for the bimetallic. Overall, similar reforming behavior was observed between the 3 wt% Rh/1 wt% Pt (Figure 17A) and 4 wt% Rh (Figure 17B) formulations, not surprisingly given that they are both primarily Rh-containing catalysts, with the bimetallic formulation providing the highest level of H₂ production at its maximum. However, the 4 wt% Pt catalyst (Figure 17C) exhibited a much lower selectivity to H₂ and increased selectivity to the C₂ species, suggesting Pt is less capable of breaking the C-C bond within ethanol.

Thus far we have shown what is commonly reported in the literature: the amount of each product detected as a function of time on stream. However, the origins of the atoms within each product are still unknown. Through examining the isotopic breakdown of individual species, we can now determine how the reactants partition into the products giving us quantitative mechanistic insight.

7.4. Isotopic composition of products

The atomic distribution of reactants into products is shown for the most active catalyst formulation, 3 wt% Rh/1 wt% Pt, in Figure 18.

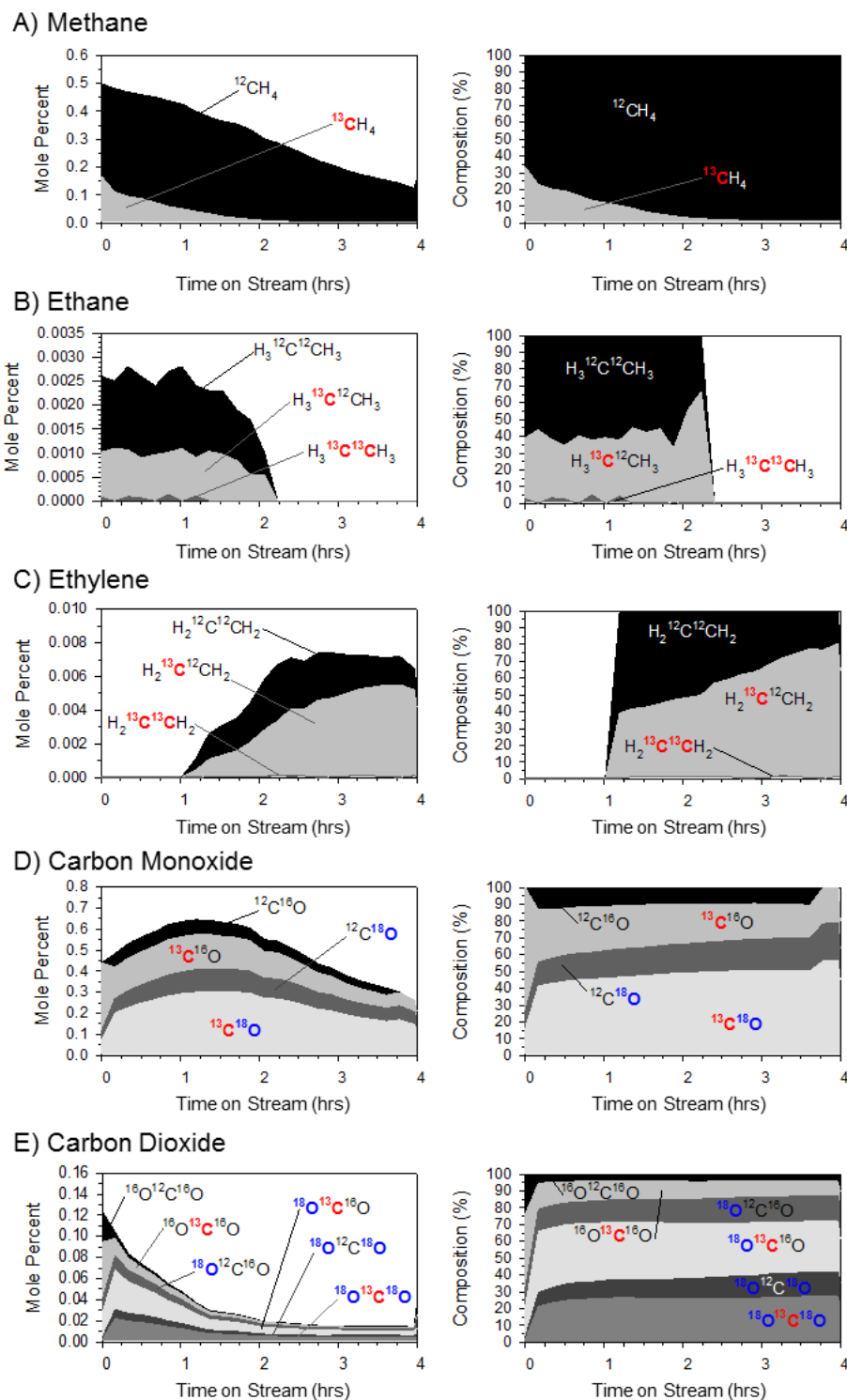


Figure 18: Atomic partitioning of ^{12}C , ^{13}C , ^{16}O , and ^{18}O shown as part of the total amount detected (left) and as percent composition (right) into (A) methane, (B) ethane, (C) ethylene, (D) carbon monoxide, and (E) carbon dioxide over 3 wt% Rh/1 wt% Pt on $\text{SiO}_2\text{-ZrO}_2$. Bold colored text indicates isotope labeling. [Crowley *et al.* 2016]

In Figure 18, the total mole percent as a function of time on stream (reproduced from Figure 17A) is shown on the left with shaded areas representing each type of compound detected with respect to isotope-labeled species. Percent composition of each isotope species is presented on the right. The simplest isotope-labeled product differentiation occurs in methane (CH_4). Two forms of methane are possible, $^{12}\text{CH}_4$ and $^{13}\text{CH}_4$, and both were detected as shown in Figure 18A. For the bimetallic catalyst, a maximum amount of $^{13}\text{CH}_4$ was detected initially at levels of 0.18 mole% (33% of total methane) which decreased to 0.01 mole% (1.6% of total methane) after 2.25 h on stream. This is surprising since $^{13}\text{CH}_4$ formation requires both the ^{12}C - ^{13}C and the ^{13}C - ^{16}O bonds in the ethanol to break, not to mention the dynamics of the various H-bonds.

Similar behavior was observed for the 4% Rh catalyst formulation, though $^{13}\text{CH}_4$ was detected at a maximum of 10% total methane rather than 33% as shown in Figure 19A. Under identical reforming conditions, the 4 wt% Pt catalyst formulation provided lower, near constant $^{13}\text{CH}_4$ levels of 2% total methane shown in Figure 20.

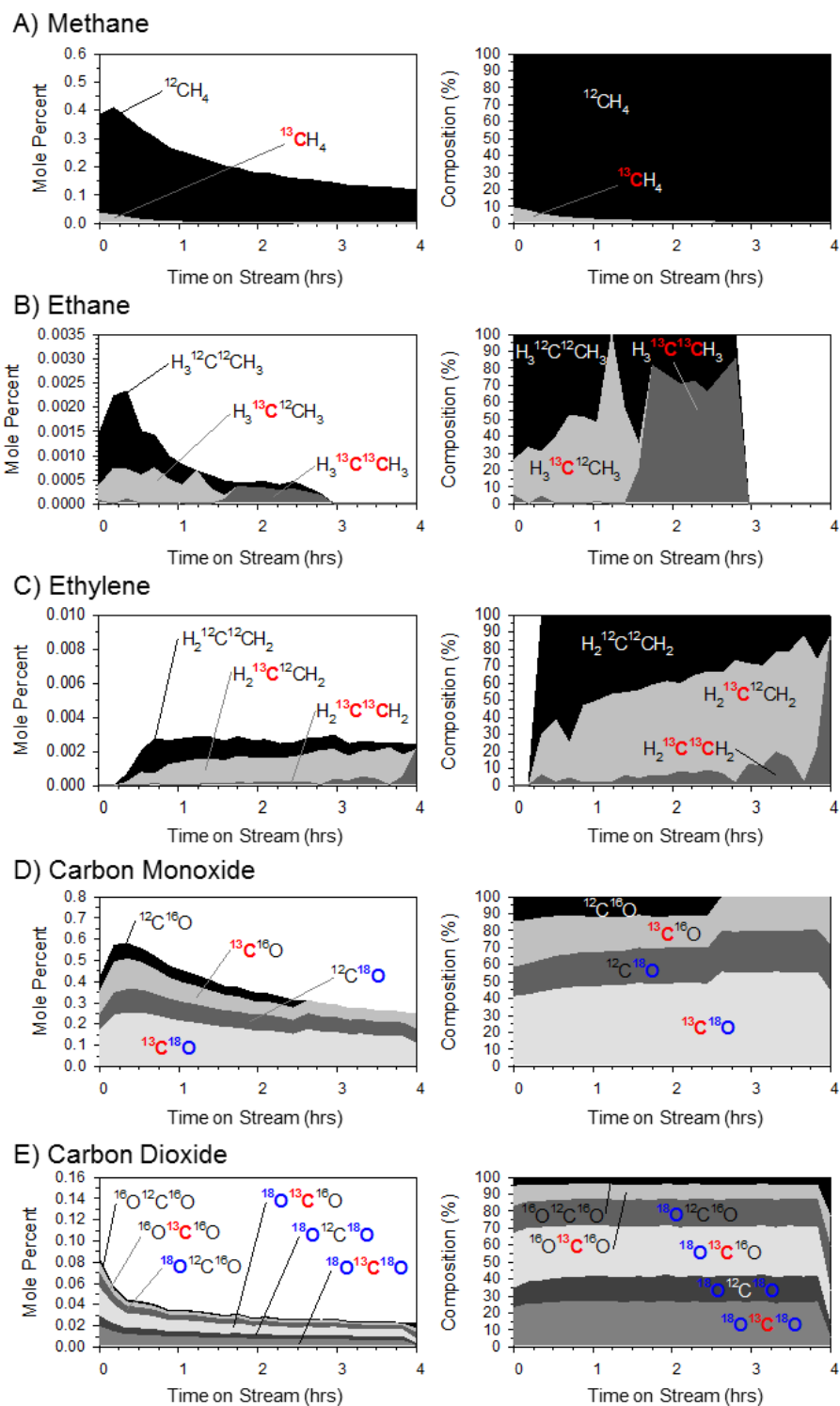


Figure 19: Atomic partitioning of ^{12}C , ^{13}C , ^{16}O , and ^{18}O shown as part of the total amount detected (left) and as percent composition (right) into (A) methane, (B) ethane, (C) ethylene, (D) carbon monoxide, and (E) carbon dioxide over 4 wt% Rh on $\text{SiO}_2\text{-ZrO}_2$. Bold colored text indicates isotope labeling. [Crowley *et al.* 2016]

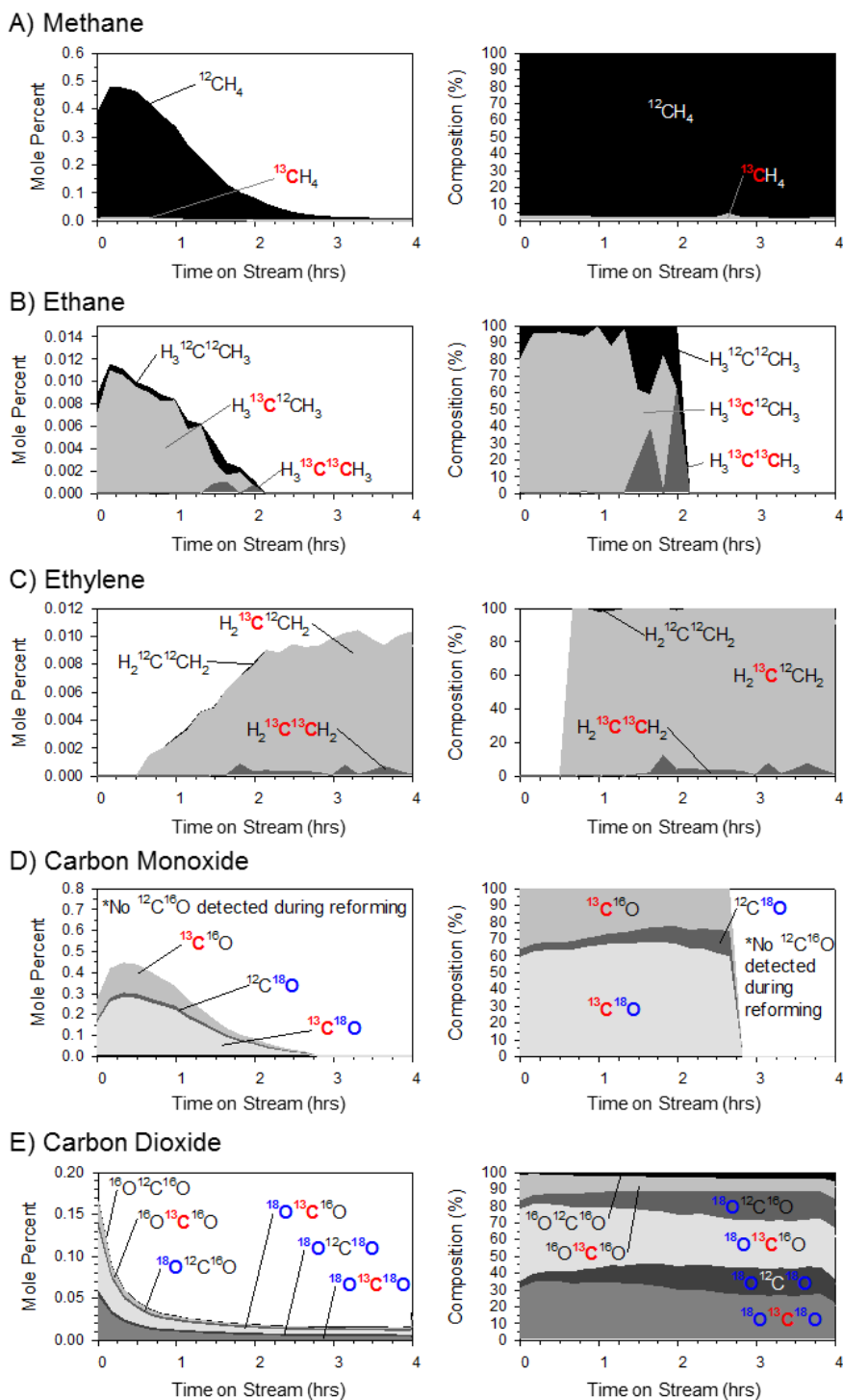


Figure 20: Atomic partitioning of ^{12}C , ^{13}C , ^{16}O , and ^{18}O shown as part of the total amount detected (left) and as percent composition (right) into (A) methane, (B) ethane, (C) ethylene, (D) carbon monoxide, and (E) carbon dioxide over 4 wt% Pt on $\text{SiO}_2\text{-ZrO}_2$. Bold colored text indicates isotope labeling. [Crowley *et al.* 2016]

A summary of the carbon isotope partitioning for methane across the three catalyst formulations studied is shown in Table 7.

Table 7: Isotope product distribution for CH₄ during ethanol reforming across three catalyst formulations.

CH ₄ Isotope	Time	Catalyst Formulation		
		3% Rh/1% Pt	4% Rh	4% Pt
¹² CH ₄	Initial	66.4%	75.7%	97.8%
	Final	98.4%	96.9%	
¹³ CH ₄	Initial	33.6%	24.3%	2.2%
	Final	1.6%	3.1%	

It should be noted that the initial and final percentages of ¹²CH₄ and ¹³CH₄ were identical for the single-metal Pt catalyst formulation. From these data sets, Rh appears to be more capable of breaking the C-C bond in ethanol than Pt with either the ¹²C-¹³C bond breakage rate decreasing with time on stream, or the breakage rate remaining constant while selectivity toward other ¹³C-containing products increases. This would account for the decrease in observed ¹³CH₄ across all formulations. However the monotonic decline in the methane for all catalyst formulations suggests the ¹²C-¹³C bond scission becomes less favored since the concentration profiles change more abruptly for other ¹³C product species. This will be discussed further with respect to the C₂-species.

Similar tracking was performed for the C₂H_x and CO_y products shown parts B through E in Figure 18-Figure 20. For the 3 wt% Rh/1 wt% Pt formulation, the ethane formed (Figure 18B) is initially observed to have a composition of 60.8% H₃¹²C¹²CH₃ which decreases to 33.3% of the total amount of ethane produced over

the first 2 h of ethanol reforming. Since the two ^{12}C atoms must come from two separate ethanol-1- ^{13}C molecules, this shows that the ethane formation pathway occurs primarily via breaking the ^{12}C - ^{13}C bond within ethanol-1- ^{13}C and recombination with another ^{12}C species, consistent with the formation of the heavy methane. Similar behavior is observed for the Rh-only catalyst formulation as shown in Figure 19B.

As discussed by Vesselli *et al.*, it is likely that the ^{12}C - ^{13}C bond within ethanol-1- ^{13}C is cleaved prior to recombination with a separate ^{12}C species.⁷² Following this logic, it seems that the abundance of $\text{H}_3^{13}\text{C}^{12}\text{CH}_3$ at levels of 35-45% can be attributed to first a breaking of the ^{12}C - ^{13}C bond within ethanol-1- ^{13}C followed by breaking of the ^{13}C - ^{16}O bond, thereby allowing the ^{12}C and the ^{13}C moieties to recombine into ethane. This theory is further supported by the presence of $\text{H}_3^{13}\text{C}^{13}\text{CH}_3$. Even though this form of ethane is detected at very low levels (~1 ppm), the only way for this molecule to form is through breaking the ^{13}C - ^{16}O and the ^{12}C - ^{13}C bonds in ethanol, allowing two ^{13}C species to recombine into ethane. On the contrary, the Pt-only catalyst formulation yields ethane with $\text{H}_3^{13}\text{C}^{12}\text{CH}_3$ making up nearly 95% of total ethane (Figure 20B), further demonstrating that Pt is ineffective at breaking the C-C bond within ethanol. A summary of the carbon isotope partitioning for ethane across the three catalyst formulations studied is shown in Table 8.

Table 8: Isotope product distribution for C₂H₆ during ethanol reforming across three catalyst formulations.

C ₂ H ₆ Isotope	Time	Catalyst Formulation		
		3% Rh/1% Pt	4% Rh	4% Pt
H ₃ ¹² C ¹² CH ₃	Initial	60.8%	74.1%	19.9%
	Final*	33.3%	15.2%	38.2%
H ₃ ¹³ C ¹² CH ₃	Initial	36.2%	20.7%	79.7%
	Final*	66.7%	ND	ND
H ₃ ¹³ C ¹³ CH ₃	Initial	3.1%	5.2%	0.4%
	Final*	ND	84.8%	61.8%

*Final time denotes the last time at which C₂H₆ was observed.

ND: Not detected

For all catalyst formulations, however, much of the ¹³C goes to the CO_x species, thus maintaining a low H₃¹³C¹³CH₃.

A similar explanation can be applied to ethylene (part C of Figure 18-Figure 20) with similar trends observed across the three catalyst formulations. It is clear that ethylene and ethane formation have a strong correlation since there is nearly an exact time match when the formation of ethane (all isotopes) declines and ethylene concentration increases. Due to this selectivity change, it would appear that a portion of the ethylene is formed directly from the ethane via the gas-phase dehydrogenation pathway.^{105,106} However, this reaction is extremely slow in the gas phase at the operating temperature of 350°C.¹⁰⁷ Therefore, the ethane that is observed must be formed through ethylene hydrogenation [Equation (12)] on the catalyst surface, a commonly reported feature of supported platinum group metal catalysts.^{108–110} We hypothesize that the tradeoff between ethane and ethylene production observed at $t = 1.25$ h implies that the ethylene hydrogenation reaction

is suppressed as the catalyst deactivates, consistent with the emergence of ethylene as a stable product and the simultaneous decreases in H₂ and ethanol conversion.

However, the amount of ethylene observed cannot be solely attributed to the prevention of the ethylene hydrogenation reaction. Stable ethylene production was observed at levels of 0.007 mole% during ethanol steam reforming over the 3 wt% Rh/1 wt% Pt catalyst formulation. Since stable ethane production was observed at roughly 0.003 mole%, this leaves 0.004 mole% (57%) of ethylene unaccounted for. By examining the corresponding isotope labeled components of ethane and ethylene, insight can be gained into the most likely ethylene production pathway. For both ¹²C-¹²C and ¹³C-¹³C ethane and ethylene, the amount observed before and after the tradeoff in selectivity at t = 1.25 h indicates that the ethylene hydrogenation reaction is completely shut down for ethylene formed from identical C atoms from ethanol. The ethane and ethylene containing both ¹²C and ¹³C, however, are a different matter. H₃¹³C¹²CH₃ is observed at 0.001 mole% during stable ethane production whereas H₂¹³C¹²CH₂ is observed at 0.005 mole% during stable ethylene production. Thus, the 0.004 mole% of unaccounted-for ethylene observed is entirely present as H₂¹³C¹²CH₂. Therefore, the decrease in ¹³CH₄ observed as well as the minimal H₂¹³C¹³CH₂ detected provide support for the ethanol dehydration pathway [Equation (4)] being the most likely source of ethylene production. A summary of the carbon isotope partitioning for ethane across the three catalyst formulations studied is shown in Table 9.

Table 9: Isotope product distribution for C₂H₄ during ethanol reforming across three catalyst formulations.

C ₂ H ₄ Isotope	Time	Catalyst Formulation		
		3% Rh/1% Pt	4% Rh	4% Pt
H ₂ ¹² C ¹² CH ₂	Initial*	58.3%	50.5%	ND
	Final	19.5%	23.7%	ND
H ₂ ¹³ C ¹² CH ₂	Initial*	40.3%	45.3%	99.2%
	Final	78.9%	58.4%	98.7%
H ₂ ¹³ C ¹³ CH ₂	Initial*	1.4%	4.2%	0.8%
	Final	1.6%	17.9%	1.3%

*Initial time denotes time at which C₂H₄ was first detected.

ND: Not detected

The products become increasingly more complex for the CO_y species in that there are two options for the carbon atom (¹²C and ¹³C) and two options for the oxygen atom(s) (¹⁶O and ¹⁸O). For the bimetallic and single metal Rh catalyst formulations, all four possible forms of carbon monoxide (part D of Figure 18 and Figure 19) are detected, proving that CO is not formed solely from the oxygen-bound carbon within ethanol. Interestingly, for the Rh-containing catalyst formulations, ¹³C¹⁸O accounts for nearly 50% of the total CO detected throughout the test, increasing to 65% during the last 15 minutes of reforming. This is clear evidence that the primary pathway for CO formation is through direct reaction between the ethanol and the water at the C-O bond within ethanol. Roughly 25% ¹³C¹⁶O was detected throughout the test, indicating that half as many ¹³C-¹⁶O bonds within ethanol-1-¹³C are preserved in CO formation. It can be seen that the ¹²C entity recombines with ¹⁸O from the water to form ¹²C¹⁸O, though only at 15% of the total

CO makeup. A summary of the carbon isotope partitioning for carbon monoxide across the three catalyst formulations studied is shown in Table 10.

Table 10: Isotope product distribution for CO during ethanol reforming across all catalyst formulations.

CO Isotope	Time	Catalyst Formulation		
		3% Rh/1% Pt	4% Rh	4% Pt
$^{12}\text{C}^{16}\text{O}$	Initial	11.5%	11.7%	ND
	Final	ND	ND	ND
$^{13}\text{C}^{16}\text{O}$	Initial	27.1%	22.6%	29.9%
	Final	21.6%	20.1%	32.2%
$^{12}\text{C}^{18}\text{O}$	Initial	16.0%	19.4%	5.2%
	Final	22.1%	24.7%	17.7%
$^{13}\text{C}^{18}\text{O}$	Initial	45.4%	46.3%	64.9%
	Final	56.3%	55.2%	50.1%

However, no $^{12}\text{C}^{16}\text{O}$ is detected at any point during reforming for the Pt-only catalyst formulation (Figure 20D). This is expected since, upon first inspection, it would seem that the only source of ^{16}O is the carbon-bound oxygen in ethanol- $1\text{-}^{13}\text{C}$. It would therefore be unlikely for the $^{13}\text{C}\text{-}^{16}\text{O}$ bond to break simply for the ^{16}O moiety to combine with a ^{12}C species on the catalyst. It is therefore surprising to find that $^{12}\text{C}^{16}\text{O}$ is present throughout the reforming experiment for the Rh-containing formulations. Thus, we propose that the CO formation pathway on Rh-containing catalysts occurs not only through recombination of the ethanol and water reactants themselves, but also with the oxygen within the catalyst support as the only other source for ^{16}O .

Oxygen exchange between water and silica and zirconia as well as oxygen mobility in catalyst supports has been well documented.^{111–115} Furthermore, tracking the composition of water in the effluent as a function of time on stream yielded a nearly constant isotopic concentration of H₂¹⁸O and H₂¹⁶O for all three catalyst formulations as shown in Table 11.

Table 11: Isotope product distribution for H₂O during ethanol reforming across all catalyst formulations.

H ₂ O Isotope	Catalyst Formulation		
	3% Rh/1% Pt	4% Rh	4% Pt
H ₂ ¹⁶ O	42.8%	46.6%	44.5%
H ₂ ¹⁸ O	56.7%	53.4%	55.5%

This proves that H₂¹⁶O is formed consistently throughout the test, either through oxygen exchange with the support or through the water-forming reactions of dehydration, reverse carbon gasification, and methanation [Equations (4),(10), and (11) respectively].

In addition, the CO₂ concentration profile for the bimetallic catalyst formulation (Figure 18E) reveals that initially the water gas shift reaction [Equation (9)] is occurring and gradually declines. Simultaneously, the CO concentration increases from 0.45 mole% at t = 0 to 0.65 mole% at t = 1.25 h—more than the amount that can be provided by the decomposition of CO₂ (0.15 mole%) to CO. Consequently, the likely CO_y species that initially forms on the catalyst is CO which undergoes further oxidation to CO₂, supplied with oxygen either from the Rh surface, the support itself, or water.

As evidenced, $^{12}\text{C}^{16}\text{O}$ is formed when the ^{12}C - ^{13}C bond within ethanol- 1 - ^{13}C is broken, freeing a ^{12}C species that remains on the surface of the catalyst, allowing for a reaction with ^{16}O in the support. This is supported quantitatively by a feature of the CO isotope product distribution for Rh-containing catalysts occurring after 3.75 h on stream for the bimetallic catalyst (Figure 18D) and 2.65 h on stream for the single-metal Rh catalyst (Figure 19D). At this point, $^{12}\text{C}^{16}\text{O}$ is no longer observed in the products, suggesting that the ^{16}O in the support near the metal-support interface has been completely depleted and replaced by ^{18}O from the labeled water.

In the case of the bimetallic catalyst, there is a possibility that after several hours on stream the metal nanoparticles are no longer a true alloy of Rh and Pt with Pt segregating to the surface, preventing recombination of the ^{12}C and ^{16}O species correlating with the observed behavior for the pure Pt catalyst formulation (Figure 20D). However, since this phenomenon is observed for the pure Rh catalyst, the oxygen exchange between the support and water at the catalyst-support interface is the most probable explanation for the observed behavior. A summary of the carbon isotope partitioning for carbon dioxide across the three catalyst formulations studied is shown in Table 12.

Table 12: Isotope product distribution for CO₂ during ethanol reforming across all catalyst formulations.

CO ₂ Isotope	Time	Catalyst Formulation		
		3% Rh/1% Pt	4% Rh	4% Pt
¹⁶ O ¹² C ¹⁶ O	Initial			33.8%
	Final	4.3%	4.5%	26.8%
¹⁶ O ¹³ C ¹⁶ O	Initial			6.0%
	Final	10.3%	8.9%	16.1%
¹⁸ O ¹² C ¹⁶ O	Initial			39.8%
	Final	14.3%	15.9%	28.8%
¹⁸ O ¹³ C ¹⁶ O	Initial			6.5%
	Final	32.5%	29.7%	16.5%
¹⁸ O ¹² C ¹⁸ O	Initial			12.1%
	Final	12.3%	14.8%	7.9%
¹⁸ O ¹³ C ¹⁸ O	Initial			1.8%
	Final	26.3%	26.2%	3.9%

Interestingly, all six possible species of CO₂ are detected throughout the reforming experiments for all three catalyst formulations. Similar behavior was observed in the total amount of CO₂ observed, decreasing after an initial maximum. For the Rh-containing formulations, CO₂ exhibited the lowest variability in isotope product breakdown with nearly constant percent composition shown in part E of Figure 18 and Figure 19 as well as detailed in Table 12. Not surprisingly, the most abundant CO₂ isotope is ¹⁸O¹³C¹⁶O, in which the ¹³C-¹⁶O bond within ethanol-1-¹³C is maintained and combines with the ¹⁸O from H₂¹⁸O. However, the second most abundant species is ¹⁸O¹³C¹⁸O where the ¹³C-¹⁶O bond is broken and the ¹³C is bound to two ¹⁸O. This suggests that the second most likely process for CO₂ formation occurs via either the Boudouard reaction [Equation (8)] where two ¹³C¹⁸O

molecules react or the water gas shift reaction [Equation (9)] where a $^{13}\text{C}^{18}\text{O}$ intermediate is formed and reacts with water- ^{18}O .

7.5. Conclusions

From our analysis, it is clear that the primary reaction pathways are changing as a function of time on stream. Figure 21 attempts to highlight the most likely dominant pathways at various stages of ethanol reforming as adapted from Figure 2.

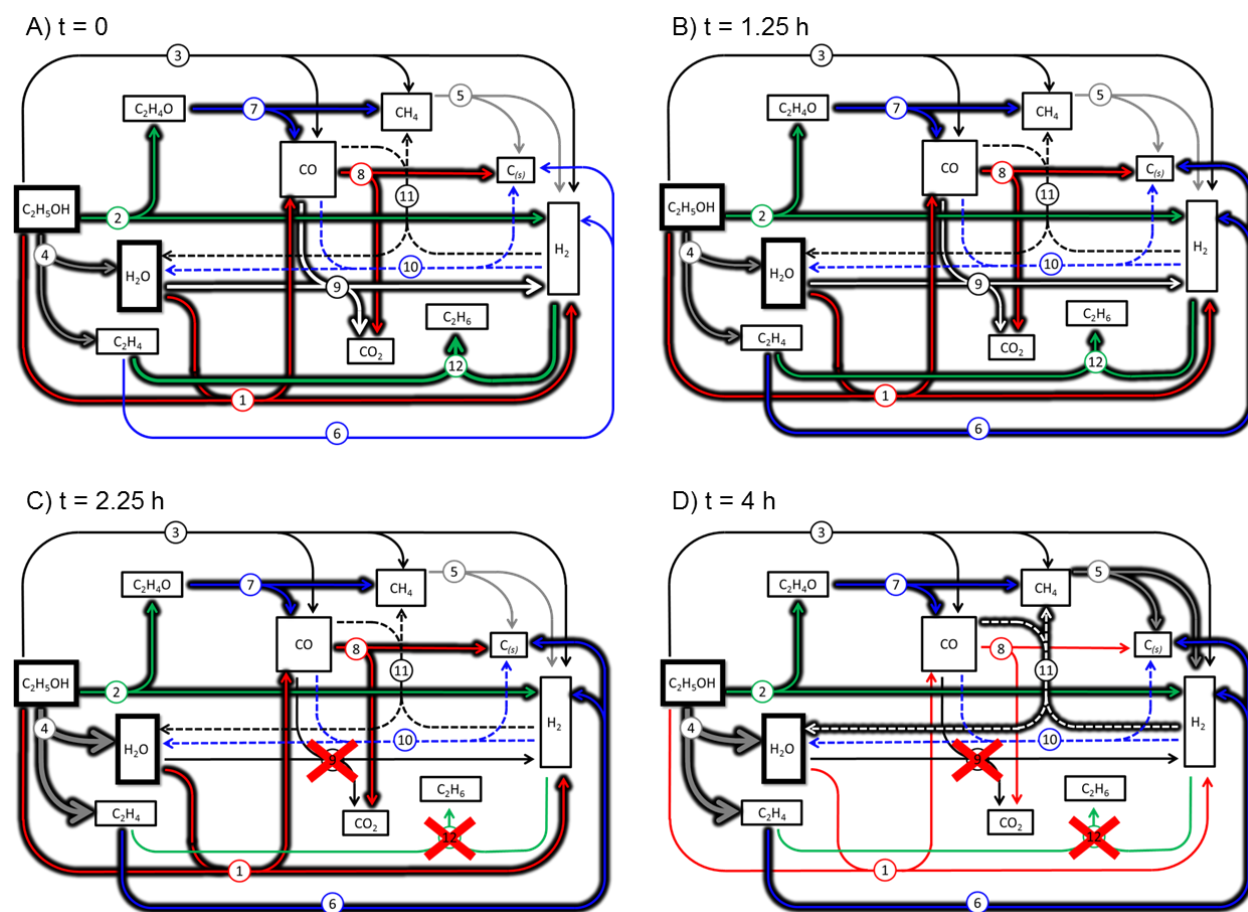


Figure 21: Schematic of possible dominant reaction pathways during ethanol steam reforming at (A) $t = 0$, (B) $t = 1.25$ h, (C) $t = 2.25$ h, and (D) $t = 4$ h. Black shading highlights dominant reaction pathways at each time. Red X indicates that the reaction most likely does not occur. Circled numbers correlate to numbered Equations (1-12). Arrows represent forward reaction for simplicity. [Crowley *et al.* 2016]

By examining the isotopic breakdown of the various compounds produced during ethanol steam reforming, we have been able to gain insight on the contribution of each metal, Rh and Pt, to the reforming process. The methodology presented here has enabled a more complete understanding of the reaction sequence for determining the underpinnings of catalyst performance.

By using carefully selected isotope-labeled reactants, individual reaction pathways have been examined with an unprecedented level of clarity and trackability, thereby allowing for the unification of theory and experimentally observed results. The selectivity toward ethanol dehydration increased as the catalyst deactivated. The presence of Pt within the catalyst makeup stabilizes Rh performance, allowing for 100% conversion of ethanol for a time period nearly threefold that of the single metal formulations. Rh has been shown to be more effective at breaking the C-C bond within ethanol and allowing for more diverse species recombination than Pt. It was shown that oxygen from the support plays a crucial role in the formation of reforming products, though Pt does not favor reaction between support oxygen and C-species on its surface.

The presence of all C- and O-isotopes within the products proves that bond preservation is not the only pathway for product formation. A recombination of species on the surface of the catalyst is occurring throughout the process for all catalyst formulations, indicating that a classic depiction of possible reactions [Equations (1-12)] is incapable of completely describing species formation. These

findings suggest that the catalyst material, including both the metal and support, has a profound impact on product formation.

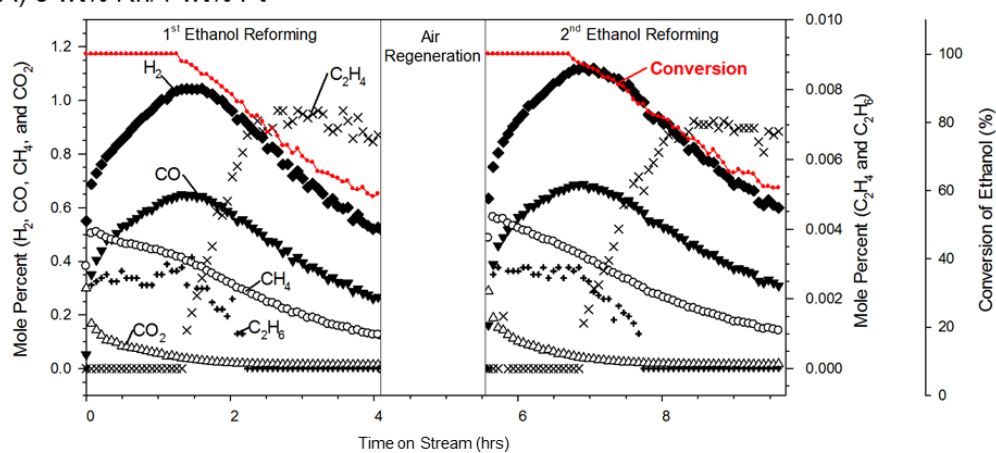
Chapter 8: Regeneration behavior

Catalyst deactivation is a problem that plagues the reforming of oxygenated hydrocarbons, limiting the amount of time the reforming process can be run continuously and necessitating regeneration procedures that are costly in terms of both time and materials. Here we investigate oxidative and reductive regeneration techniques and their impact on catalyst performance.

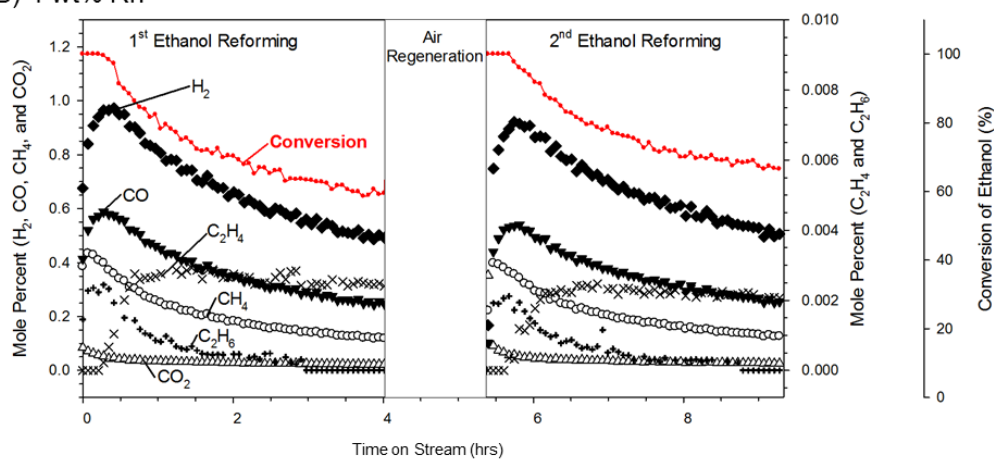
8.1. Oxidative regeneration

As part of the isotope-labeled reactant study, regeneration was performed in 5% O₂ in N₂ after 4 hours on stream. Oxidative regeneration has shown to be beneficial in removing coke buildup on the surface of the catalyst.⁵¹ The product distribution profiles for the bimetallic 3 wt% Rh/1 wt% Pt, single metal Rh and single metal Pt and catalyst formulations are shown in Figure 22.

A) 3 wt% Rh/1 wt% Pt



B) 4 wt% Rh



C) 4 wt% Pt

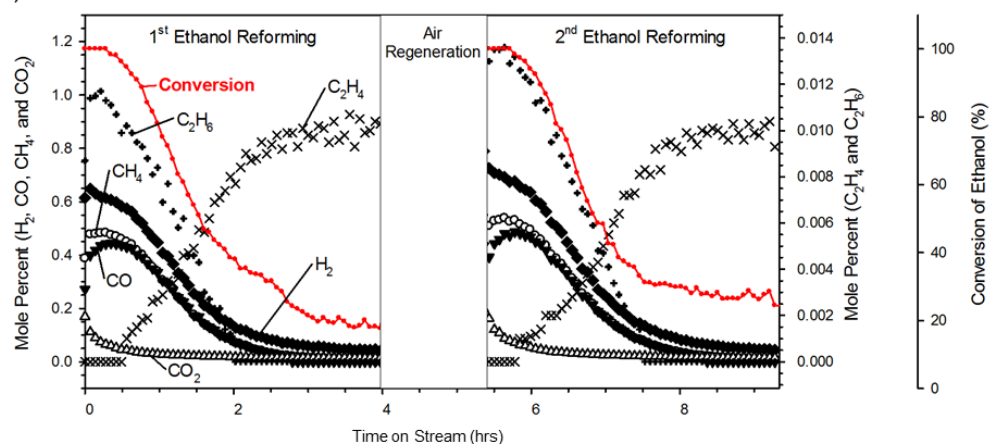


Figure 22: Product distribution profile for the reforming of ethanol-1-¹³C with water-¹⁸O with 1 hour regeneration in 5% O₂ in N₂ over (A) 3 wt% Rh/1 wt% Pt, (B) 4 wt% Rh, and (C) 4 wt% Pt on SiO₂-ZrO₂ support. Reaction conditions: S/C = 1.5, GHSV = 44,000 hr⁻¹, calcination temperature: 550°C, reforming temperature: 350°C, and 1 atm. [Crowley *et al.* 2016]

Across all catalyst formulations, the product distribution profile is nearly identical both pre- and post-regeneration, suggesting that the catalysts are fully able to be regenerated in an oxidative environment. However, the ability to fully regenerate the catalyst may be due to the relatively mild operating conditions and short time on stream before regeneration consistent with the work of Simson *et al.*⁵¹

8.2. Reductive regeneration

As part of the *operando* XAFS analysis study, regeneration was performed in 5% H₂ in He after 2.5 hours on stream. Reductive generation can remove carbon buildup on the surface while simultaneously stripping the metal nanoparticles of any oxide layer that may have formed during reaction. The product distribution profiles for the bimetallic 3 wt% Rh/1 wt% Pt, single metal Rh, and single metal Pt catalyst formulations are shown in Figure 23.

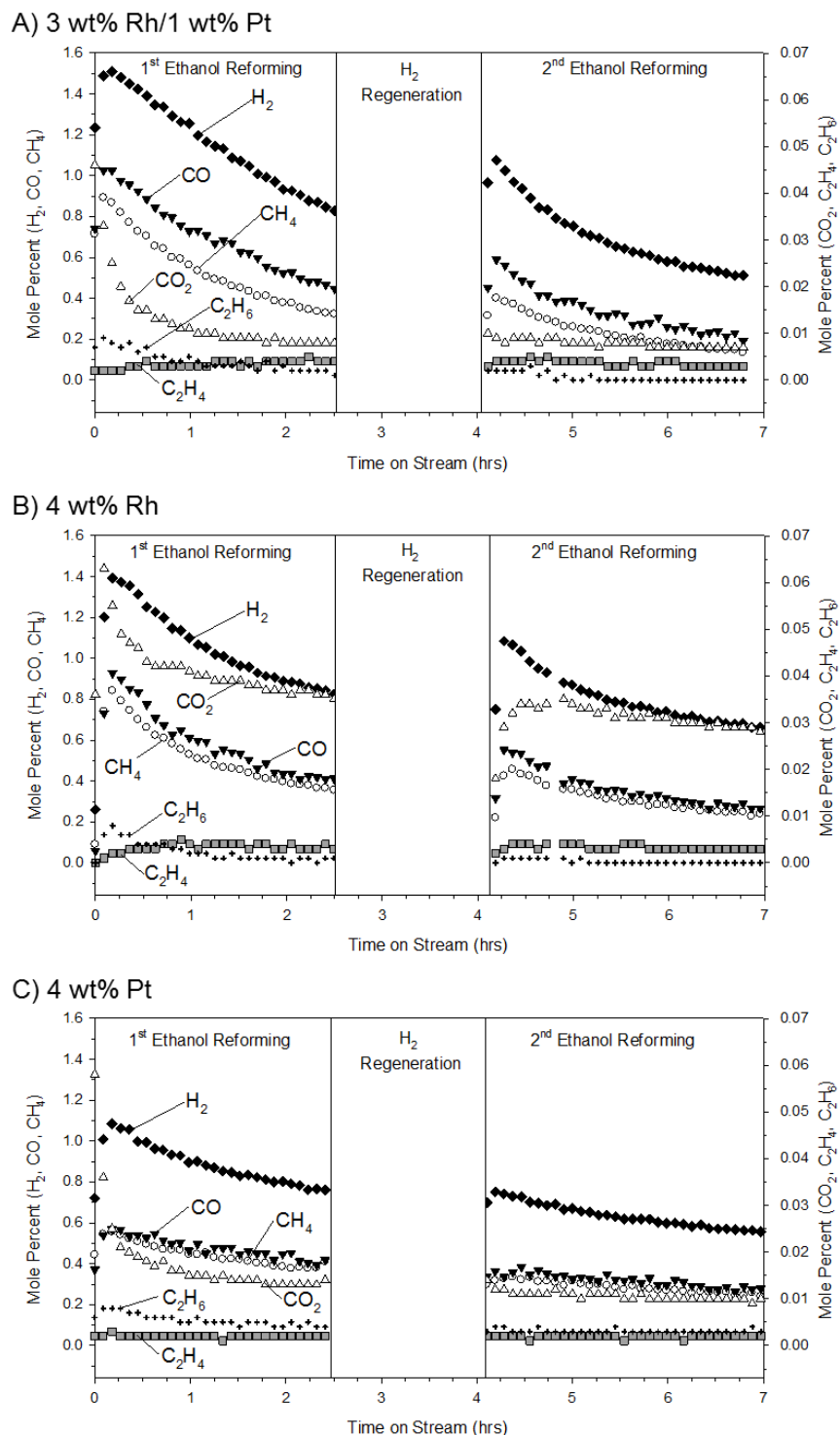


Figure 23: Product distribution profile for the steam reforming of ethanol with 1 hour regeneration in 5% H_2 in He over (A) 3 wt% Rh/1 wt% Pt, (B) 4 wt% Rh, and (C) 4 wt% Pt on SiO_2 - ZrO_2 support. Reaction conditions: Nashner-Adler reactor, S/C = 1.5, flow rate = 44 mL/min, calcination temperature: 550°C, reforming temperature: 350°C, and 1 atm.

It is clear that reductive regeneration does not achieve full regeneration across all catalyst formulations. The bimetallic and pure Rh formulations (Figure 23A and B) recover roughly 70% of their selectivity to hydrogen whereas the pure Pt formulation (Figure 23C) resumes ethanol reforming at identical selectivity toward all species. This suggests that hydrogen is incapable of cleaving the Pt-C bond in the absence of Rh and carbon species bound to Rh are only partially removed.

Chapter 9: Modeling and simulations

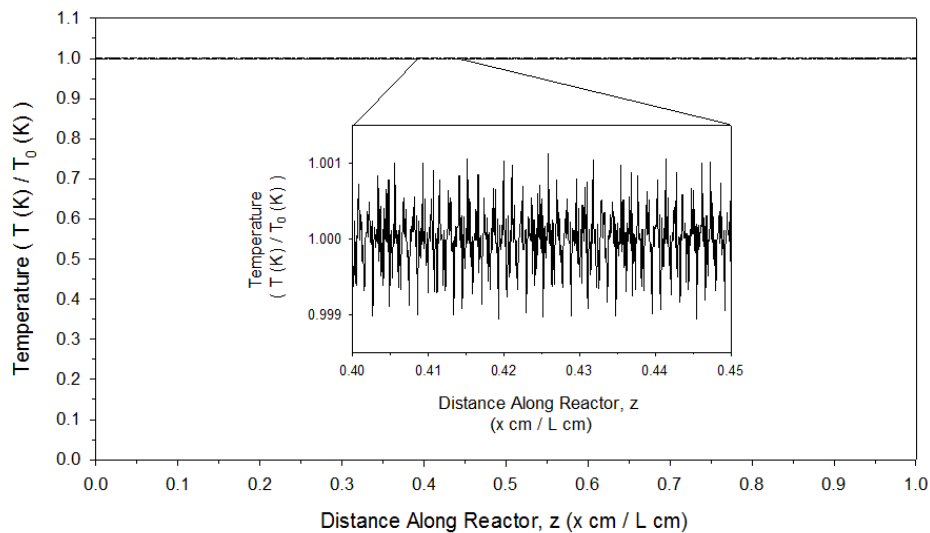
To better understand the ethanol reforming process, simulation work was performed to provide a means of validating the experimentally observed behavior against thermodynamic and kinetic theory. All experimental parameters for catalytic ethanol reforming in a packed bed reactor as previously described were simulated in the model. A full derivation of the governing equations is presented in Appendix D.

9.1. Temperature profile along the reactor bed

Reactor temperature was examined as a function of length along the reactor bed in the plug flow reactor setup to quantify the expected thermal profile during reaction, allowing for verification that localized endotherms and exotherms had no discernible impact on the temperature within the reactor. The simulation yielded consistent temperatures within the reactor at the two main reaction temperatures.

The temperature profile was shown to be constant along the reactor bed at both 350°C and 650°C as shown in Figure 24.

A) Reactor temperature = 350°C



B) Reactor temperature = 650°C

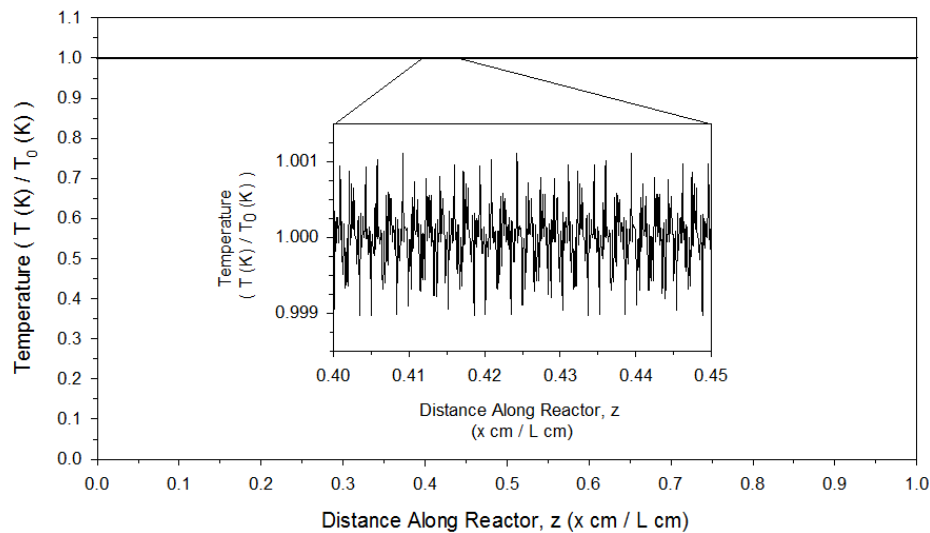


Figure 24: Nondimensionalized temperature profile along the reactor bed for catalytic ethanol steam reforming performed at (A) 350°C and (B) 650°C.

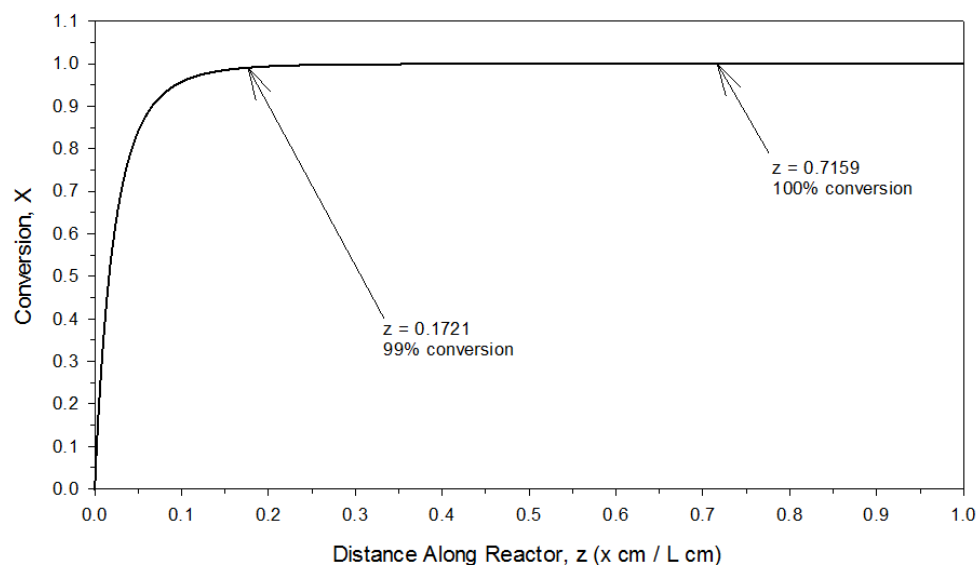
The observed behavior in Figure 24 is not surprising due to the dilute nature of the reactant mixture, primarily composed of nitrogen at roughly 96%, allowing for thermal stability independent of the ethanol steam reforming reaction.

Interestingly, upon closer inspection, the temperature seems to vary by roughly 0.1% at each temperature. From an experimental point of view, one explanation could be that this behavior is due to the localized endotherms/exotherms occurring as part of the real reaction system. However, due to the confines of the simulation, the reaction itself is entirely endothermic. Therefore, this observed fluctuation is due entirely to the noise of the ordinary differential equation solver employed. In this case, the “ode45” solver was used as part of the Matlab suite.¹¹⁶ This solver is based on the explicit Runge-Kutta method,¹¹⁷ an initial-value method allowing for the greatest level of accuracy with an iterative approach.

9.2. Conversion profile along the reactor bed

Complete conversion of ethanol is expected almost immediately after entering the catalyst bed at both 350°C and 650°C as shown in Figure 25.

A) Reactor temperature = 350°C



B) Reactor temperature = 650°C

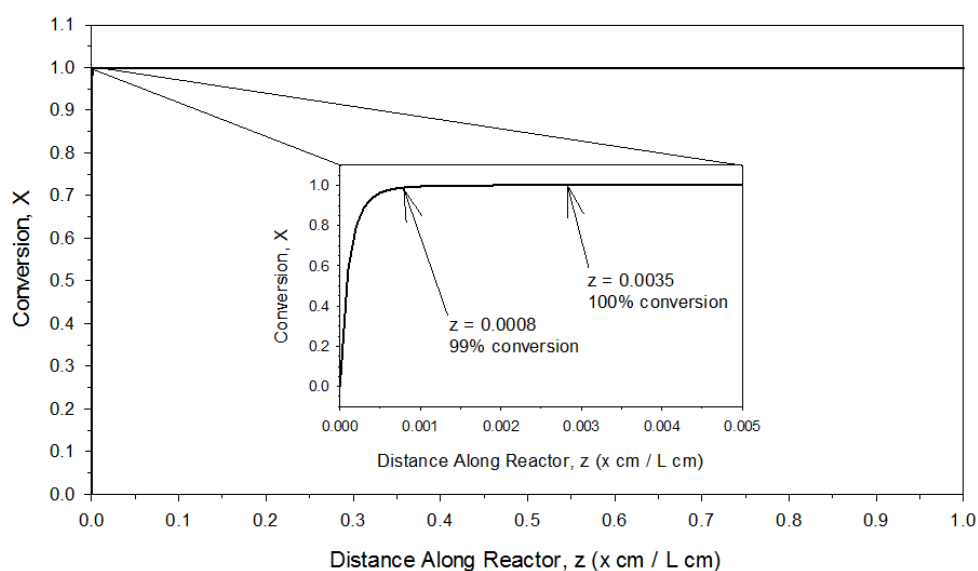


Figure 25: Nondimensionalized conversion profile along the reactor bed for catalytic ethanol steam reforming performed at (A) 350°C and (B) 650°C.

The 100% conversion observed experimentally at each temperature is consistent with thermodynamic and kinetic calculations. Furthermore, a test was performed to validate the developed model at less than 100% conversion of ethanol.

During one reforming test performed at 350°C, the catalyst bed shifted outside of the reactor region heated by the furnace, resulting in a lower reforming temperature and initial conversion of only 82.25%. The model predicts that this level of conversion should be observed at a reactor temperature of roughly 250°C as shown in Figure 26.

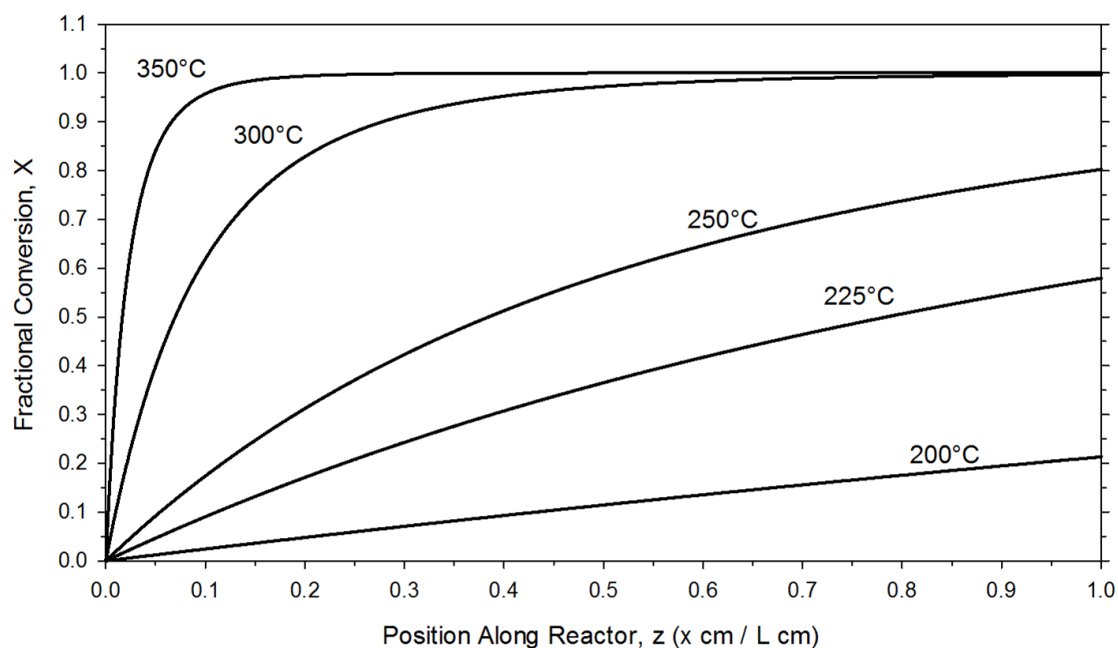


Figure 26: Fractional conversion as a function of position along the packed bed reactor for ethanol steam reforming performed at various temperatures.

The 250°C reforming temperature intuitively makes sense given the close proximity to the heated region of the furnace and the residual heat of the reactant stream. An attempt was made to correlate the measured concentration of the gaseous products at this temperature to those predicted by a Gibbs free energy equilibrium calculation. Unfortunately, this correlation cannot be made since the equilibrium calculation solely revolves around the gas-phase reactants and products, failing to take into account carbon deposition on the surface of the catalyst.

Chapter 10: Conclusions and future work

10.1. Conclusions

This work was meant to identify and characterize a possible catalyst formulation allowing for the use of oxygenated hydrocarbons commonly found in biomass to produce syngas through the steam reforming process and to determine the factors dictating overall behavior. Ethanol was used as a model compound due to its relative simplicity while maintaining the key attributes of at least one C-C bond and an oxygen-containing functional group.

The first investigation involved determination of a catalyst formulation capable of providing near-equilibrium hydrogen production. Rh-containing catalyst formulations exhibited higher dispersion of metal on the surface of the support. Precious metal sintering was minimized by calcining the catalyst material at the operating temperature. The catalyst exhibiting the desired performance was the 3 wt% Rh/1 wt% Pt on SiO₂-ZrO₂ support, achieving near-equilibrium hydrogen production for approximately 90 hours on stream at industrially relevant operating conditions including temperature, S/C ratio, and space velocity.

The contribution of each metal to overall catalyst performance was determined with respect to oxidation state and conformation of the precious metal nanoparticles. The oxidation state of Rh was found to change dynamically as a function of time on stream. *Operando* X-ray absorption spectroscopy showed that a partially oxidized Rh surface was the most active in ethanol reforming capability.

The presence of Pt, however, was found to stabilize the Rh and allow for prolonged operation at desired hydrogen yields. XAFS analysis showed that the coordination number between Rh and Pt atoms were dynamic during ethanol reforming as well with the coordination number of Rh-Pt changing drastically between *ex-situ*, *in-situ*, and *operando* conditions. This suggests that an accurate measurement of catalyst configuration can only be performed during reaction.

A final investigation involved determining the contribution of each metal to the overall reforming behavior during low-temperature ethanol steam reforming. Isotope-labeled reactant studies illuminated the role of single-metal Rh, single-metal Pt, and the most active of the bimetallic formulations in the reforming process. All combinations of isotope- and non-isotope-labeled atoms were detected in the products for the bimetallic formulation, proving there are multiple pathways involved in H₂, CO, CO₂, CH₄, C₂H₄, and C₂H₆ product formation. Pt was almost completely incapable of breaking the C-C bond within ethanol, suggesting that Pt-based formulations will not enable the efficient processing of biomass-derived feedstocks. Both the recombination of C-species on the surface of the catalyst and preservation of the C-C bond within ethanol are responsible for C₂ product formation for all catalyst formulations. The role of oxygen from the support was found to be an important factor in product distribution with clear evidence presented that oxygen from the SiO₂-ZrO₂ support constitutes 10% of the oxygen in CO formed during reaction.

10.2. Future work

The work presented in this thesis has demonstrated the influence of catalyst morphology on the selectivity and regeneration behavior of precious metal catalysts while expounding specific reaction pathways during ethanol reforming.

Determination of activation and deactivation modes and optimization of design parameters during catalyst synthesis are important areas future development.

Specifically, the phases of precious metal nanoparticles with regard to lattice structure should be examined and correlated to catalyst activity. Reaction pathways at temperatures allowing for peak thermodynamic efficiencies between 600°C and 700°C require further investigation. Furthermore, deactivation through coke formation has been shown throughout this work, highlighting a vital area for future work: whether a selectivity change of the catalyst gives rise to coke formation and subsequently the detection of intermediate species or if coke formation causes a shift in catalytic activity resulting in intermediate speciation.

10.2.1. Nanoparticle lattice structure

Chapter 6 showed that the coordination number between atoms in the supported precious metal nanoparticles of the catalyst changed dynamically during reaction. The bimetallic catalyst formulation was shown to be a true alloy after the pre-reduction step, but segregation of the metals was occurring during reaction indicated by the ratio of Rh coordination numbers at the reaction temperature of 350°C (see Table 6). Interestingly, the form of the precious metal nanoparticles as

either alloy or segregated was indecipherable when the catalyst was cooled to room temperature.

In section 4.2, TEM images exposed that the precious metal nanoparticles exhibit a specific lattice structure. Both Rh and Pt exhibit face-centered cubic crystal structures as single metals, but the packing of atoms in bimetallic nanoparticles remains unclear. A more in depth analysis on the crystal structure, coordination number, and corresponding activity of precious metal nanoparticles should elicit the most active phase. Studies could then be performed on synthesis parameters that preferentially give rise to this active phase with characterizations by high-resolution transmission electron microscopy (HRTEM), x-ray photoelectron spectroscopy (XPS) and *in situ* scanning tunneling microscopy (STM).¹¹⁸

10.2.2. Reaction network at elevated temperatures

The evolution of preferred reaction pathways was determined for the steam reforming of ethanol at 350°C through the use of isotope-labeled reactants in Chapter 7. It was shown that the water-gas shift reaction [Equation (9)] and ethylene hydrogenation [Equation (12)] were suppressed as a function of time on stream at this temperature. Oxygen exchange with the support was theorized to allow for the formation of CO_y species at the interface with 10% of all CO formed containing oxygen from the support. By performing a similar study at temperatures allowing for peak thermodynamic efficiencies (600°C to 700°C), information could be gained on whether product species formation occurs primarily via bond preservation or species recombination at industrially relevant conditions.

10.2.3. Carbon deposition

In Chapter 8, the regeneration behavior of several precious metal catalyst formulations was examined to determine the role of individual metals in a bimetallic catalyst. Reductive regeneration was shown to be only partially effective on Rh-containing catalysts and completely inactive in the regeneration of a single-metal Pt formulation. However, regenerations performed in an oxidative environment allowed for identical performance to that of fresh catalyst, suggesting that the observed catalyst deactivation was completely reversible.

During oxidative regeneration, the only observed species in the effluent was CO₂, indicating that carbon deposition on the surface of the catalyst was largely responsible for deactivation. A full characterization of this carbon could provide information on the carbon species most likely to deposit on the surface (either the O-bound carbon or the methyl group carbon within ethanol) as well as the type of coke formed on the surface (amorphous versus graphitic). Temperature programmed oxidation (TPO) studies with simultaneous analysis by GC-MS on catalysts exposed to isotope-labeled reactants would be capable of providing this information.

In terms of species formation, it remains unclear as to what comes first: selectivity change resulting in coke formation or coke formation resulting in selectivity change, both leading to catalyst deactivation. Certain surface groups including carbonyls, hydroxyls, esters, and ketones have been shown to greatly influence the activity of catalysts.^{119,120} Solid-state nuclear magnetic resonance

(SSNMR) could be employed with respect to ^{13}C as a powerful technique that would not only characterize the type of coke deposited, but the functional groups present on the carbon surface. Understanding the inception of coke formation versus changes in selectivity will provide invaluable information on the reaction pathways of fuel reforming, allowing for the targeted design and implementation of supported metal catalysts.

Appendices

Appendix A: Gaseous product analysis

A.1. Micro gas chromatography (μGC)

The detection and quantification of gaseous products was performed with a 3-channel Inficon 3000 Micro GC. A full description of the instrument, including columns and target compounds, is provided in Table A.1.

Table A.1: Inficon 3000 Micro GC channel specifications and applications.

Channel	A	B	C
Column Type	Molecular Sieve	Plot U	OV-1
Column Applications ¹²¹	Permanent and noble gases. Argon and oxygen separation at 35°C	C1 to C7 hydrocarbons, CO ₂ , methane, air/CO, water, oxygenates, amines, solvents, alcohols, ketones, aldehydes	Amines, hydrocarbons, pesticides, PCBs, phenols, sulfur compounds, flavors, and fragrances
Common Compounds ¹²²	H ₂ , O ₂ , N ₂ , CH ₄ , CO	CO ₂ , Ethylene, Ethane, Acetylene, 1,2-Propadiene, Methyl Acetylene	Water, Methanol, Ethanol, n-Butane, n-Hexane, n-Heptane
Column Temperature	90°C	75°C	60°C
Column Pressure	23 psi	23 psi	23 psi
Carrier Gas	Argon	Helium	Helium

A.2. Gas chromatography – mass spectroscopy (GC-MS)

The detection and quantification of isotope-labeled gaseous products was performed with an Agilent 7890B Gas Chromatograph equipped with a 5977A mass selective detector (MSD). A full description of the method parameters is provided in Table A.2.

Table A.2: Method parameters for gaseous product analysis by GC-MS.

Column	Supelco Carboxen-1010 PLOT 30 m x 320 μm ID x 15 μm film thickness
Column Mode	Constant Flow
Carrier Gas	Helium (Research Grade, 6.0)
Carrier Gas Flow Rate	3 mL/min
Inlet Temperature	125°C
Inlet Mode	Split
Split Ratio	10:1
Initial Temperature/Initial Time	35°C/1 min
Heating Rate	100°C/min
Final Temperature/Final Time	240°C/3.5 min
Total Run Time	6.55 min
Detector Temperature (quad/source)	180°C/230°C
Injection Volume (valve)	1.000 mL

Appendix B: XAFS

B.1. Nashner-Adler cell

The Nashner-Adler reactor cell used for *operando* X-ray analysis is shown in Figure A.1.

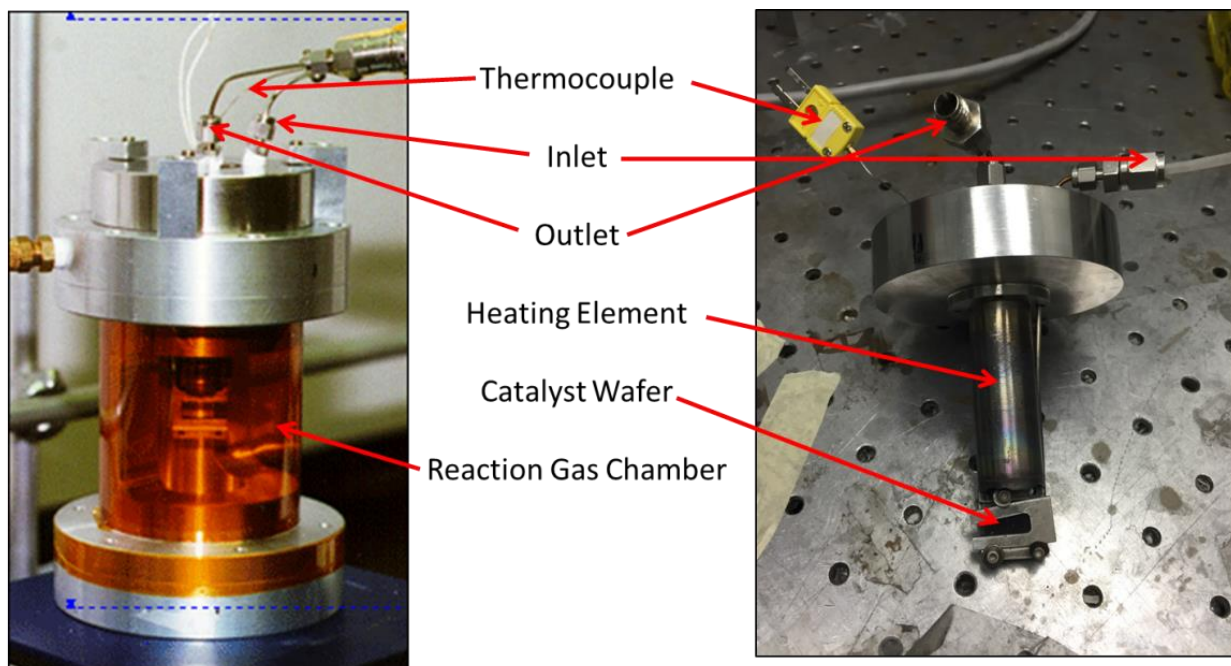


Figure A.1: Nashner-Adler cell used for X-ray characterization of the catalyst during ethanol steam reforming.

In this reactor cell, the pelletized form of the catalyst (catalyst wafer) is suspended in a larger volume (roughly 250 mL) of the reactant mixture. Catalyst bed temperature is controlled through the heating element and monitored by the thermocouple. The reactant mixture is introduced through the inlet and products are analyzed at the outlet.

B.2. XAFS fitting

R-space fitting was performed to determine N , R , and σ^2 (see section 6.4). This was done by comparing the measured spectra in R-space to calculated scattering factors for Rh-Rh, Rh-Pt, and Pt-Pt and adjusting the contribution of these paths to the observed spectra.⁹⁸ A summary of the XAFS fitting results for the 3 wt% Rh/1 wt% Pt catalyst during several stages of ethanol reforming is shown in

Figure A.2. Good agreement between the fit spectra and the experimental spectra support the claims in section 6.4.

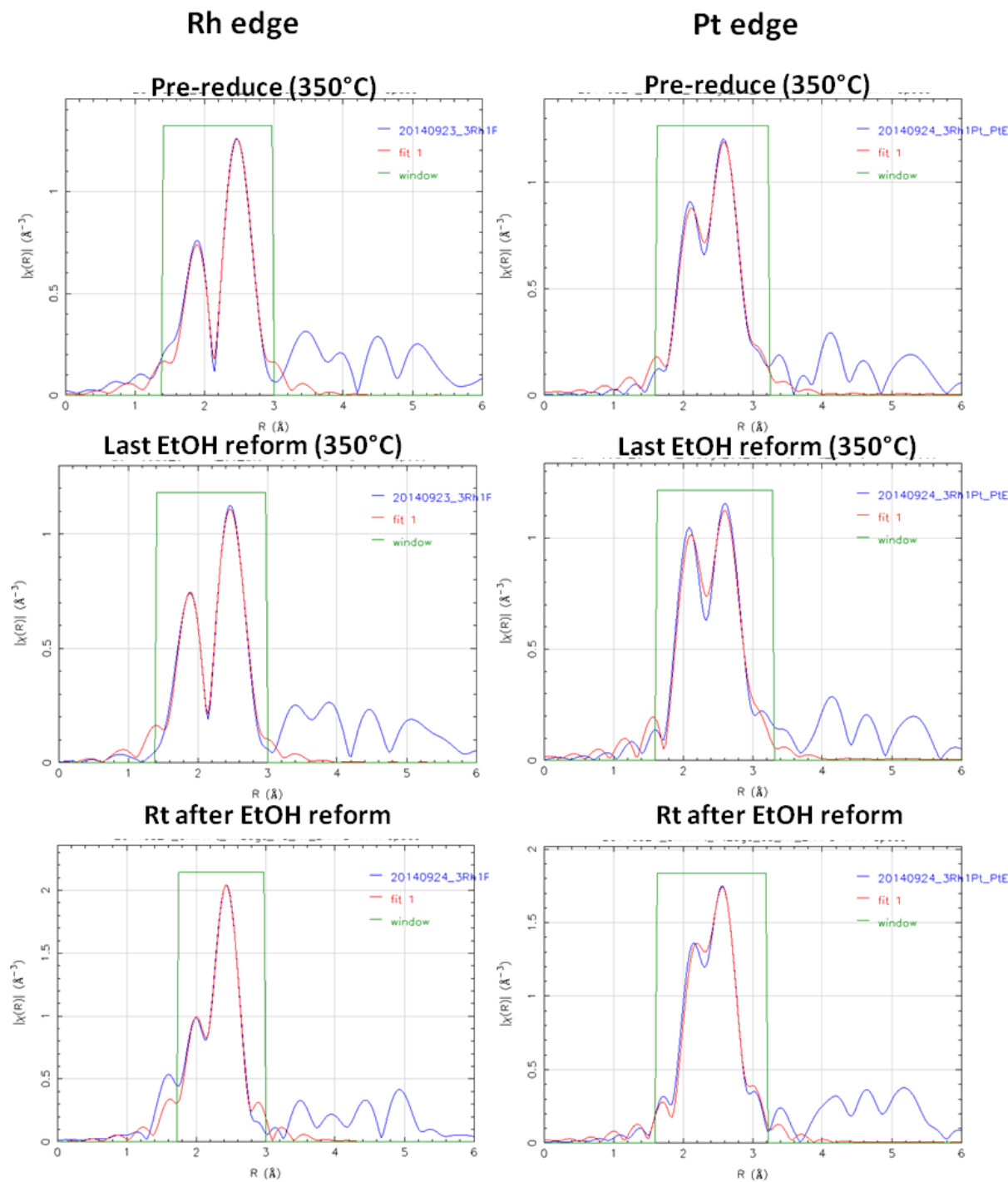


Figure A.2: XAFS fitting of the Rh-edge and Pt-edge spectra for the 3 wt% Rh/1 wt% Pt catalyst during several stages of ethanol reforming.

Appendix C: Isotopic enrichment confirmation

Compound identity and isotope labeling was confirmed through GC-MS analysis. Both isotope-labeled and non-isotope-labeled liquid samples of ethanol and water were directly injected onto the analytical column. Non-isotope-labeled ethanol and water were identified by comparing their mass spectra to the NIST database with each having agreement to the reference spectra greater than 95%. The retention time of the unlabeled ethanol and water were used to confirm the identity of the isotope-labeled chemicals. For both ethanol and water, labeled and unlabeled chemicals exhibited nearly identical retention times, thus confirming their identity as shown in Figure A.3.

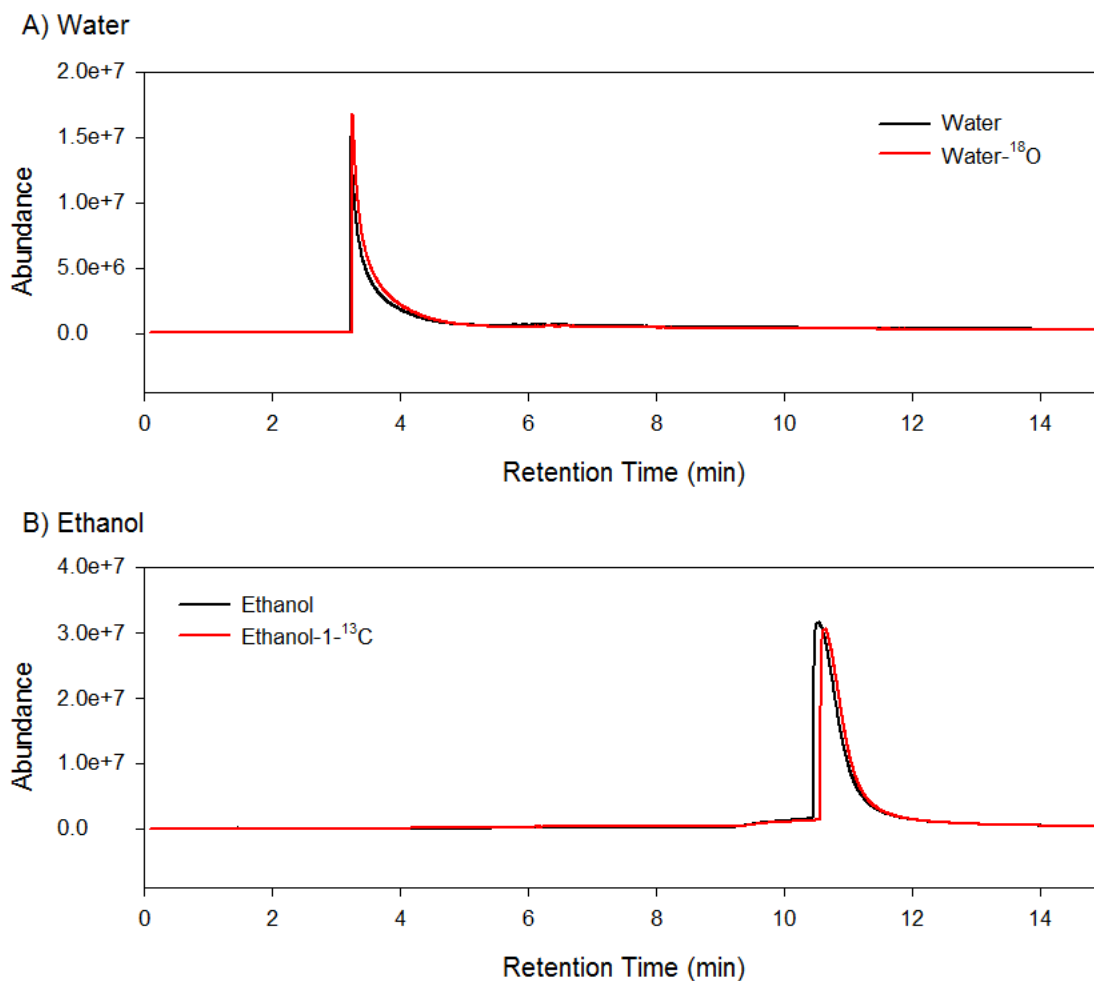


Figure A.3: Total ion chromatograms for (A) water and water-¹⁸O and (B) ethanol and ethanol-1-¹³C.

Isotope labeling of ethanol and water was confirmed by examining the mass spectra of both labeled and unlabeled chemical species as shown in Figure A.4 and Figure A.5. In each case, the fragmentation patterns confirm the presence of ¹⁸O in water and ¹³C in ethanol.

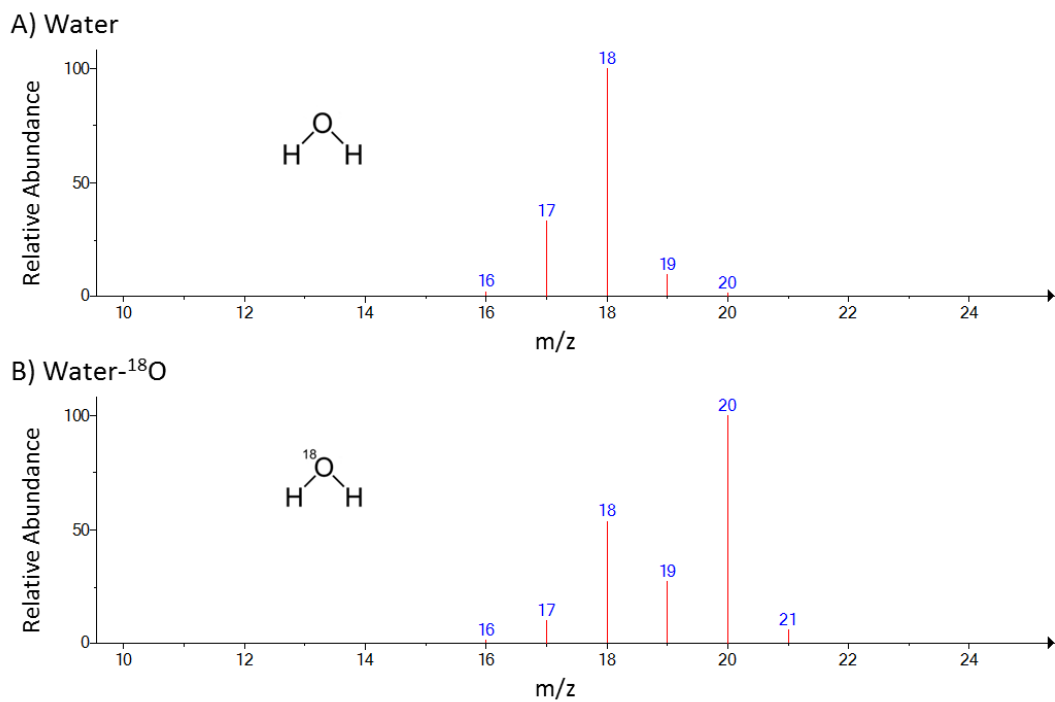


Figure A.4: Mass spectral fragmentation pattern of (A) water and (B) water-¹⁸O.

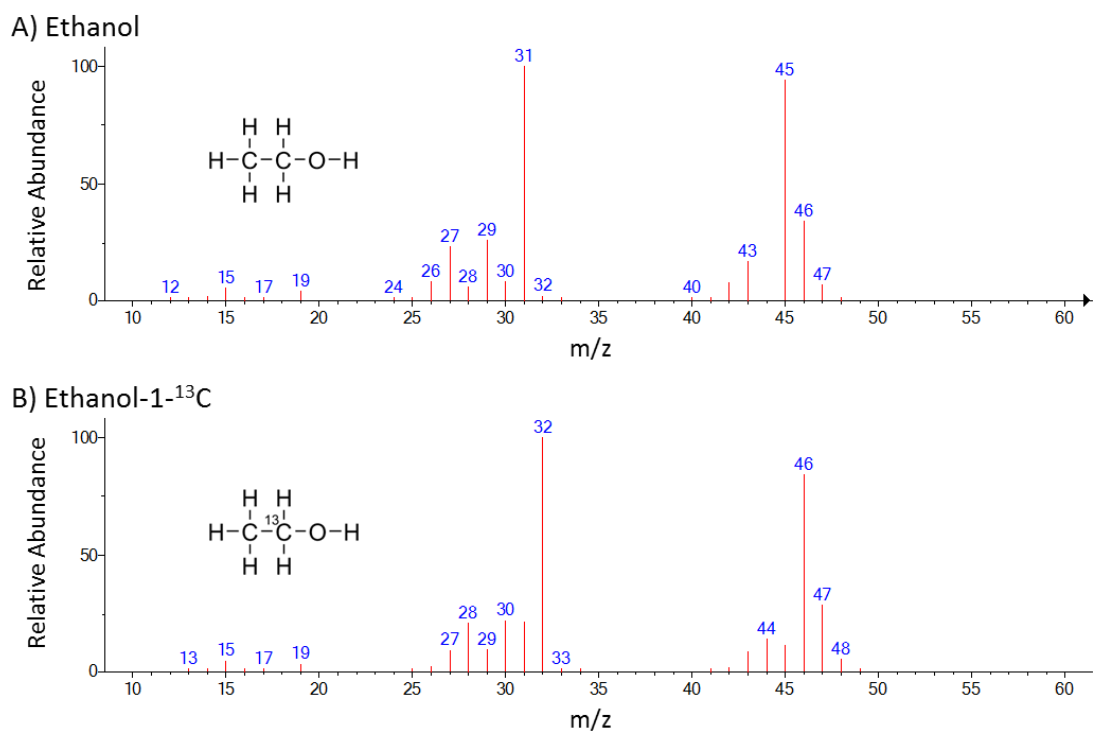


Figure A.5: Mass spectral fragmentation pattern of (A) ethanol and (B) ethanol-1-¹³C.

Appendix D: Additional calculations and simulation – plug flow reactor

D.1. Rate expression

A rate expression was developed in order to simulate reaction conditions for the plug flow reactor.

Assume: Arrhenius rate constant k as defined in Equation (A.1).

$$k = k_0 \cdot e^{-\frac{E_a}{RT}} \quad (\text{A.1})$$

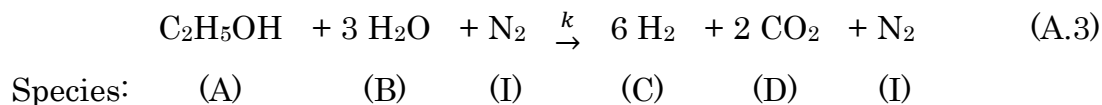
Where k_0 is the pre-exponential factor, E_a is the activation energy, R is the universal gas constant, and T is the temperature in Kelvin. Kinetic parameters, including values for k_0 , E_a , and reaction order were taken from the doctoral thesis of Dr. Amanda Simson.¹²³

$$k_0 = 2.21 \times 10^{-5} \text{ mol}^{-0.2} \text{ m}^{0.6} \text{ s}^{-1}$$

$$E_a = 85.24 \text{ kJ} \cdot \text{mol}^{-1} = 85240 \text{ J} \cdot \text{mol}^{-1}$$

$$r_{EtOH} = r_A = k[P_{EtOH}]^{1.2} \quad (\text{A.2})$$

Reaction with N_2 balance:



Species balance:

Let F_i denote the flow rate of species i where subscript “0” indicates initial value.

Let F_T denote the total flow rate where subscript “0” indicates initial value.

Let T denote reactor bed temperature where subscript “0” indicates initial value.

Let t denote the nondimensionalized reactor bed temperature where

$$t = \frac{T}{T_0} \quad (\text{A.4})$$

Let X denote conversion of ethanol as defined in Equation (A.5).

$$X = \frac{n_{\text{EtOH},in} - n_{\text{EtOH},out}}{n_{\text{EtOH},in}} \quad (\text{A.5})$$

Table A.3: Species balance during ethanol steam reforming based on stoichiometry in Equation (A.3).

Species	In	Out
A	F_{A0}	$F_{A0}(1 - X)$
B	F_{B0}	$F_{B0}\left(1 - 3\frac{F_{A0}}{F_{B0}}X\right)$
C	0	$6F_{A0}X$
D	0	$2F_{A0}X$
I	F_{I0}	F_{I0}

Assume:

$$F_{A0} = y_A F_{T0} \quad (\text{A.6})$$

where y_A is the mole fraction of ethanol.

Therefore:

$$F_{T0} = F_{A0} + F_{B0} + F_{I0} \quad (\text{A.7})$$

and

$$F_T = F_{A0}(1 - X) + F_{B0}\left(1 - 3\frac{F_{A0}}{F_{B0}}X\right) + 8F_{A0}X + F_{I0} \quad (\text{A.8})$$

$$F_T = F_{A0} - F_{A0}X + F_{B0} - 3F_{A0}X + 8F_{A0}X + F_{I0} \quad (\text{A.9})$$

$$F_T = F_{A0} + F_{B0} + F_{I0} + 4F_{A0}X \quad (\text{A.10})$$

$$F_T = F_{T0} + 4y_A F_{T0} X \quad (\text{A.11})$$

$$F_T = F_{T0}(1 + 4y_A X) \quad (\text{A.12})$$

$$P_A = y_A P_T = \frac{F_{A0}}{F_T} (1 - X) P_{T0} = \frac{y_A P_{T0} F_{T0} (1 - X)}{F_{T0} (1 + 4y_A X)} = \frac{P_{A0} (1 - X)}{(1 + 4y_A X)} \quad (\text{A.13})$$

Therefore,

$$r_A = \left[(2.21 \times 10^5) e^{\frac{-85240 \text{ J}\cdot\text{mol}^{-1}}{(8.314 \text{ J}\cdot\text{mol}^{-1}\text{K}^{-1})(T)}} \right] \left[P_{A0} \frac{(1 - X)}{(1 + 4y_A X)} \right]^{1.2} \quad (\text{A.14})$$

Ultimately giving

$$r_A = \left[(2.21 \times 10^5) e^{\frac{-10252.586 \text{ K}}{(T_0 t)}} \right] \left[P_{A0} \frac{(1 - X)}{(1 + 4y_A X)} \right]^{1.2} \quad (\text{A.15})$$

D.2. Mass balance

Assuming a pseudo steady-state reactor, a mass balance for the system can be developed from the simple equation:

$$IN - OUT = \frac{dN_A}{dt} = 0 \quad (\text{A.16})$$

where N_A is the amount of ethanol and t is time.

$$F_{A0}|_W - (F_{A0}|_{W+\Delta W} + r_A \Delta W) = 0 \quad (\text{A.17})$$

$$F_{A0}|_W - F_{A0}|_{W+\Delta W} - r_A \Delta W = 0 \quad (\text{A.18})$$

$$-r_A \Delta W = F_{A0}|_{W+\Delta W} - F_{A0}|_W \quad (\text{A.19})$$

Therefore, for the packed bed reactor, the reaction rate is governed by Equation (A.20).

$$-r_A = \lim_{\Delta W \rightarrow 0} \left(\frac{F_{A0}|_{W+\Delta W} - F_{A0}|_W}{\Delta W} \right) = \frac{dF_A}{dW} \quad (\text{A.20})$$

where W is the mass of the catalyst.

$$F_A = F_{A0}(1 - X) \quad (\text{A.21})$$

which implies

$$dF_A = -F_{A0}dX \quad (\text{A.22})$$

A cylindrical catalyst bed approximation was used in order to directly correlate the catalyst particle bed to reactor length (L)

$$W = \rho_c \cdot V = \rho_c \cdot \pi \left(\frac{D}{2} \right)^2 \cdot x = \rho_c \cdot \pi \frac{D^2}{4} \cdot x \quad (\text{A.23})$$

So,

$$dW = \rho_c \cdot \pi \frac{D^2}{4} \cdot dx \quad (\text{A.24})$$

where x is position along the reactor tube. Here, we will nondimensionalize position:

Let:

$$z = \frac{x}{L} \quad (\text{A.25})$$

which implies

$$dx = Ldz \quad (\text{A.26})$$

Therefore,

$$-r_A = \frac{-F_{A0}dX}{\rho_c \cdot \pi \frac{D^2}{4} \cdot Ldz} \quad (\text{A.27})$$

This implies

$$\frac{dX}{dz} = \frac{r_A}{F_{A0}} \rho_c \cdot \pi \frac{D^2}{4} \cdot L \quad (\text{A.28})$$

$$F_{A0} = \frac{\dot{V}P}{RT} \quad (\text{A.29})$$

$$F_{A0} = \frac{(44 \text{ mL} \cdot \text{min}^{-1})P}{RT} \left(\frac{1 \text{ L}}{1000 \text{ mL}} \right) \left(\frac{1 \text{ min}}{60 \text{ s}} \right) (\text{mole\% EtOH}) \quad (\text{A.30})$$

Therefore, $F_{A0} = 2.7 \times 10^{-7} \text{ mol} \cdot \text{s}^{-1}$.

$$\frac{dX}{dz} = \frac{r_A \rho_c \cdot \pi D^2 L}{(2.7 \times 10^{-7} \text{ mol} \cdot \text{s}^{-1})(4)} \quad (\text{A.31})$$

Ultimately giving:

$$\frac{dX}{dz} = \frac{\rho_c \cdot \pi D^2 L}{(2.7 \times 10^{-7} \text{ mol} \cdot \text{s}^{-1})(4)} \left[(2.21 \times 10^5) e^{\frac{-10252.586 \text{ K}}{(T_0 t)}} \right] \left[P_{A0} \frac{(1-X)}{(1+4y_A X)} \right]^{1.2} \quad (\text{A.32})$$

D.3. Energy balance

Assuming a pseudo steady-state reactor, an energy balance for the system can be developed from the simple equation:

$$E_{in} - E_{out} + \text{Heat}_{rxn} = \frac{dE}{dt} = 0 \quad (\text{A.33})$$

$$\Delta \dot{Q} + \dot{m} \hat{H} \Big|_W - \dot{m} \hat{H} \Big|_{W+\Delta W} - r_A \Delta W \Delta H_r(T) = 0 \quad (\text{A.34})$$

$$U\Delta A(T_a - T) - \dot{m}(\hat{H}|_{W+\Delta W} - \hat{H}|_W) - r_A\Delta W\Delta H_r(T) = 0 \quad (\text{A.35})$$

Where U is the overall heat transfer coefficient, A is the heat-exchange area per volume of reactor, T_a is the temperature at the reactor wall, and \dot{m} is the mass flow rate.

$$\Delta A = \frac{A}{V}\Delta V = \frac{\pi DL}{\left(\frac{\pi D^2 L}{4}\right)}\Delta V = \frac{4}{D}\Delta V = \frac{4}{D\rho_c}\Delta W \quad (\text{A.36})$$

$$\frac{4U}{D\rho_c}\Delta W(T_a - T) - \dot{m}(\hat{H}|_{W+\Delta W} - \hat{H}|_W) - r_A\Delta W\Delta H_r(T) = 0 \quad (\text{A.37})$$

$$\frac{4U}{D\rho_c}(T_a - T) - \dot{m}\frac{(\hat{H}|_{W+\Delta W} - \hat{H}|_W)}{\Delta W} - r_A\Delta H_r(T) = 0 \quad (\text{A.38})$$

Taking the limit as $\Delta W \rightarrow 0$ gives

$$\frac{4U}{D\rho_c}(T_a - T) - \dot{m}\frac{d\hat{H}}{dW} - r_A\Delta H_r(T) = 0 \quad (\text{A.39})$$

$$\frac{d\hat{H}}{dT} = \hat{C}_p \text{ implies } d\hat{H} = \hat{C}_p dT \quad (\text{A.40})$$

Therefore,

$$\frac{4U}{D\rho_c}(T_a - T) - \dot{m}\hat{C}_p\frac{dT}{dW} - r_A\Delta H_r(T) = 0 \quad (\text{A.41})$$

$$\frac{dT}{dW} = \frac{\frac{4U}{D\rho_c}(T_a - T) - r_A\Delta H_r(T)}{\dot{m}\hat{C}_p} \quad (\text{A.42})$$

After nondimensionalization using definitions from sections A.D.1. and A.D.2.

Equation (A.42) becomes:

$$\frac{dt}{dz} = \frac{\pi DLU(t_a - t)}{\dot{m}\hat{C}_p m_w} - \frac{\rho_c \pi \cdot D^2 \cdot L \cdot r_A \Delta H_r(T)}{4T_i \dot{m}\hat{C}_p m_w} \quad (\text{A.43})$$

U was calculated according to Equation (A.44) from Bagajewicz *et al.*¹²⁴

$$\frac{1}{U} = \frac{1}{h_o} + R_{od} + \frac{d_o \cdot \ln\left(\frac{d_o}{d_i}\right)}{2k_w} + \frac{d_o}{d_i} \frac{1}{h_i} + \frac{d_o}{d_i} R_{id} \quad (\text{A.44})$$

Where h_o is the outside film heat transfer coefficient, h_i is the inside film heat transfer coefficient, d_o is the outside reactor tube diameter, d_i is the inside reactor tube diameter, k_w is the wall thermal conductivity, R_{od} is the outside fouling heat transfer coefficient, and R_{id} is the inside fouling heat transfer coefficient. Values for air were used as a first approximation as shown in

Table A.4: Parameters for calculation of overall heat transfer coefficient in the packed bed catalytic reactor. [The Engineering ToolBox 2016]

Variable	Value	Units	Reference
h_o	10.45	W m ⁻² K ⁻¹	125
h_i	12.81	W m ⁻² K ⁻¹	125
d_o	6 x 10 ⁻³	m	N/A
d_i	4 x 10 ⁻³	m	N/A
k_w	3	W m ⁻¹ K ⁻¹	126
R_{od}	4 x 10 ⁻⁴	m ² K W ⁻¹	127
R_{id}	9 x 10 ⁻⁵	m ² K W ⁻¹	127

For simplicity, a constant value of 4.68 W m⁻² K⁻¹ was used for all simulations.

The change in enthalpy for the ethanol steam reforming reaction as a function of changing temperature can be determined by using Kirchhoff's Law¹²⁸ as shown in Equation (A.45).

$$\Delta H_r(T) = \Delta H_r(25^\circ\text{C}) + \int_{25^\circ\text{C}}^T \Delta C_p(T') dT' \quad (\text{A.45})$$

Functions for the heat capacities as a function of temperature for each reaction species were generated through sixth-order polynomial fits using data provided by the National Institute of Standards and Technology¹²⁹ and The Engineering ToolBox.^{130–132} Resulting equations were of the form:

$$C_p(T) = a \cdot T^6 + b \cdot T^5 + c \cdot T^4 + d \cdot T^3 + e \cdot T^2 + f \cdot T + g \quad (\text{A.46})$$

where T is in Celsius. Table A.5 shows the coefficients as outlined in Equation (A.46).

Table A.5: Sixth-order polynomial fit coefficients describing the change in heat capacity as a function of temperature for each reaction component as described in Equation (A.46).

Component:	C ₂ H ₅ OH	H ₂ O	H ₂	CO ₂
<i>a</i>	6.1008 x 10 ⁻¹⁸	7.1883 x 10 ⁻²¹	-1.1543 x 10 ⁻¹⁶	-4.5108 x 10 ⁻²¹
<i>b</i>	-4.9886 x 10 ⁻¹⁴	-8.5075 x 10 ⁻¹⁷	2.8659 x 10 ⁻¹³	4.9649 x 10 ⁻¹⁷
<i>c</i>	1.4956 x 10 ⁻¹⁰	3.7765 x 10 ⁻¹³	-2.8492 x 10 ⁻¹⁰	-2.3268 x 10 ⁻¹³
<i>d</i>	-1.8708 x 10 ⁻⁰⁷	-9.1080 x 10 ⁻¹⁰	1.4537 x 10 ⁻⁰⁷	6.1352 x 10 ⁻¹⁰
<i>e</i>	3.8918 x 10 ⁻⁰⁵	9.9477 x 10 ⁻⁰⁷	-3.8872 x 10 ⁻⁰⁵	-1.0072 x 10 ⁻⁰⁶
<i>f</i>	1.3725 x 10 ⁻⁰¹	2.2532 x 10 ⁻⁰⁴	5.3663 x 10 ⁻⁰³	1.0557 x 10 ⁻⁰³
<i>g</i>	6.2700 x 10 ⁺⁰¹	1.8597 x 10 ⁺⁰⁰	1.4193 x 10 ⁺⁰¹	8.1875 x 10 ⁻⁰¹

Therefore, the $\Delta H_r(T)$ were calculated to be 163.897 kJ mol⁻¹ K⁻¹ at 350°C and 138.280 kJ mol⁻¹ K⁻¹ at 650°C.

D.4. Matlab code

An example of the code used to run the Matlab simulation is shown below for the 650°C ethanol steam reforming:

```
function ydot = EthanolReform650C(z,y)
%variables
t=y(1);
x=y(2);

%fixed parameters
U=46800; % overall heat transfer coefficient in J/s.cm2.K
m=0.00000027; % mol flow rate, mol/s
Cp=1.151; % specific heat of nitrogen @ 650C, J/gK
ta=1; % nondimensional temperature of reactants at the inlet
pc=3.7; % density of silica zirconia, g/cm3
Ti=923.15; % 650C+273.15-> K
H=138279.6; % enthalpy of reaction at 650C, J/mol
ma=46.06844; % molecular weight of ethanol, g/mol
Pao=0.00901398; % partial pressure of ethanol, atm
pi=3.14159265359;
ya=0.00901398; % mole% EtOH

%input parameters
D=0.4; %diameter in cm
L=0.475; % length in cm

%differential equations
dtdz=((pi*D*L*U*(ta-t))/(m*Cp*ma))-((pc*pi*(D^2)*L*((2.21*(10^5))*exp(-10252.586/(Ti*t)))*(Pao*((1-x)/(1+4*ya*x)))^1.2))*H)/(4*Ti*m*Cp*ma));

dxdz((((2.21*(10^5))*exp(-10252.586/(Ti*t)))*(Pao*((1-x)/(1+4*ya*x)))^1.2))*pc*pi*(D^2)*L)/(4*m));

%column vector derivatives
ydot=[dtdz;dxdz];
```

Bibliography

1. Ahmed S, Krumpelt M. Hydrogen from hydrocarbon fuels for fuel cells. *International Journal of Hydrogen Energy*. 2001;26(4):291–301.
2. Small BL, Brookhart M. Iron-Based Catalysts with Exceptionally High Activities and Selectivities for Oligomerization of Ethylene to Linear α -Olefins. *Journal of the American Chemical Society*. 1998;120(28):7143–7144.

3. Utaka T, Takeguchi T, Kikuchi R, Eguchi K. CO removal from reformed fuels over Cu and precious metal catalysts. *Applied Catalysis A: General*. 2003;246(1):117–124.
4. Obradović A, Likožar B, Levec J. Steam methane reforming over Ni-based pellet-type and Pt/Ni/Al₂O₃ structured plate-type catalyst: Intrinsic kinetics study. *Industrial and Engineering Chemistry Research*. 2013;52(38):13597–13606.
5. Tang Y, Roberts CA, Perkins RT, Wachs IE. Revisiting formic acid decomposition on metallic powder catalysts: Exploding the HCOOH decomposition volcano curve. *Surface Science*. 2016;650:103–110.
6. Chansai S, Burch R, Hardacre C, Breen J, Meunier F. Investigating the mechanism of the H₂-assisted selective catalytic reduction (SCR) of NO_x with octane using fast cycling transient in situ DRIFTS-MS analysis. *Journal of Catalysis*. 2010;276(1):49–55.
7. Tang D-TD, Collins KD, Glorius F. Completely Regioselective Direct C–H Functionalization of Benzol[b]thiophenes Using a Simple Heterogeneous Catalyst. *Journal of the American Chemical Society*. 2013;135(20):7450–7453.
8. Somorjai GA. The experimental evidence of the role of surface restructuring during catalytic reactions. *Catalysis Letters*. 1992;12(1–3):17–34.
9. Wunder S, Lu Y, Albrecht M, Ballauff M. Catalytic activity of faceted gold nanoparticles studied by a model reaction: Evidence for substrate-induced surface restructuring. *ACS Catalysis*. 2011;1(8):908–916.
10. Burton JJ, Garten RL. *Advanced Materials in Catalysis*. New York, NY: Academic Press, Inc.; 1977.
11. Zhang H, Wang L, Lu L, Toshima N. Preparation and Catalytic Activity for Aerobic Glucose Oxidation of Crown Jewel Structured Pt/Au Bimetallic Nanoclusters. *Scientific Reports*. 2016;6(April):30752.
12. Yao Y, Goodman DW. New Insights into Structure–Activity Relationships for Propane Hydrogenolysis over Ni–Cu Bimetallic Catalysts. *RSC Advances*.

2015;5:43547–43551.

13. Griffin MB, Rodriguez AA, Montemore MM, Monnier JR, Williams CT, Medlin JW. The selective oxidation of ethylene glycol and 1,2-propanediol on Au, Pd, and Au–Pd bimetallic catalysts. *Journal of Catalysis*. 2013;307:111–120.
14. Xu C, Du Y, Li C, Yang J, Yang G. Insight into effect of acid/base nature of supports on selectivity of glycerol oxidation over supported Au–Pt bimetallic catalysts. *Applied Catalysis B: Environmental*. 2015;164:334–343.
15. Wang C, Li B, Lin H, Yuan Y. Carbon nanotube-supported Pt–Co bimetallic catalysts for preferential oxidation of CO in a H₂-rich stream with CO₂ and H₂O vapor. *Journal of Power Sources*. 2012;202:200–208.
16. Wettstein SG, Bond JQ, Alonso DM, Pham HN, Datye AK, Dumesic JA. RuSn bimetallic catalysts for selective hydrogenation of levulinic acid to γ -valerolactone. *Applied Catalysis B: Environmental*. 2012;117:321–329.
17. Zhang Y, Diao W, Williams CT, Monnier JR. Selective hydrogenation of acetylene in excess ethylene using Ag⁻ and Au–Pd/SiO₂ bimetallic catalysts prepared by electroless deposition. *Applied Catalysis A: General*. 2014;469:419–426.
18. Budroni G, Kondrat SA, Taylor SH, Morgan DJ, Carley AF, Williams PB, Hutchings GJ, Coq B, Figueras F, Ponc V, et al. Selective deposition of palladium onto supported nickel – bimetallic catalysts for the hydrogenation of crotonaldehyde. *Catalysis Science & Technology*. 2013;3(10):2746.
19. Osojnik Črnivec IG, Djinović P, Erjavec B, Pintar A. Effect of synthesis parameters on morphology and activity of bimetallic catalysts in CO₂–CH₄ reforming. *Chemical Engineering Journal*. 2012;207:299–307.
20. Cai W, Piscina PR de la, Homs N. Hydrogen production from the steam reforming of bio-butanol over novel supported Co-based bimetallic catalysts. *Bioresource Technology*. 2012;107:482–486.
21. Navarro RM, Sanchez-Sanchez MC, Fierro JLG. Structure and Activity of Pt–Ni Catalysts Supported on Modified Al₂O₃ for Ethanol Steam Reforming.

- Journal of Nanoscience and Nanotechnology. 2015;15(9):6592–6603.
22. Speight J. Handbook of Petroleum Product Analysis. Hoboken, NJ: John Wiley & Sons; 2002. 454 p.
 23. García L. 4 – Hydrogen production by steam reforming of natural gas and other nonrenewable feedstocks. In: Compendium of Hydrogen Energy. 2015. p. 83–107.
 24. Smith PB, Payne GF. Renewable and Sustainable Polymers. Payne GF, Smith PB, editors. Washington, DC: American Chemical Society; 2011. 1-10 p. (ACS Symposium Series).
 25. Serrano-Ruiz JC, Luque R, Sepúlveda-Escribano A. Transformations of biomass-derived platform molecules: from high added-value chemicals to fuels via aqueous-phase processing. Chemical Society Reviews. 2011;40(11):5266–81.
 26. Simonetti DA, Dumesic JA. Catalytic strategies for changing the energy content and achieving C-C coupling in biomass-derived oxygenated hydrocarbons. ChemSusChem. 2008;1(8–9):725–33.
 27. Trivalent. Building Speed and Agility. 2010 [accessed 2015 Aug 10]. http://www.buildingspeed.org/modules/energyDensity/bs2MOD_energyDensity.php
 28. Date AW. Analytic Combustion: With Thermodynamics, Chemical Kinetics and Mass Transfer. New York, NY: Cambridge University Press; 2011. 366 p.
 29. National Biodiesel Board. Chemical Weight and Formula: Soybean Methyl Ester Formula and Molecular Weight. 2012;3:292.
 30. Choudhary T V., Phillips CB. Renewable fuels via catalytic hydrodeoxygenation. Applied Catalysis A: General. 2011;397(1–2):1–12.
 31. Abhari R, Havlik P. Hydrodeoxygenation process. 2011.
 32. Ardiyanti AR. Hydrotreatment of Fast Pyrolysis Oil. Catalyst Development and

Process-Product Relations. University of Groningen; 2013.

33. Chattanathan SA, Adhikari S, Abdoumoumine N. A review on current status of hydrogen production from bio-oil. *Renewable and Sustainable Energy Reviews*. 2012;16(5):2366–2372.
34. Davda RR, Shabaker JW, Huber GW, Cortright RD, Dumesic J a. A review of catalytic issues and process conditions for renewable hydrogen and alkanes by aqueous-phase reforming of oxygenated hydrocarbons over supported metal catalysts. *Applied Catalysis B: Environmental*. 2005;56(1–2 SPEC. ISS.):171–186.
35. Isikgor FH, C. Remzi Becer. Lignocellulosic Biomass: a sustainable platform for production of bio-based chemicals and polymers. *Polymer Chemistry*. 2015;6:4497–4559.
36. National Research Council. *Future Hydrogen Production and Use : Letter Report*. Washington, DC; 2003.
37. Corma Canos A, Iborra S, Vely A. Chemical routes for the transformation of biomass into chemicals. *Chemical Reviews*. 2007;107(6):2411–2502.
38. Huber GW, Iborra S, Corma A. Synthesis of transportation fuels from biomass: Chemistry, catalysts, and engineering. *Chemical Reviews*. 2006;106(9):4044–4098.
39. Luque R, Herrero-Davila L, Campelo JM, Clark JH, Hidalgo JM, Luna D, Marinas JM, Romero AA. Biofuels: a technological perspective. *Energy & Environmental Science*. 2008;1(5):542–564.
40. Naik SN, Goud V V., Rout PK, Dalai AK. Production of first and second generation biofuels: A comprehensive review. *Renewable and Sustainable Energy Reviews*. 2010;14(2):578–597.
41. Sehested J. Four challenges for nickel steam-reforming catalysts. *Catalysis Today*. 2006;111(1–2):103–110.

42. Münster P, Grabke HJ. Kinetics of the steam reforming of methane with iron, nickel, and iron-nickel alloys as catalysts. *Journal of Catalysis*. 1981;72(2):279–287.
43. Ferencz Z, Erdöhelyi A, Baán K, Oszkó A, ÓVári L, Kónya Z, Papp C, Steinrück HP, Kiss J. Effects of support and Rh additive on co-based catalysts in the ethanol steam reforming reaction. *ACS Catalysis*. 2014;4(4):1205–1218.
44. Vicente J, Ereña J, Montero C, Azkoiti MJ, Bilbao J, Gayubo AG. Reaction pathway for ethanol steam reforming on a Ni/SiO₂ catalyst including coke formation. *International Journal of Hydrogen Energy*. 2014;39(33):18820–18834.
45. Laosiripojana N, Assabumrungrat S. Catalytic steam reforming of methane, methanol, and ethanol over Ni/YSZ: The possible use of these fuels in internal reforming SOFC. *Journal of Power Sources*. 2007;163(2):943–951.
46. Wanke SE, Flynn PC. The Sintering of Supported Metal Catalysts. *Catalysis Reviews*. 1975;12(1):93–135.
47. Shinjoh H, Hatanaka M, Nagai Y, Tanabe T, Takahashi N, Yoshida T, Miyake Y. Suppression of noble metal sintering based on the support anchoring effect and its application in automotive three-way catalysis. *Topics in Catalysis*. 2009;52(13–20):1967–1971.
48. Hou T, Zhang S, Chen Y, Wang D, Cai W. Hydrogen production from ethanol reforming: Catalysts and reaction mechanism. *Renewable and Sustainable Energy Reviews*. 2015;44:132–148.
49. Glasspoole BW, Webb JD, Crudden CM. Catalysis with chemically modified mesoporous silicas: Stability of the mesostructure under Suzuki-Miyaura reaction conditions. *Journal of Catalysis*. 2009;265(2):148–154.
50. Korotcenkov G. The role of morphology and crystallographic structure of metal oxides in response of conductometric-type gas sensors. *Materials Science and Engineering R: Reports*. 2008;61(1–6):1–39.
51. Simson A, Farrauto R, Castaldi M. Steam reforming of ethanol/gasoline

- mixtures: Deactivation, regeneration and stable performance. *Applied Catalysis B: Environmental*. 2011;106(3–4):295–303.
52. Navarro RM, Álvarez-Galván MC, Sánchez-Sánchez MC, Rosa F, Fierro JLG. Production of hydrogen by oxidative reforming of ethanol over Pt catalysts supported on Al₂O₃ modified with Ce and La. *Applied Catalysis B: Environmental*. 2005;55(4):229–241.
53. Kugai J, Subramani V, Song C, Engelhard MH, Chin YH. Effects of nanocrystalline CeO₂ supports on the properties and performance of Ni-Rh bimetallic catalyst for oxidative steam reforming of ethanol. *Journal of Catalysis*. 2006;238(2):430–440.
54. Sánchez-Sánchez MC, Navarro RM, Fierro JLG. Ethanol steam reforming over Ni / M_xO_y-Al₂O₃ (M = Ce, La, Zr and Mg) catalysts: Influence of support on the hydrogen production. *International Journal of Hydrogen Energy*. 2007;32(10–11):1462–1471.
55. Profeti LPR, Ticianelli EA, Assaf EM. Production of hydrogen by ethanol steam reforming on Co/Al₂O₃ catalysts: Effect of addition of small quantities of noble metals. *Journal of Power Sources*. 2008;175(1):482–489.
56. Alayoglu S, Zavalij P, Eichhorn B, Wang Q, Frenkel AI, Chupas P. Structural and Architectural Evaluation of Bimetallic Nanoparticles: A Case Study of Pt-Ru Core-Shell and Alloy Nanoparticles. *ACS nano*. 2009;3(10):3127–3137.
57. Kim KS, Seo HR, Lee SY, Ahn JG, Shin WC, Lee YK. TPR and EXAFS studies on Na-promoted Co/ZnO catalysts for ethanol steam reforming. *Topics in Catalysis*. 2010;53(7–10):615–620.
58. Bayram B, Soykal II, Von Deak D, Miller JT, Ozkan US. Ethanol steam reforming over Co-based catalysts: Investigation of cobalt coordination environment under reaction conditions. *Journal of Catalysis*. 2011;284(1):77–89.
59. Mondal T, Pant KK, Dalai AK. Oxidative and non-oxidative steam reforming of crude bio-ethanol for hydrogen production over Rh promoted Ni/CeO₂-ZrO₂ catalyst. *Applied Catalysis A: General*. 2015;499:19–31.

60. Espinal R, Taboada E, Molins E, Chimentao RJ, Medina F, Llorca J. Ethanol steam reforming over hydrotalcite-derived Co catalysts doped with Pt and Rh. *Topics in Catalysis*. 2013;56(18–20):1660–1671.
61. Lucrédio AF, Assaf JM, Assaf EM. Reforming of a model biogas on Ni and Rh-Ni catalysts: Effect of adding Ia. *Fuel Processing Technology*. 2012;102:124–131.
62. Moraes TS, Neto RCR, Ribeiro MC, Mattos LV, Kourtelesis M, Ladas S, Verykios X, Bellot Noronha F. The study of the performance of PtNi/CeO₂-nanocube catalysts for low temperature steam reforming of ethanol. *Catalysis Today*. 2015;242:35–49.
63. Divins NJ, Llorca J. In situ photoelectron spectroscopy study of ethanol steam reforming over RhPd nanoparticles and RhPd/CeO₂. *Applied Catalysis A: General*. 2015.
64. Agrell J, Birgersson H, Boutonnet M, Melián-Cabrera I, Navarro R., Fierro JL. Production of hydrogen from methanol over Cu/ZnO catalysts promoted by ZrO₂ and Al₂O₃. *Journal of Catalysis*. 2003;219(2):389–403.
65. Okabe K, Saitoh K, Sano T, Yasumoto Y, Shimohura K, Hagiwara H, Takaya H, Bandoh K. Hydrogenation of carbon monoxide to light olefins over chlorine-containing magnetite catalysts in slurry phase. *Journal of The Japan Petroleum Institute*. 1986;29(1):1–7.
66. Wang J, Yasuda H, Inumaru K, Misono M. Catalytic Decomposition of Dinitrogen Oxide over Perovskite-Related Mixed Oxides. *Bulletin of the Chemical Society of Japan*. 1995;68(4):1226–1231.
67. Pande J V., Shukla A, Biniwale RB. Catalytic dehydrogenation of cyclohexane over Ag-M/ACC catalysts for hydrogen supply. *International Journal of Hydrogen Energy*. 2012;37(8):6756–6763.
68. Divins NJ, Angurell I, Escudero C, Pérez-Dieste V, Llorca J. Influence of the support on surface rearrangements of bimetallic nanoparticles in real catalysts. *Science*. 2014;346(6209):620–623.
69. Benito M, Sanz JL, Isabel R, Padilla R, Arjona R, Daza L. Bio-ethanol steam

- reforming: Insights on the mechanism for hydrogen production. *Journal of Power Sources*. 2005;151(1-2):11-17.
70. de Lima SM, Silva AM, Graham UM, Jacobs G, Davis BH, Mattos L V., Noronha FB. Ethanol decomposition and steam reforming of ethanol over CeZrO₂ and Pt/CeZrO₂ catalyst: Reaction mechanism and deactivation. *Applied Catalysis A: General*. 2009;352(1-2):95-113.
71. Trane-Restrup R, Dahl S, Jensen a. D. Steam reforming of ethanol: Effects of support and additives on Ni-based catalysts. *International Journal of Hydrogen Energy*. 2013;38(35):15105-15118.
72. Vesselli E, Baraldi A, Comelli G, Lizzit S, Rosei R. Ethanol decomposition: C-C cleavage selectivity on Rh(111). *ChemPhysChem*. 2004;5(8):1133-40.
73. Resta A, Blomquist J, Gustafson J, Karhu H, Mikkelsen A, Lundgren E, Uvdal P, Andersen JN. Acetate formation during the ethanol oxidation on Rh(111). *Surface Science*. 2006;600:5136-5141.
74. Vesselli E, Comelli G, Rosei R, Freni S, Frusteri F, Cavallaro S. Ethanol auto-thermal reforming on rhodium catalysts and initial steps simulation on single crystals under UHV conditions. *Applied Catalysis A: General*. 2005;281(1-2):139-147.
75. Resta A, Gustafson J, Westerström R, Mikkelsen A, Lundgren E, Andersen JN, Yang MM, Ma XF, Bao XH, Li WX. Step enhanced dehydrogenation of ethanol on Rh. *Surface Science*. 2008;602(18):3057-3063.
76. Chen H-L, Liu S-H, Ho J-J. Theoretical Calculation of the Dehydrogenation of Ethanol on a Rh-CeO₂(111) Surface. *J. Phys. Chem. B*. 2006;110(111):14816-14823.
77. Otto K, Shelef M, Kummer JT. Studies of surface reactions of nitric oxide by nitrogen-15 isotope labeling. I. Reaction between nitric oxide and ammonia over supported platinum at 200-250°. *Journal of Physical Chemistry*. 1970;74(13):2690-2698.
78. Shannon L, Goodwin JG. Characterization of Catalytic Surfaces by Isotopic-

- Transient Kinetics during Steady-State Reaction. *Chemical Rev.* 1995;95:677–695.
79. Lum RM, Klingert JK, Kisker DW, Abys SM, Stevie FA. ^{13}C isotopic labeling studies of growth mechanisms in the metalorganic vapor phase epitaxy of GaAs. *Journal of Crystal Growth.* 1988;93(1–4):120–126.
80. Song H, Bao X, Hadad CM, Ozkan US. Adsorption/desorption behavior of ethanol steam reforming reactants and intermediates over supported cobalt catalysts. *Catalysis Letters.* 2011;141:43–54.
81. Song H, Zhang L, Ozkan US. Investigation of the Reaction Network in Ethanol Steam Reforming over Supported Cobalt Catalysts. *Industrial & Engineering Chemistry Research.* 2010;2(49):8984–8989.
82. López T, Asomoza M, Gomez R. A thermal study of the $\text{SiO}_2\text{-ZrO}_2$ sol-gel system. *Thermochimica Acta.* 1993;223:233–240.
83. Simson A, Waterman E, Farrauto R, Castaldi M. Kinetic and process study for ethanol reforming using a Rh/Pt washcoated monolith catalyst. *Applied Catalysis B: Environmental.* 2009;89(1–2):58–64.
84. Ichikawa M, Fukushima T. Infrared Studies of Metal Additive Effects on CO Chemisorption Modes on SiO_2 -Supported Rh-Mn, -Ti, and -Fe Catalysts. *Journal of Physical Chemistry.* 1985;(89):1564–1567.
85. Trovarelli A, Dolcetti G, Leitenburg C De, Kaspar J, Finetti P, Santonit A. Rh-CeO₂, Interaction induced by High-temperature Reduction. *Journal of the Chemical Society, Faraday Transactions.* 1992;88(9):1311–1319.
86. Suhonen S, Valden M, Hietikko M, Laitinen R, Savimäki A, Härkönen M. Effect of Ce-Zr mixed oxides on the chemical state of Rh in alumina supported automotive exhaust catalysts studied by XPS and XRD. *Applied Catalysis A: General.* 2001;218(1–2):151–160.
87. Yoshida H, Onodera Y, Fujita S, Kawamori H, Arai M. Solvent effects in heterogeneous selective hydrogenation of acetophenone: differences between Rh/C and Rh/Al₂O₃ catalysts and the superiority of water as a functional

- solvent. *Green Chem.* 2015;17(3):1877–1883.
88. Cavanagh RR, Jr. JTY. Site distribution studies of Rh supported on Al₂O₃—An infrared study of chemisorbed CO. *The Journal of Chemical Physics.* 1981;74(7):4150.
89. Min Z, Lin J-Y, Yimsiri P, Asadullah M, Li C-Z. Catalytic reforming of tar during gasification. Part V. Decomposition of NO_x precursors on the char-supported iron catalyst. *Fuel.* 2014;116:19–24.
90. Flytzani-Stephanopoulos M, Wong S, Schmidt LD. Surface Morphology of Platinum Catalysts. *Journal of Catalysis.* 1977;49:51–82.
91. Miller JT, Schreier M, Kropf a. J, Regalbuto JR. A fundamental study of platinum tetraammine impregnation of silica: 2. The effect of method of preparation, loading, and calcination temperature on (reduced) particle size. *Journal of Catalysis.* 2004;225(1):203–212.
92. He Q, Mukerjee S, Shyam B, Ramaker D, Parres-Esclapez S, Illán-Gómez MJ, Bueno-López a. Promoting effect of CeO₂ in the electrocatalytic activity of rhodium for ethanol electro-oxidation. *Journal of Power Sources.* 2009;193(2):408–415.
93. Choi JH, Park KW, Park IS, Nam WH, Sung YE. Methanol electro-oxidation and direct methanol fuel cell using Pt/Rh and Pt/Ru/Rh alloy catalysts. *Electrochimica Acta.* 2004;50(2–3 SPEC. ISS.):787–790.
94. Alayoglu S, Eichhorn B. Rh- Pt Bimetallic Catalysts: Synthesis, Characterization, and Catalysis of Core- Shell, Alloy, and Monometallic Nanoparticles. *Journal of the American Chemical Society.* 2008;130(51):17479–17486.
95. Varga E, Ferencz Z, Oszkó A, Erdőhelyi A, Kiss J. Oxidation states of active catalytic centers in ethanol steam reforming reaction on ceria based Rh promoted Co catalysts: An XPS study. *Journal of Molecular Catalysis A: Chemical.* 2015;397:127–133.
96. Houtman CJ, Barteau MA. Divergent pathways of acetaldehyde and ethanol

- decarbonylation on the Rh(111) surface. *Journal of Catalysis*. 1991;130(2):528–546.
97. Calvin S. *XAFS for Everyone*. Boca Raton, FL: CRC Press; 2013.
98. Attenkofer K, Calvin S, Farquhar E, Frenkel AI, Ehrlich S, Haskel D, Heald S, Karim A, Kas J, Khalid S, et al. *Methods and Applications of X-Ray Absorption Fine Structure Spectroscopy*. In: *XAFS Course*, Brookhaven National Laboratory. Upton, NY; 2014.
99. Newville M. *Fundamentals of XAFS*. Chicago, IL; 2004.
100. Kelly S. *Basics of EXAFS data analysis: X-ray Absorption Fine Structure*. Chicago, IL; 2012.
101. Aleandri LE, Bönnemann H, Jones DJ, Richter J, Rozière J. Structural investigation of bimetallic RH–Pt nanoparticles through X-ray absorption spectroscopy. *J. Mater. Chem.* 1995;5(5):749–752.
102. Ferrando R, Jellinek J, Johnston RL. Nanoalloys: From Theory to Applications of Alloy Clusters and Nanoparticles. *Chemical Reviews*. 2008;108(3):845–910.
103. Crowley S, Li Y, Frenkel AI, Castaldi MJ. In situ x-ray absorbance fine structure (XAFS) of precious metals during ethanol steam reforming. In: *The 249th American Chemical Society National Meeting and Exposition*. Denver, CO; 2015.
104. Singleton DA, Thomas AA. High-precision simultaneous determination of multiple small kinetic isotope effects at natural abundance. *Journal of the American Chemical Society*. 1995;117:9357–9358.
105. Frey FE, Smith DF. Thermal Decomposition of Ethane, Ethylene, Propane, and Propylene. *Industrial & Engineering Chemistry*. 1928;20(9):948–951.
106. Rice FO, Varnerin RE. The mechanism of the thermal decomposition of ethane-d₆. *Journal of the American Chemical Society*. 1954;76(2):324–327.

107. Dar HJ, Nanot SU, Jens KJ, Jakobsen H a., Tangstad E, Chen D. Kinetic Analysis and Upper Bound of Ethylene Yield of Gas Phase Oxidative Dehydrogenation of Ethane to Ethylene. *Industrial & Engineering Chemistry Research*. 2012;51(32):10571–10585.
108. Okamoto Y, Ishida N, Imanaka T, Teranishi S. Active states of rhodium in rhodium exchanged Y zeolite catalysts for hydrogenation of ethylene and acetylene and dimerization of ethylene studied with X-ray photoelectron spectroscopy. *Journal of Catalysis*. 1979;58(1):82–94.
109. Zhao S, Li Y, Stavitski E, Tappero R, Crowley S, Castaldi MJ, Zakharov DN, Nuzzo RG, Frenkel AI, Stach EA. Operando Characterization of Catalysts through use of a Portable Microreactor. *ChemCatChem*. 2015;7:3683–3691.
110. Grunes J, Zhu J, Anderson E a., Somorjai G a. Ethylene hydrogenation over platinum nanoparticle array model catalysts fabricated by electron beam lithography: Determination of active metal surface area. *Journal of Physical Chemistry B*. 2002;106(44):11463–11468.
111. Hutchison DA. Isotopic Exchange of Oxygen in the Systems Water-Silica and Oxygen-Silica. *The Journal of Chemical Physics*. 1954;22(4):758.
112. Spitzer WG, Ligenza JR. Oxygen exchange between silica and high pressure steam. *Journal of Physics and Chemistry of Solids*. 1961;17(3–4):196–202.
113. Busch BW, Schulte WH, Garfunkel E, Gustafsson T, Qi W, Nieh R, Lee J. Oxygen exchange and transport in thin zirconia films on Si(100). *Physical Review B - Condensed Matter and Materials Physics*. 2000;62(20):290–293.
114. Martin D, Duprez D. Mobility of Surface Species on Oxides . 1 . Isotopic Exchange of $^{18}\text{O}_2$ with ^{16}O of SiO_2 , Al_2O_3 , ZrO_2 , MgO , CeO_2 , and $\text{CeO}_2\text{-Al}_2\text{O}_3$. Activation by Noble Metals. Correlation with Oxide Basicity. *Journal of Physical Chemistry*. 1996;2(95):9429–9438.
115. Chelikowsky J, Chadi D, Binggeli N. Oxygen configurations in silica. *Physical Review B*. 2000;62(4):R2251–R2254.
116. Gilat A. *MATLAB: An Introduction With Applications*. 3rd ed. Danvers, MA:

John Wiley & Sons; 2008.

117. Press WH, Teukolsky SA, Vetterling WT, Flannery BP. Numerical Recipes: The Art of Scientific Computing. 3rd ed. New York, NY: Cambridge University Press; 2007.
118. Deng X, Lee J, Wang C, Matranga C, Aksoy F, Liu Z. In Situ Observation of Water Dissociation with Lattice Incorporation at FeO Particle Edges Using Scanning Tunneling Microscopy and X-ray Photoelectron Spectroscopy. *Langmuir*. 2011;27(6):2146–2149.
119. Pereira MFR, Órfão JJM, Figueiredo JL. Oxidative dehydrogenation of ethylbenzene on activated carbon catalysts. I. Influence of surface chemical groups. *Applied Catalysis A: General*. 1999;184(1):153–160.
120. Cadus LE, Gorrioz OF, Rivarola JB. Nature of active coke in the oxydehydrogenation of ethylbenzene to styrene. *Industrial & Engineering Chemistry Research*. 1990;29(7):1143–1146.
121. Agilent Technologies. Agilent 3000 Micro Gas Chromatograph: User Information. 2002.
122. Agilent Technologies. GC Columns and Stationary Phase Applications Guide. 2015 [accessed 2015 Jan 29].
<http://www.chem.agilent.com/cag/cabu/propphase1.htm>
123. Simson AE. Developing an energy efficient steam reforming process to produce hydrogen from sulfur-containing fuels [Dissertation]. Columbia University; 2013.
124. Bagajewicz MJ. Heat Exchanger Design Lecture. [accessed 2016 Jul 13].
[http://www.ou.edu/class/che-design/design 1-2013/Heat Exchangers.pdf](http://www.ou.edu/class/che-design/design%201-2013/Heat%20Exchangers.pdf)
125. The Engineering ToolBox. Convective Heat Transfer. [accessed 2016 Jul 13].
http://www.engineeringtoolbox.com/convective-heat-transfer-d_430.html
126. The Engineering ToolBox. Thermal Conductivity of some common Materials

- and Gases. [accessed 2016 Jul 13].
http://www.engineeringtoolbox.com/thermal-conductivity-d_429.html
127. The Engineering ToolBox. Fouling and Reduced Heat Transfer in Heat Exchangers. [accessed 2016 Jul 13].
http://www.engineeringtoolbox.com/fouling-heat-transfer-d_1661.html
128. Patel J, Malley K. Kirchhoff's Law. [accessed 2016 Jul 1].
http://chemwiki.ucdavis.edu/Core/Physical_Chemistry/Thermodynamics/State_Functions/Enthalpy/Kirchhoff_Law
129. Material Measurement Laboratory. Ethanol. 2016 [accessed 2016 Jul 1].
<http://webbook.nist.gov/cgi/cbook.cgi?ID=64-17-5>
130. The Engineering ToolBox. Water Vapor - Specific Heat. [accessed 2016 Jun 20].
http://www.engineeringtoolbox.com/water-vapor-d_979.html
131. The Engineering ToolBox. Hydrogen - Specific Heat. [accessed 2016 Jun 20].
http://www.engineeringtoolbox.com/hydrogen-d_976.html
132. The Engineering ToolBox. Carbon Dioxide Gas - Specific Heat. [accessed 2016 Jun 20]. http://www.engineeringtoolbox.com/carbon-dioxide-d_974.html